

RICE UNIVERSITY

Missing Energy Studies at the DØ Experiment

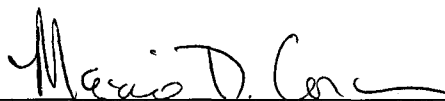
by

Julie Managan Hogan

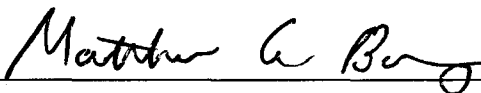
A THESIS SUBMITTED  
IN PARTIAL FULFILLMENT OF THE  
REQUIREMENTS FOR THE DEGREE

Master of Science

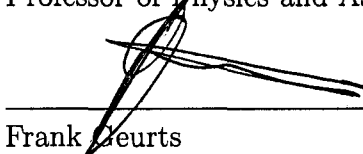
APPROVED, THESIS COMMITTEE:



Marjorie D. Corcoran, Chair  
Professor of Physics and Astronomy



Matthew G. Baring  
Professor of Physics and Astronomy



Frank Geurts  
Assistant Professor of Physics and Astronomy

Houston, Texas

November, 2012

# Missing Energy Studies at the DØ Experiment

Julie Managan Hogan

## Abstract

Missing transverse energy is an important aspect of physics analyses at hadron collider detectors. While other particles can be identified by the energy they deposit in the detector, the presence of neutrinos and other theorized particles must be inferred by an energy imbalance. At the DØ experiment missing energy algorithms exist not only to calculate the missing energy in an event, but to distinguish between possible sources: detector measurement effects or unobserved particles. DØ scientists rely on these algorithms to produce reliable physics results. This thesis presents updates made in the past year to missing energy certification, the unclustered energy resolution, and the missing energy significance calculation. It describes a new processor which calculates missing momentum from tracks as well as development work toward an unclustered energy calibration.

# Acknowledgments

Many thanks to...

Marj Corcoran and my Bonner Lab professors, who prepared me so well for work at DØ.

Leo Bellantoni, who was always ready with a web comic on a stressful day.

My parents, who have encouraged me on this path since the beginning.

And Thomas, who has loved me through long nights of homework, moving to Fermilab,  
and stays strong for me every crazy day of our lives.

# Contents

Abstract	ii
Acknowledgments	iii
List of Illustrations	vi
List of Tables	xi
<b>1 Introduction</b>	<b>1</b>
1.1 Standard Model of Particle Physics . . . . .	1
1.2 Fermilab and the Tevatron . . . . .	5
1.3 The DØ Detector . . . . .	8
1.4 Missing Energy in the DØ Framework . . . . .	15
<b>2 Missing <math>E_T</math> Certification</b>	<b>18</b>
2.1 $\cancel{E}_T$ Certification for RunIIb4 . . . . .	18
2.2 Dependence on Primary Vertex Position . . . . .	22
2.3 $\cancel{E}_T$ Certification for Reprocessed Events . . . . .	31
<b>3 Unclustered Energy Resolution &amp; Missing <math>E_T</math> Significance</b>	<b>41</b>
3.1 Unclustered Energy . . . . .	41

3.2	$\cancel{E}_T$ Significance . . . . .	42
3.3	UE Resolution Functions . . . . .	44
3.4	Effect on $\cancel{E}_T$ Significance . . . . .	54
3.5	Summary & Application . . . . .	60
<b>4</b>	<b>Missing Momentum from Tracks</b>	<b>63</b>
4.1	Missing $p_T$ and $Dphi$ . . . . .	63
4.2	Significance Variables . . . . .	64
4.3	TrackMPT Processor . . . . .	69
4.4	Performance in $Z \rightarrow ee$ events . . . . .	70
4.5	Multi-sample Comparisons . . . . .	73
4.6	$W$ Boson Sample Background Reduction . . . . .	81
4.7	Summary . . . . .	83
<b>5</b>	<b>Unclustered Energy Scale Development</b>	<b>87</b>
5.1	Derivation . . . . .	87
5.2	Calibration based on UE . . . . .	91
5.3	Calibration based on $m_{ue}$ . . . . .	101
5.4	Summary . . . . .	111
<b>6</b>	<b>Conclusions</b>	<b>112</b>
	<b>References</b>	<b>114</b>

# Illustrations

1.1	Particles of the Standard Model. . . . .	2
1.2	Overview of the accelerator system at Fermilab. . . . .	5
1.3	View of the full DØ detector . . . . .	8
1.4	Close up view of the central region of the DØ detector . . . . .	12
2.1	RunIIb4 Certification of METD and SETD showing excesses in the tail regions	20
2.2	RunIIb4 Certification of subdetector $\cancel{E}_T$ . . . . .	21
2.3	RunIIb4 METD and SETD with radial primary vertex position less than 1 cm	22
2.4	RunIIb4 Certification of relationships between METD, SETD, and luminosity	23
2.5	RunIIb4 Certification of relationships between METD, SETD, jets, and primary vertices . . . . .	24
2.6	RunIIb4 Certification of the mean and RMS of METD <sub>x,y</sub> as functions of $\sqrt{SETD}$ . . . . .	25
2.7	METD distributions in RunIIb1 and RunIIb2 show tail excesses in RunIIb1.	26
2.8	Primary vertex position of peak events in each RunIIb epoch. . . . .	28
2.9	Primary vertex position of tail events in each RunIIb epoch. . . . .	29

2.10	Ratio of RunIIB peak events to tail events versus radial primary vertex position. . . . .	30
2.11	Radial primary vertex position for RunIIB peak and tail events. . . . .	30
2.12	METD distributions for each RunIIB epoch after a primary vertex cut at 1 cm. . . . .	31
2.13	RunIIB1 reprocessed $Z \rightarrow ee$ data compared to original data . . . . .	33
2.14	RunIIB2 reprocessed $Z \rightarrow ee$ data compared to original data. . . . .	34
2.15	RunIIB3 reprocessed $Z \rightarrow ee$ data compared to original data. . . . .	35
2.16	RunIIB4 reprocessed $Z \rightarrow ee$ data compared to original data. . . . .	36
2.17	CorrMET in RunIIB1 reprocessed $Z \rightarrow ee$ data/MC and original data/MC . . . . .	37
2.18	CorrSET in RunIIB1 reprocessed $Z \rightarrow ee$ data/MC and original data/MC . . . . .	38
2.19	CorrMET in RunIIB2,3,4 reprocessed $Z \rightarrow ee$ data/MC and original data/MC . . . . .	39
2.20	CorrSET in RunIIB2,3,4 reprocessed $Z \rightarrow ee$ data/MC and original data/MC . . . . .	40
3.1	Demonstration of $UE_x, UE_y$ combination . . . . .	45
3.2	Demonstration of UE resolution function derivation procedure . . . . .	46
3.3	RMS of $UE_{\perp}$ in RunIIB $Z \rightarrow ee$ events in several luminosity bins . . . . .	47
3.4	RunIIa RMS of $UE_{\perp}$ in bins of $\sqrt{SUE}$ with linear fits. . . . .	51
3.5	RunIIB RMS of $UE_{\perp}$ in bins of SUE, with linear fits. . . . .	52
3.6	RMS of $ue_{x,y}$ in RunIIa $Z \rightarrow ee$ data events compared to early UE resolution functions . . . . .	53

3.7	$\cancel{E}_T$ significance distributions with 2006 and 2012 UE resolutions in $Z \rightarrow ee$ data/MC, $W \rightarrow e\nu$ MC, and QCD data . . . . .	56
3.8	Jet separated $\cancel{E}_T$ significance distributions with 2006 and 2012 UE resolutions in RunIIb3 $W \rightarrow e\nu$ MC and QCD data . . . . .	57
3.9	UE Resolution comparison in a $ZH \rightarrow \nu\bar{\nu}b\bar{b}$ multijet and signal selection . .	59
3.10	$\cancel{E}_T$ significance comparison in a $ZH \rightarrow \nu\bar{\nu}b\bar{b}$ multijet and signal selection . .	60
3.11	$\cancel{E}_T$ significance comparison with four lower probability limits . . . . .	61
4.1	Track impact parameter $b$ in the $z$ and $r$ directions . . . . .	70
4.2	Distributions of $\cancel{E}_T$ and $\cancel{p}_T$ in RunIIb3 $Z \rightarrow ee$ events. . . . .	74
4.3	Distributions of $\phi_{\cancel{E}_T}$ and $\phi_{\cancel{p}_T}$ in RunIIb3 $Z \rightarrow ee$ events. . . . .	75
4.4	Distributions of $Dphi$ in RunIIb3 $Z \rightarrow ee$ events . . . . .	76
4.5	Distributions of MPTsig and MMsig in RunIIb3 $Z \rightarrow ee$ events. . . . .	77
4.6	Distributions of $\sigma_{\cancel{p}_T}$ and $\sigma_{Dphi}$ in RunIIb3 $Z \rightarrow ee$ events. . . . .	78
4.7	Reduction of high $\cancel{p}_T$ and $\sigma_{MPT}$ tails by discarding events with MPTsig $< 0.5$	79
4.8	Comparisons of $\cancel{p}_T$ and $Dphi$ distributions in several RunIIb3 samples . . . .	80
4.9	Comparisons of MPTsig and MMsig distributions in several RunIIb3 samples.	81
4.10	Example of a triangle cut . . . . .	82
4.11	Effect of various cuts on $W$ boson transverse mass distribution in RunIIb3 EM Data . . . . .	83



4.12 Comparison of $\cancel{E}_T$ significance and $Dphi$ cuts to a triangle cut on RunIIb3 samples . . . . .	84
4.13 Signal/Background ratios for various $\cancel{E}_T$ significance and $Dphi$ cuts, and a triangle cut with varying slope and intercept . . . . .	85
5.1 Unclustered energy as a function of $Z_T$ in events with zero jets . . . . .	92
5.2 Unclustered energy as a function of $O_T$ in events with any number of jets. . .	93
5.3 Original responses of UE and $mue$ to $O_T$ , with $q = O_T$ . . . . .	93
5.4 MC fit of UE response $r(\sqrt{SET})$ . . . . .	95
5.5 UE response $r(\sqrt{SET})$ : Calibrated $-UE_o$ v. $O_T$ and $r(O_T)$ . . . . .	95
5.6 UE response $r(\sqrt{SET})$ : Original and calibrated UE and $\cancel{E}_T$ distributions . .	96
5.7 Data and MC fits of UE response $r(-UE_o)$ , in events with $O_T < 10$ GeV. . .	97
5.8 UE response $r(-UE_o)$ : Calibrated $-UE_o$ v. $O_T$ and $r(O_T)$ . . . . .	98
5.9 UE response $r(-UE_o)$ : Original and calibrated UE and $\cancel{E}_T$ distributions . .	99
5.10 UE response $r(-UE_o)$ : Original and calibrated SUE and SET distributions .	100
5.11 Data and MC fits of $mue$ response $r(\sqrt{SET})$ . . . . .	102
5.12 $mue$ response $r(\sqrt{SET})$ : Calibrated $mue_o$ v. $O_T$ and $r(O_T)$ . . . . .	102
5.13 $mue$ response $r(\sqrt{SET})$ : Original and calibrated $\cancel{E}_T$ distributions . . . . .	103
5.14 Data and MC fits of $mue$ response $r(mue_o)$ . . . . .	104
5.15 $mue$ response $r(mue_o)$ : Calibrated $mue_o$ v. $O_T$ and $r(O_T)$ . . . . .	105
5.16 $mue$ response $r(mue_o)$ : Original and calibrated $mue$ and UE distributions .	106

5.17	<i>mue</i> response $r(mue_o)$ : Original and calibrated <i>sue</i> and SUE distributions . .	107
5.18	<i>mue</i> response $r(mue_o)$ : Original and calibrated $\mathbb{E}_T$ and SET distributions . .	108
5.19	Calibration of <i>mue</i> response $r(mue_o)$ leaves tails in calibrated $\mathbb{E}_T$ and SET, which are reduced after the tail correction. . . . .	109
5.20	Original and calibrated $\mathbb{E}_T$ and SET distributions showing the effects of tail corrections to the $r(mue_o)$ calibration. . . . .	110

# Tables

2.1	Primary vertex study data samples. . . . .	26
3.1	Data samples used to derive UE resolutions . . . . .	48
3.2	Monte Carlo samples used to derive UE resolutions . . . . .	48
3.3	RunIIa UE Resolution Functions. $\sigma_{UE\perp} = p0 + p1(\sqrt{SUE} - 5)$ . . . . .	50
3.4	RunIIb UE Resolution Functions. $\sigma_{UE\perp} = p0 + p1 * SUE$ . . . . .	50
3.5	October 2006 UE Resolution Functions. $\sigma_{ue_{x,y}} = p0 + p1(\sqrt{sue} - 5)$ . . . . .	53
3.6	January 2007 UE Resolution Functions. $\sigma_{ue_{x,y}} = p0 + p1(\sqrt{sue} - 5)$ . . . . .	54
3.7	$\cancel{E}_T$ significance UE resolution test samples . . . . .	55
3.8	$ZH \rightarrow \nu\bar{\nu}b\bar{b}$ samples. . . . .	58
3.9	METsigAlg processor configuration options . . . . .	62
4.1	TrackMPT processor output variables . . . . .	71
4.2	TrackMPT processor configuration options . . . . .	72
4.3	RunIIb3 $\cancel{p}_T$ test samples . . . . .	80
4.4	Cut Survival Efficiencies for Fig. 4.12 . . . . .	85

5.1	Fit functions for the UE response $r(-UE_o)$ , in events with $O_T < 10$ GeV. . .	98
5.2	Fit functions for $mue$ response $r(\sqrt{SET})$ . . . . .	101
5.3	Fit functions for $mue$ response $r(mue_o)$ . . . . .	105

# Chapter 1

## Introduction

### 1.1 Standard Model of Particle Physics

High energy particle physics is the study of the most fundamental elements of matter in the universe and the forces which govern them. Over the past hundred years the boundaries of what are known as the fundamental particles have shifted drastically – the rapid discovery of new particles in the twentieth century rivaled the previous century’s discoveries of the atomic elements. Today the results of decades of study and experiment are summarized in the Standard Model, which describes the properties of the twelve elementary particles, four “force-carrying” gauge bosons, and the electroweak symmetry breaking Higgs boson (Fig. 1.1).

Three of the forces which define the behavior of the universe and their representative gauge bosons are elements of the Standard Model. All the forces of nature are mediated by the exchange of particles [1]. Heisenberg’s uncertainty principle for virtual particles, written as  $\Delta E \Delta t \leq \hbar$ , allows them to be created and carry energy as long as the transfer happens so quickly that the energy imbalance, according to this principle, is impossible to measure. This relationship defines how long a force-carrying boson can exist, and therefore how far it can travel, before it completes the interaction. The electromagnetic force is

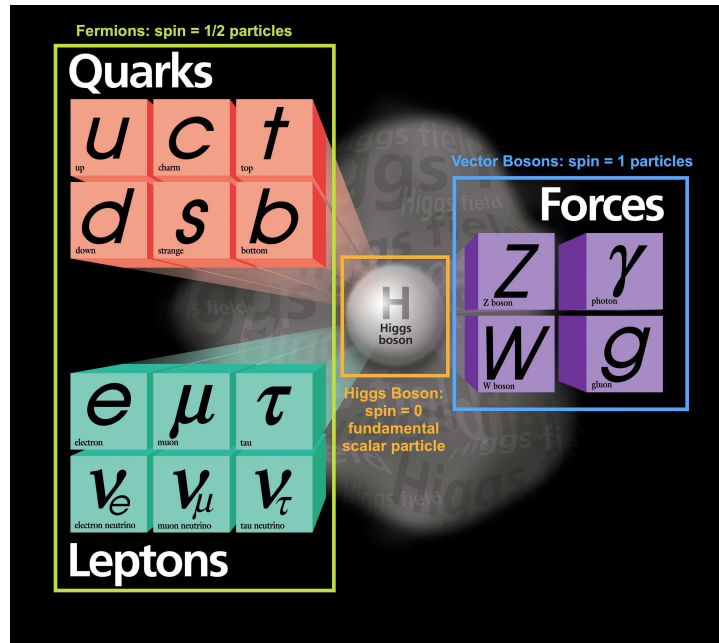


Figure 1.1 : Particles of the Standard Model.

mediated by the massless photon ( $\gamma$ ) which transfers a quantum of electromagnetic energy between electrically charged particles. The strong force is mediated by massless gluons ( $g$ ), which transfer quanta of the whimsically named “color charge” between quarks and other gluons. Because gluons, unlike photons, exhibit this self-interaction, particles which carry color charge are confined within composite particles called hadrons which have a radius of approximately one femtometer, about the size of a small atomic nucleus. The weak force is mediated by the massive  $Z^0$ ,  $W^+$ , and  $W^-$  bosons and has an even shorter range than the strong force. Since the weak gauge bosons have mass their energy for the uncertainty principle can be written as  $E = mc^2$ . So a  $W$  boson traveling near the speed of light can only cover a small fraction of a femtometer before being reabsorbed.

The fermions in the Standard Model are divided into three generations, or families, containing two quarks and two leptons. The masses of the particles increase with each successive generation. The lightest family contains the familiar atomic constituents: up and down quarks which form protons and neutrons, the electron, and the electron neutrino. More massive quarks and leptons were slowly discovered until the third generation was completed with the discovery of the heavy top quark at Fermilab in 1995 [2].

The fermions can also be divided into groups of six quarks and six leptons. Quarks have electric charge of  $+2/3$  (up, charm, and top) or  $-1/3$  (down, strange, and bottom), and interact with the charged weak bosons to turn up-type quarks into down-type quarks or vice-versa. Each quark has a theoretical “color” of red, green, or blue, and interacts with other colored particles by exchanging gluons. Particles containing quarks are called hadrons, which are stable in color-neutral quark combinations: mesons have a quark-antiquark pair of the same color, and baryons have three quarks with one of each color.

Leptons have an electric charge of  $-1$  (electron, muon, and tau) or zero (neutrinos). They interact with the weak force in charged lepton/neutrino pairs, and do not interact with the strong force at all. Neutrinos behave in very unique ways since their mass is nearly zero and their only option for interacting with other particles is through the weak force. While neutrinos are commonly produced in radioactive beta decays or high energy particle collisions, once produced their probability of interacting again is very small. For this reason neutrinos escape the trackers and calorimeters that make up collider detectors without creating ionizing radiation to mark their trail. With patience and sufficiently large

detectors neutrinos can be observed through their interactions with leptons in atoms, but this is not possible at collider detectors.

One of the great successes of the Standard Model as a theory is its ability to unify the electromagnetic and weak forces into a joint symmetry group. This formulation predicts a relationship between the weak boson masses and a mixing angle which has been confirmed by experiments. Another important element of the Standard Model is electroweak symmetry breaking. To create a theory with massive weak bosons and a massless photon, symmetry of the electroweak field must be broken by choosing one of many possible ground states, or “gauges”. The result of this process, called the Higgs mechanism, is an additional massive particle – the Higgs boson. The Standard Model cannot predict the masses of any particles, but after a long search a boson with Higgs-like properties was recently discovered at a mass of 125 GeV by the experiments at CERN’s Large Hadron Collider [3].

There are still many physical concepts which the Standard Model cannot describe. Neutrinos have now been discovered to have mass, which will require a modification to the theory. Gravity is well understood on a macroscopic scale, but cannot be reconciled with the other known forces into a unified theoretical framework. Other cosmological phenomena such as dark matter and dark energy remain even more mysterious. The Standard Model has proved itself an excellent theory, but the door to new discoveries is certainly not closed.



## 1.2 Fermilab and the Tevatron

Fermilab is a United States Dept. of Energy laboratory in Batavia, Illinois, where a wide range of particle physics experiments are conducted. For several decades it boasted the largest and most energetic particle accelerator system in the world. Until recently, the central focus of the physics program at Fermilab was the Tevatron, a hadron collider with two multipurpose detectors. The Tevatron collided 980 GeV protons and antiprotons for a total center of mass energy of 1.96 TeV. The Tevatron was supported by a series of accelerators which worked together to produce and accelerate the particles (Fig. 1.2) [4].

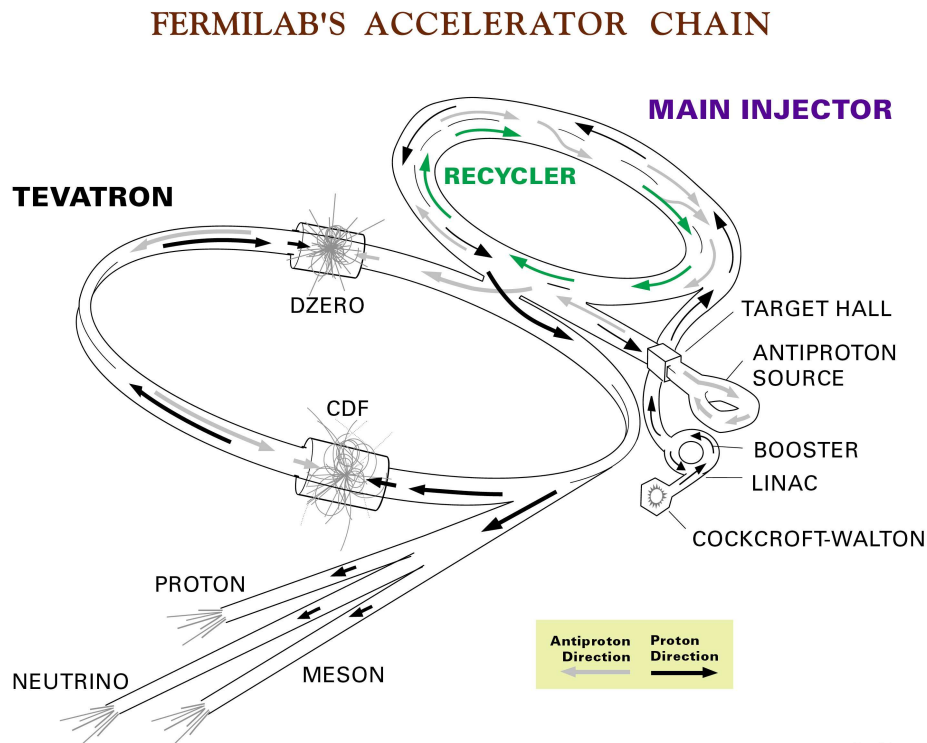


Figure 1.2 : Overview of the accelerator system at Fermilab.

The chain begins with a collection of Cockcroft-Walton accelerators, which feature columns supporting large domes charged to -750 kV where hydrogen atoms pick up electrons to become H<sup>-</sup> ions. The ions are influenced by the electric field and accelerate to an energy of 750 keV as they move down the columns to electrical ground. The ions are then transferred to the Linac, or linear accelerator, which uses a series of 12 “radio frequency” (RF) cavities to increase the ions’ energy to 400 MeV. An RF cavity is literally a gap in the metal beam pipe where an electric field can be applied to the particles within, increasing their kinetic energy. The applied electric field and induced magnetic field of the cavity are in resonance with each other at a frequency designed to be in the radio range of the electromagnetic spectrum, hence the label “RF” cavity. The Linac uses increasingly longer drift tubes between cavities so the particles never cross a cavity when the electric field opposes their direction of motion. The Linac then sends 400 MeV H<sup>-</sup> ions to the Booster, and also sends 66 MeV ions to Fermilab’s Neutron Therapy Facility where neutrons are produced for medical radiation treatments.

In the Booster the H<sup>-</sup> ions are stripped of their electrons and accelerated to an energy of 8 GeV. The Booster is the first circular “synchrotron” accelerator in the chain and has 19 RF cavities. Accelerators like the Booster are called synchrotrons because the RF cavity frequencies must increase in sync with the growing beam energy to protect the particles from opposing electric fields, like the drift tubes in the Linac. This way particles in the beam are continually gaining energy until the RF frequency is set so that they cross the cavities when the electric field is zero. This allows a single ring to both accelerate particles and store them at the desired energy. The Booster transfers the 8 GeV protons to the Main Injector or to

the MiniBooNE target for production of a neutrino beam.

The Main Injector is a much larger circular synchrotron which has 18 RF cavities, accelerating protons to 150 GeV for the Tevatron and 120 GeV for producing antiprotons and secondary beams such as kaons, pions, muons, or neutrinos. Antiprotons are produced when the 120 GeV proton beam strikes a nickel target and magnets are used to isolate 8 GeV antiprotons from the spray of collision products. The antiprotons go through several stages of “cooling” which make the beam more uniform in both space and momentum. Antiprotons undergo stochastic cooling in the Antiproton Source and electron cooling after they move into the Recycler, a storage ring which shares the Main Injector Tunnel. Finally, the antiprotons are returned to the Main Injector for acceleration to 150 GeV and injection into the Tevatron.

The Tevatron is the most well known of Fermilab’s accelerators. It has a 4 mile circumference and the protective berm can be seen from the air. Superconducting niobium-titanium magnets cryogenically cooled to near four degrees Kelvin with liquid helium bend and focus the particle beams, which are accelerated through 8 RF cavities to 980 GeV. The beams are directed so that they collide in two detectors: the Collider Detector at Fermilab (CDF), and  $D\bar{O}$  (named for its position on the Tevatron ring). The accelerator complex was developed over many years and represents an enormous engineering achievement. The Tevatron run ended in September 2011 after the collider detectors recorded approximately  $10 \text{ fb}^{-1}$  of integrated luminosity, or about five trillion collisions [5].

### 1.3 The DØ Detector

The DØ detector is located on the southeast portion of Fermilab's Tevatron accelerator. It is a standard example of modern hadron collider detectors: the beampipe sits inside a tube of silicon trackers which are surrounded by electromagnetic and hadronic calorimeters and a muon tracking system (Fig. 1.3) [6].

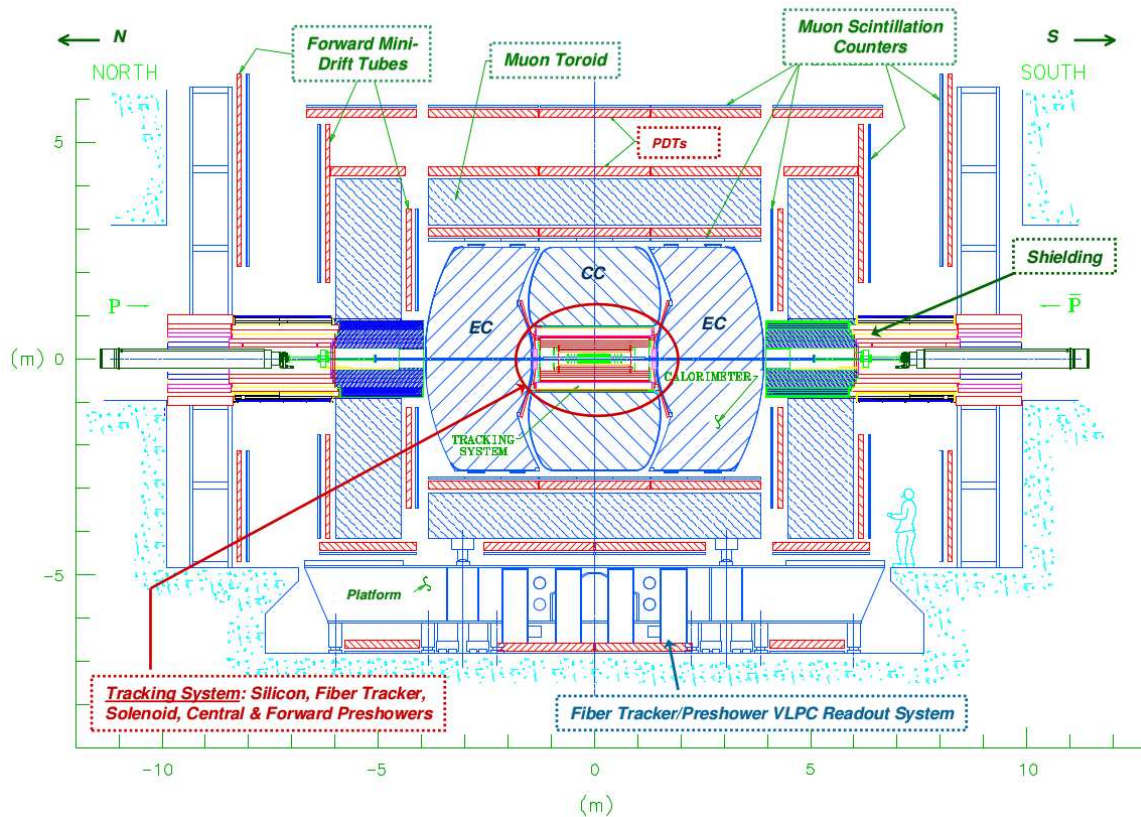


Figure 1.3 : View of the full DØ detector in the  $y-z$  plane showing the beampipe, central tracking, calorimetry, and muon system.

### 1.3.1 Tracking and Preshowers

The tracker, the first layer of detector outside the beryllium beampipe, consists of the silicon microstrip tracker (SMT) and the central fiber tracker (CFT). The SMT, a system of barrels and disks equipped with silicon sensors, is close enough to the interaction point that it can identify secondary vertices in  $b$  quark decays to a precision of approximately  $15\ \mu\text{m}$ . It covers a wide range of polar angle so that tracks can be matched to energy clusters in the calorimeters and muon system. The CFT is made of cylinders of polystyrene scintillating fibers which are located just outside the SMT. The CFT measures tracks with a resolution of about  $100\ \mu\text{m}$ . Charged particles moving through the trackers leave small amounts of ionizing radiation behind, which are detected by sensitive amplifiers in the SMT readout chips and by light produced in the CFT scintillators. Photons produced in the CFT fibers are carried to Visible Light Photon Counters (VLPCs) which convert photons to electrical signals. The VLPCs are operated at 9K and are capable of converting single photons to electrons with an efficiency of greater than 75%. Signals from the tracking detectors are called “hits”, and particle tracks are reconstructed by connecting hits along a path. Both layers of tracking are encased in a 2T solenoid magnet which can be operated at both polarities. Tracking a particle’s motion through the magnetic field gives information about electric charge and momentum, which drastically improved  $D\bar{O}$ ’s RunII performance over the RunI detector which had no magnetic field in its tracker.

Outside the tracking solenoid are the central preshower (CPS) and forward preshower (FPS). In some ways these detectors act as both trackers and calorimeters, and help match

tracks to the calorimeter showers. They are designed to contain approximately two radiation lengths of material which will spark electromagnetic showers from electrons and photons. The CPS is made of triangular scintillator strips which are interlaced so that tracks hit multiple strips and there is no dead space. The FPS has three layers: a minimum ionizing particle (MIP) layer which most particles travel through leaving only a minimum amount of energy, a steel absorber layer, and a shower layer where electrons and photons will leave showers while hadronic particles and muons continue traveling through as MIPs. These different types of behavior in the preshower detectors provide valuable information for particle identification.

### **1.3.2 Calorimeters and Muon System**

The next layer of the  $D\bar{O}$  detector is a series of liquid argon sampling calorimeters. There is no magnetic field in this region so the particles are acted upon by creating short distance electric fields between grounded absorber plates and electronic readout boards with high voltage surfaces. Shower particles created in the absorber plates ionize liquid argon atoms, and the electric field moves the ionization electrons to the readout boards so their energy can be measured. The innermost calorimeter is the electromagnetic calorimeter with 3-4 mm uranium absorber plates which cause electrons and photons to create showers of other electromagnetic particles as they slow down and lose energy. The next layer is the hadronic calorimeter which has two segments: fine and coarse. The fine hadronic calorimeter has thicker absorber plates, 6 mm uranium-niobium alloy, in which hadronic particles begin showers. The coarse hadronic calorimeter's plates are much thicker, 46 mm, and made of

copper or stainless steel. While traveling through the calorimeter all hadronic particles will shower into cone-shaped clusters of energy. Collections of closely spaced showers form “jets” which are used to trace hadronic particles back to the original quarks from a collision and estimate their energies.

The calorimeters exist in three sections, a central barrel and two endcaps, so to maintain the 90K liquid argon temperature three separate cryostats are needed. Just inside each cryostat, outside the first layer of uranium, are subdetectors called the massless gaps (MG), which are essentially one calorimeter readout cell. In between the cryostats are the intercryostat detectors (ICD) which are made of scintillating tiles in light-tight aluminum boxes. The light from particles impacting the scintillator is directed through wavelength shifting fibers to photomultiplier tubes. Also between the calorimeter cryostats are the luminosity monitors. The luminosity monitors are two arrays of twenty-four scintillating crystals and photomultiplier tubes which are mounted around the beampipe next to the endcap calorimeters. They measure  $p\bar{p}$  inelastic scattering to calculate the number of collisions in the detector as well as to monitor beam halo backgrounds.

The muon tracking system is the exterior layer of the  $D\bar{O}$  detector and tracks the momentum of muons, the only charged particles which travel through all the tracking and calorimeter layers without interacting. The muon system uses a 1.8T toroidal magnetic field, drift tubes, and scintillation counters to make an independent momentum measurement which helps match muons to tracks left in the central detector and improve the muon momentum resolution.

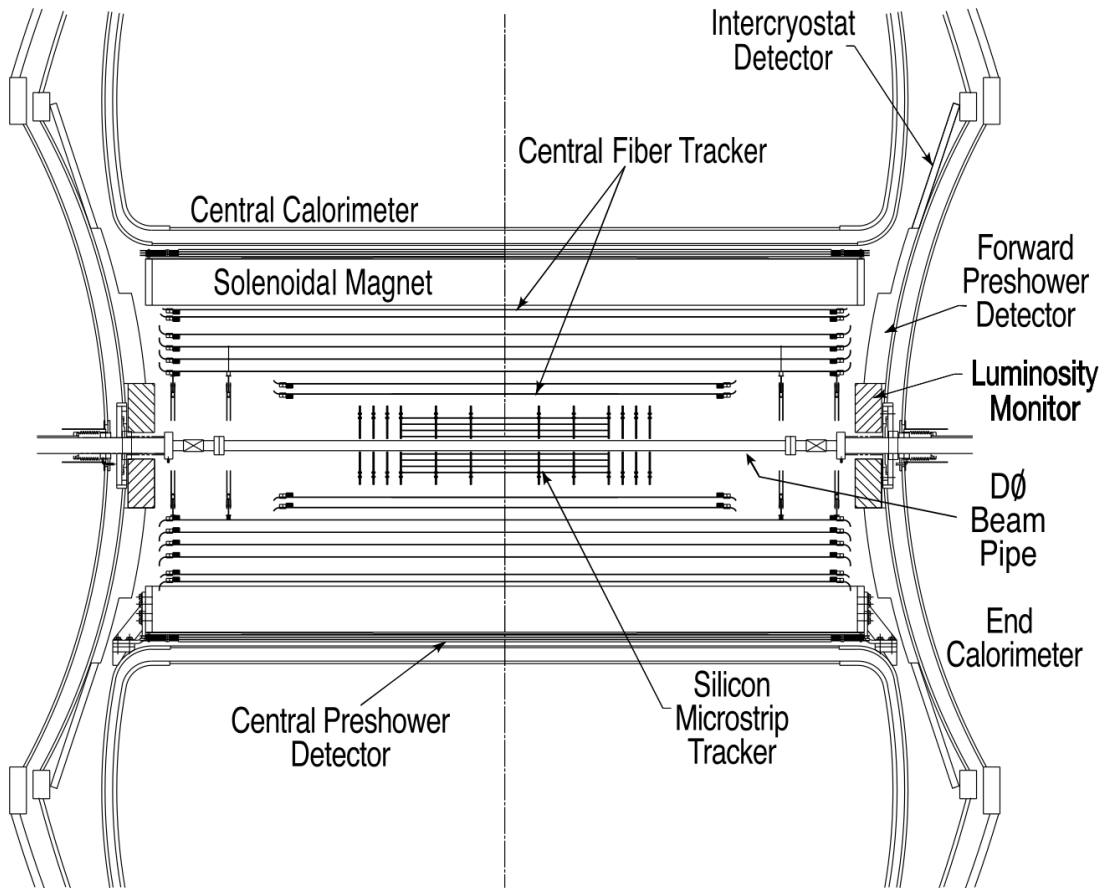


Figure 1.4 : Close up view of the central region of the DØ detector showing the SMT, CFT, solenoid, preshower detectors, luminosity monitors, and intercryostat detectors.



### 1.3.3 Triggers and Data Reconstruction

Collisions are processed through three levels of triggers to collect events with interesting physics processes. The first level is a series of hardware triggers which make decisions to keep or reject events based on calorimeter energy deposits or track momenta above certain thresholds. These triggers accept an average of 2000 events per second, or a rate of 2 kHz. The second trigger level combines hardware triggers with computer processors which can form physics objects, match tracks to calorimeter clusters, and calculate quantities such as missing transverse energy and a track's impact parameter with the beam. This information is used to look for known signatures across the subdetectors and reduce the accepted event rate by half. The Level 3 trigger is a farm of microprocessors which make more detailed calculations and study relationships between objects in the event to reduce the accept rate to 50-100 Hz. This final output rate is manageable for the tape record system and promotes high quality physics data samples.

Events passing all three trigger levels are processed through DØ's reconstruction code and "skimmed" to produce smaller data samples containing events with similar objects or conditions. Reconstructed data samples are stored and accessed with a program called SAM: Sequential data Access via Metadata. Each data sample has a unique SAM "definition" which allows the program to access specific files and make them available to a user's analysis program. SAM definitions are used here to identify the samples for each study in a way that other DØ users could replicate. DØ's Common Samples Group creates SAM definitions with consistent terms. The definition "CSG\_CAF\_2EMhighpt\_PASS5\_p21.18.00\_p20.16.08"

provides the following information:

- CSG: definition produced by the Common Samples Group.
- CAF: data processed using DØ’s Central Analysis Framework.
- 2EMhighpt: name of the specific data skim.
- PASS5: indicates a major version of the reconstruction code; also the data epoch.
- p21.18.00: CAF version number.
- p20.16.08: specific version of the reconstruction code.

### 1.3.4 Monte Carlo Simulation

DØ data is simulated using Monte Carlo methods. The Monte Carlo events are produced using the GEANT3 program [7] to model the detector materials and ALPGEN [8] and/or PYTHIA [9] to model the physics processes. Monte Carlo (MC) has been produced to simulate a large number of physics processes for each data epoch. MC for the studies presented here uses ALPGEN for particle generation combined with PYTHIA for hadronization processes, and the CTEQ6L1 parton distribution function library [10].

DØ MC is also identified and accessed using SAM. Common SAM definitions for MC have different identifiers than data definitions. For example, a SAM definition for  $Z \rightarrow ee$  events “CSG\_alpgenpythia\_gamz\_ee\_75\_130\_p212100\_Run2b3\_v3” gives the following information:

- CSG: definition produced by the Common Samples Group.

- `alpgenpythia`: ALPGEN+PYTHIA used to model physics processes.
- `gamz`: main particles ( $\gamma$  or  $Z$ ) produced in the collision.
- `ee`: decay products (two electrons) of the main particles.
- `75_130`: mass range of the main particles.
- `p212100`: CAF version number.
- `Run2b3_v3`: data epoch and version of the simulation.

## 1.4 Missing Energy in the DØ Framework

Because neutrinos cannot be directly detected in collider experiments we rely on missing transverse energy to identify their presence. Since the colliding beams move in opposite directions with equal energy, conservation of momentum requires that the vector sum of particle momenta orthogonal to the beam direction be equal to zero. When this sum is nonzero noise in the detector, random fluctuations of measured particle energies, or undetected particles like neutrinos participated in the event. Many models of physics beyond the Standard Model also include particles, such as the supersymmetric *neutralino*, whose only signature is a substantial excess of missing energy.

DØ calculates missing transverse energy ( $E_T$  or MET) as the negative vector sum of all energy deposits in a collection of calorimeter cells. Energy is a scalar quantity, but the magnitude and location of calorimeter energy deposits can be used to closely estimate a particle's momentum. A spatial coordinate system is defined for the DØ detector such that

$\hat{x}$  points out of the Tevatron ring,  $\hat{y}$  points up, and  $\hat{z}$  points along the direction of the proton beam. In this coordinate system the  $x$  and  $y$  components of  $\mathbf{E}_T$  for a group of cells are calculated as:

$$\cancel{E}_{T,x} = - \sum_{\text{cells}} E_x^{\text{cell}} \quad (1.1)$$

$$\cancel{E}_{T,y} = - \sum_{\text{cells}} E_y^{\text{cell}} \quad (1.2)$$

The magnitude and direction of  $\mathbf{E}_T$  are then:

$$E_T = \sqrt{(\cancel{E}_{T,x})^2 + (\cancel{E}_{T,y})^2} \quad (1.3)$$

$$\phi_{\cancel{E}_T} = \tan^{-1} (\cancel{E}_{T,y} / \cancel{E}_{T,x}) \quad (1.4)$$

The scalar sum of calorimeter cell energy deposits is called scalar transverse energy (SET):

$$SET = \sum_{\text{cells}} E_T^{\text{cell}} \quad (1.5)$$

$\mathbf{E}_T$  and SET are calculated for each calorimeter component and sums of these components form the various definitions of  $\mathbf{E}_T$ . The two most basic definitions are called ‘‘METC’’ and ‘‘METD’’:

$$\mathbf{METC} = \mathbf{METEM} + \mathbf{METMG} + \mathbf{METICD} + \mathbf{METFH} + \mathbf{METCH} \quad (1.6)$$

$$\mathbf{METD} = \mathbf{METEM} + \mathbf{METMG} + \mathbf{METICD} + \mathbf{METFH} \quad (1.7)$$

$$SETC = SETEM + SETMG + SETICD + SETFH + SETCH \quad (1.8)$$

$$SETD = SETEM + SETMG + SETICD + SETFH \quad (1.9)$$

where  $\mathbf{METEM}$  is the  $\mathbf{E}_T$  from the electromagnetic calorimeter,  $\mathbf{METMG}$  is the  $\mathbf{E}_T$  from the massless gaps,  $\mathbf{METICD}$  is the  $\mathbf{E}_T$  from the intercryostat detectors,  $\mathbf{METFH}$  is the  $\mathbf{E}_T$

from the fine hadronic calorimeter, **METCH** is the  $\cancel{E}_T$  from the coarse hadronic calorimeter, and SET follows the same conventions. In general the coarse hadronic calorimeter suffers too much from noise to be useful in  $\cancel{E}_T$  calculations so it is discarded from METD, the standard form of uncorrected  $\cancel{E}_T$ .

Since the energies of physics objects are corrected for detector effects after reconstruction  $\cancel{E}_T$  also requires correction. The processor `ReComputeMET` in the DØ analysis framework adjusts METD and SETD as necessary to correct for jet energy in the coarse hadronic calorimeter (**CHcorr**), scaling of jet energy (**JEScorr**), scaling of electromagnetic object energy (**EMcorr**), muon momentum measured in the muon system (**MUcorr**), and energy left by muons in the calorimeter (**MUCalcorr**). For each term the corrections to METD<sub>x</sub>, METD<sub>y</sub>, and SETD are calculated and added to the uncorrected value.

$$\begin{aligned} \mathbf{CorrMET} = \mathbf{METD} + \mathbf{CHcorr} + \mathbf{JEScorr} \\ + \mathbf{EMcorr} + \mathbf{MUcorr} + \mathbf{MUCalcorr} \end{aligned} \quad (1.10)$$

$$\mathit{CorrSET} = \mathit{SETD} + \mathit{CHcorr} + \mathit{JEScorr} + \mathit{EMcorr} + \mathit{MUcorr} + \mathit{MUCalcorr} \quad (1.11)$$

These corrected versions of  $\cancel{E}_T$  and SET serve as the basic variables for analysts.

Since  $\cancel{E}_T$  is a crucial component of events with neutrinos in the final state there are multiple algorithms dedicated to both measuring the missing energy and identifying collisions with real missing energy from physics processes. Chapters 2-5 detail the work that has been done to certify the missing energy measurements at DØ, develop new missing energy tools, and improve the existing tools.

## Chapter 2

### Missing $E_T$ Certification

#### 2.1 $E_T$ Certification for RunIIb4

Data collected at DØ during RunII is split into several sections, or epochs. RunIIa encompasses the time up to March 2006. A major upgrade was performed on the detector and data taken after the upgrade, from June 2006 through September 2011, is called RunIIb. RunIIb is further separated into four epochs: RunIIb1 - RunIIb4. After the data for each epoch was completed and cataloged,  $E_T$  and other reconstructed objects required certification to ensure that the identification algorithms performed properly in the analysis framework.

Unlike physics objects such as electrons, which have a certain probability of being correctly identified in an event,  $E_T$  is always measured. To certify  $E_T$ , distributions from one epoch are compared to that of another and the differences interpreted. Certification is performed on the events in the “zero-bias/minimum-bias” (ZBMB) data sample. Zero-bias and minimum-bias events form a random sample of activity in the detector. Zero-bias events only require that a beam crossing occurred, while minimum-bias events add the requirement that inelastic collisions be observed in the luminosity monitor. Figure 2.1 shows the METD distributions for the RunIIb4 certification. Similar distributions are plotted for all the  $E_T$  definitions used in Eq. 1.6 (Fig. 2.2) so that each subdetector can be checked for discrep-

ancies. The RunIIb4 certification revealed large tails in the  $\cancel{E}_T$  distributions, which were eventually linked to events with poorly reconstructed primary vertices. Figure 2.3 shows RunIIb4  $\cancel{E}_T$  compared to RunIIb3 after a cut at 1.0 cm is placed on the radial position of the primary vertex. The study leading to this choice of vertex cut is described in the next section.

$\cancel{E}_T$  certification also includes a study of the relationships between  $\cancel{E}_T$ , scalar  $E_T$  (SET), number of jets, number of primary vertices, and luminosity. Luminosity and SET are both general measures of the amount of activity in an event, so it is expected that the average amount of  $\cancel{E}_T$  will increase steadily with both of these variables (Fig. 2.4). A primary vertex is the location of an interaction between a proton and antiproton in the beams, as opposed to vertices formed by the decay of collision products. Aside from major changes in jet or primary vertex algorithms, the relationships between these variables,  $\cancel{E}_T$ , and SET should remain constant (Fig. 2.5). Significant changes in these relationships can help identify issues with the reconstruction. This part of the RunIIb4 certification revealed a marked decrease in the number of primary vertices along with an increase in the average  $\cancel{E}_T$  per vertex. Both discrepancies arose from changes in the vertexing algorithms for RunIIb4.

The final component of  $\cancel{E}_T$  certification involves studying the relationship between  $\sqrt{SET}$  and the mean and RMS of MET<sub>x</sub> and MET<sub>y</sub> (Fig. 2.6). Since the average value of  $\cancel{E}_T$  has been shown to increase linearly with  $\sqrt{SET}$  it is expected that the width of the  $x$  and  $y$  components will exhibit the same relationship. While the widths of MET<sub>x</sub> and MET<sub>y</sub> are expected to grow with increasing event activity, the mean values of these distributions should

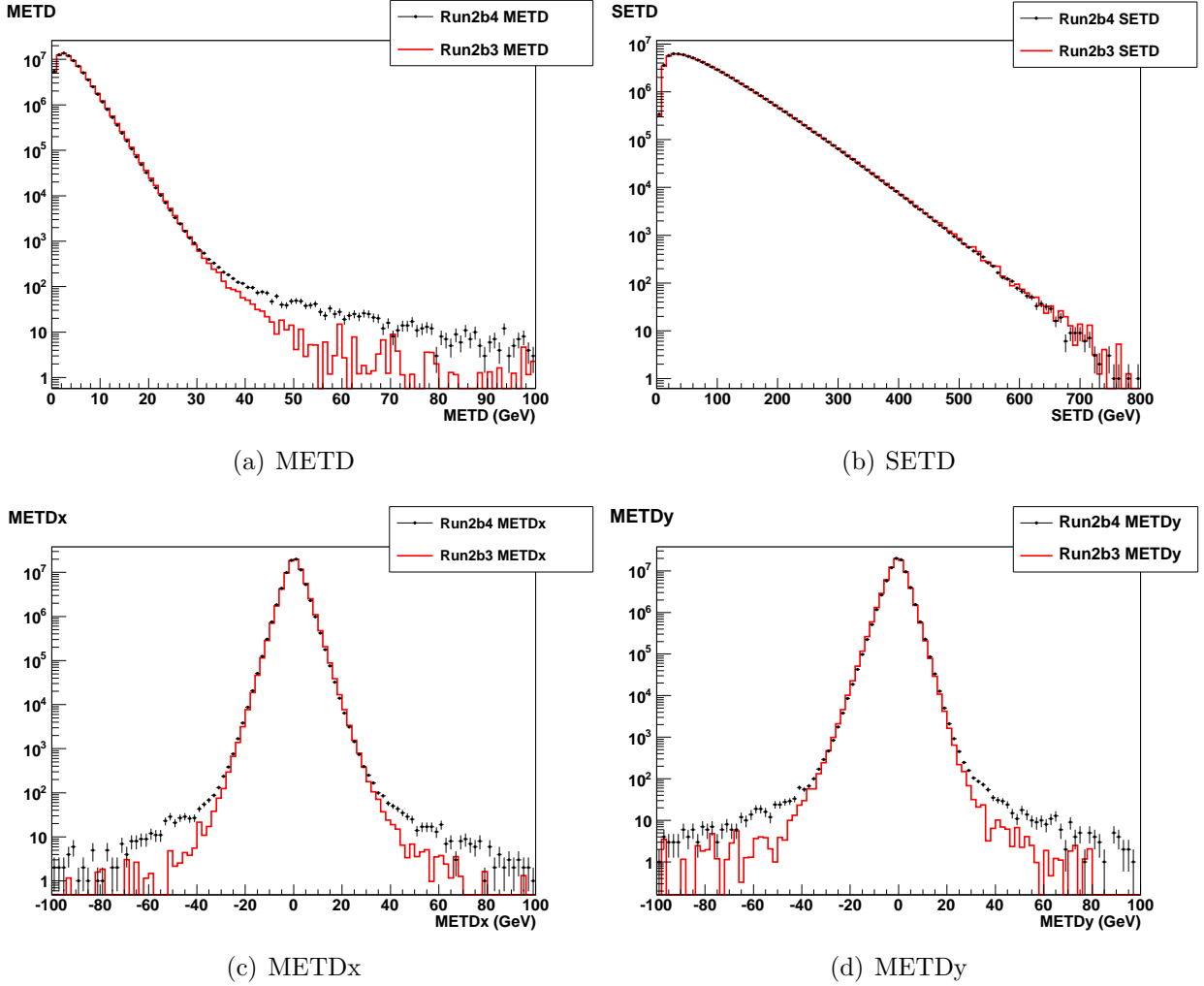


Figure 2.1 : Certification of METD and SETD in RunIIB4 ZBMB events showing excesses in the tail regions. METD (a) is the  $\cancel{E}_T$  from the electromagnetic and fine hadronic calorimeters as well as the massless gaps and intercryostat detectors. SETD (b) is the scalar sum of energy deposited in each of these subdetectors. METDx (c) and METDy (d) are the spatial components of METD. For example,  $\text{METD}_x = -\sum_{\text{EM calo}} E_x - \sum_{\text{FH calo}} E_x - \sum_{\text{MG}} E_x - \sum_{\text{ICD}} E_x$ .



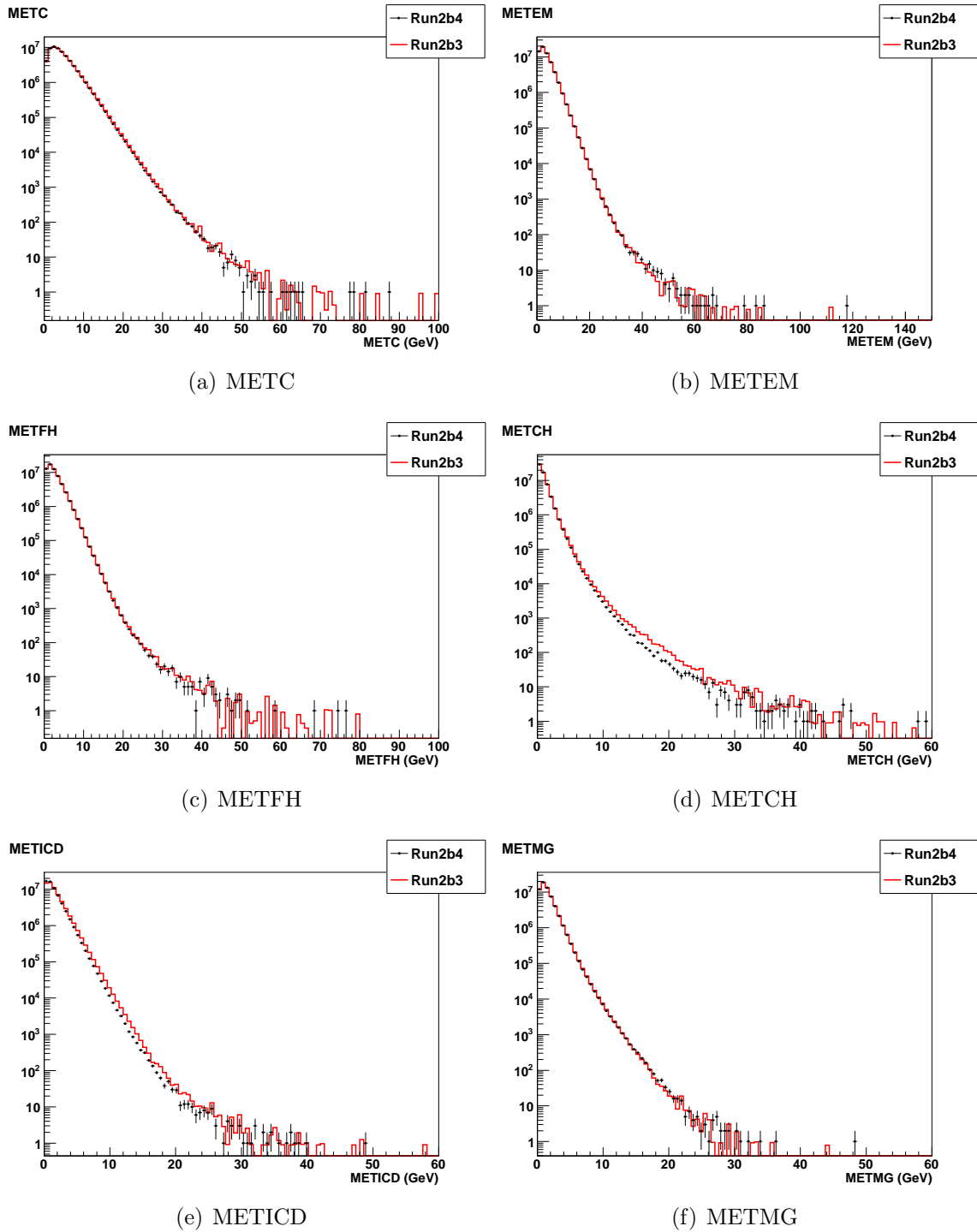


Figure 2.2 : Certification of subdetector  $\cancel{E}_T$  in RunIIb4 ZBMB events with radial primary vertex position less than 1 cm. This primary vertex cut reduces the high  $\cancel{E}_T$  tails seen in Fig. 2.1.

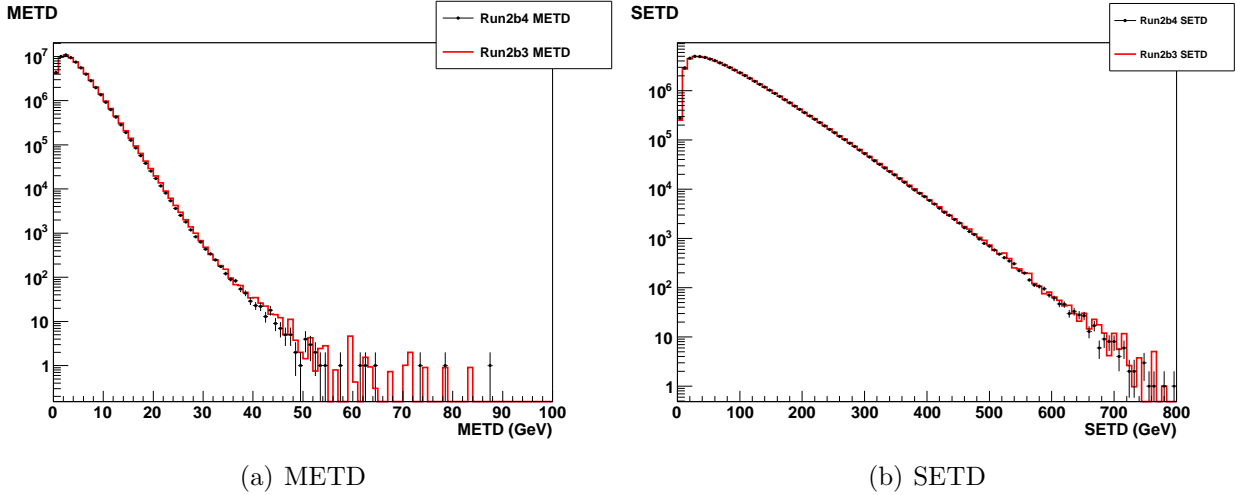


Figure 2.3 : RunIIB4 METD and SETD with radial primary vertex position less than 1 cm, a cut which removes the high  $\cancel{E}_T$  tails seen in Fig. 2.1.

remain close to zero. It has been consistently observed that MET<sub>x</sub> shifts slowly to positive values as  $\sqrt{SET}$  increases and MET<sub>y</sub> shifts slowly to negative values. In RunIIB4 the mean values of both distributions remained closer to zero than in RunIIB3.

## 2.2 Dependence on Primary Vertex Position

While  $\cancel{E}_T$  certification shows that scalar  $E_T$  distributions remained fairly constant over the course of RunIIB, distributions of  $\cancel{E}_T$  exhibit tails which vary with data epoch (Fig. 2.7). To some extent, these tails are the result of primary vertex locations that are unphysical. METD distributions were studied in each data epoch using the data samples listed in Tab. 2.1. Primary vertex positions were compared for events in two categories: “peak” events with METD less than 15 GeV, and “tail” events with METD greater than 40 GeV.

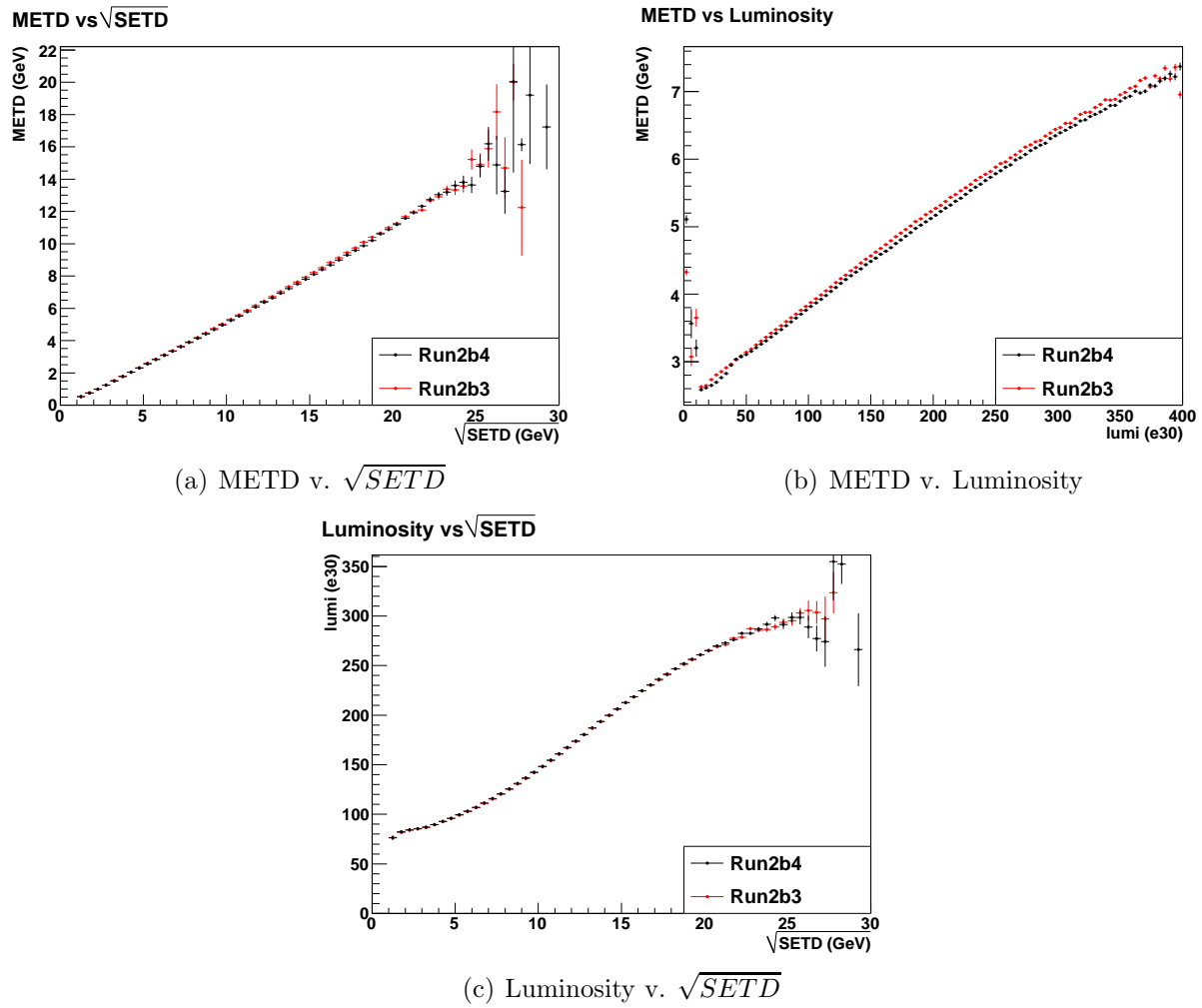


Figure 2.4 : Certification of relationships between METD, SETD, and luminosity in RunIIb4 ZBMB events. METD has the expected monotonic increase with respect to SETD and luminosity (a-b), and no large changes are shown between run periods.

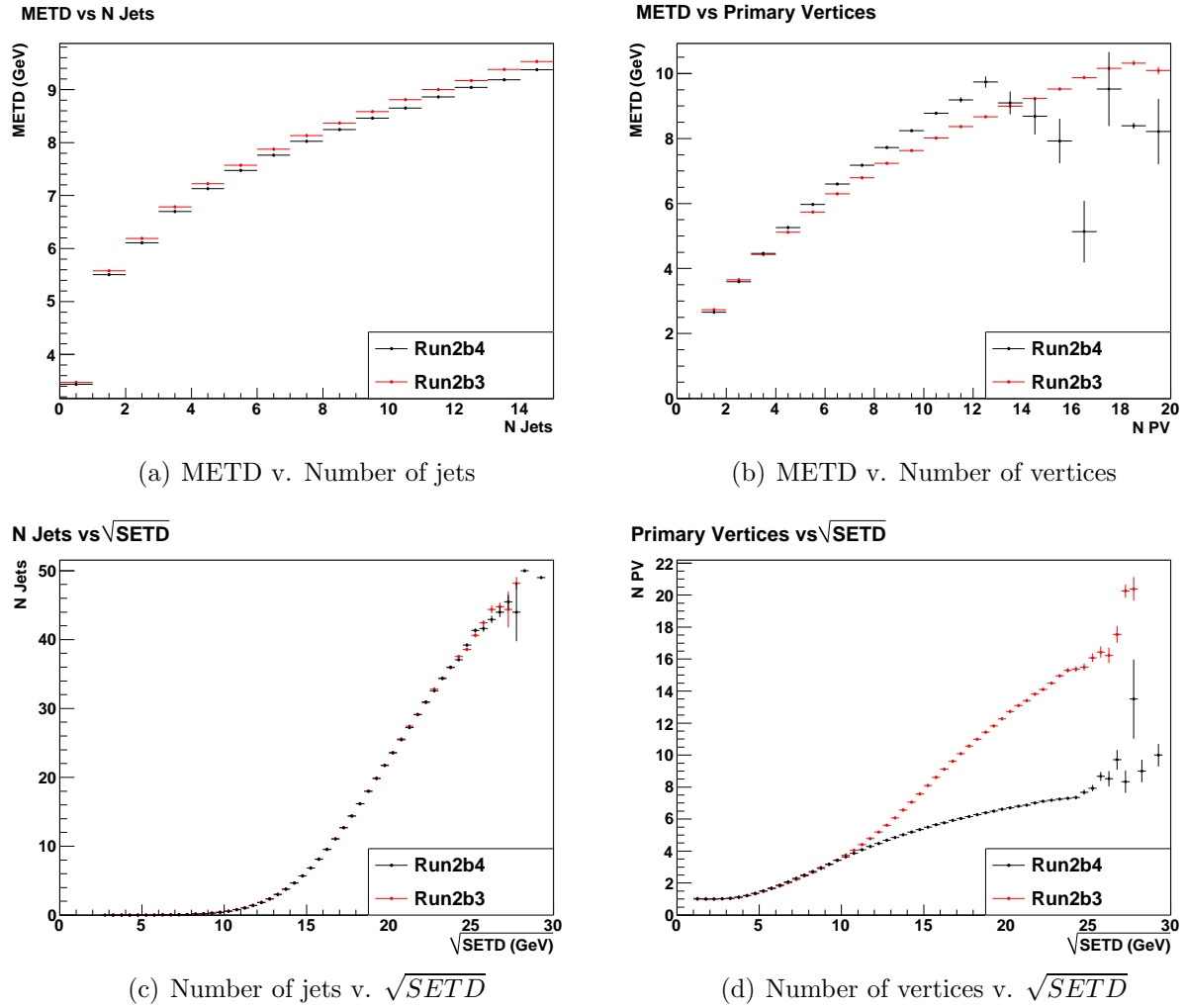


Figure 2.5 : Certification of relationships between METD or SETD and jets and primary vertices in RunIIb4 ZBMB events. Changes in the primary vertex algorithms caused a reduced average number of vertices in higher activity events in RunIIb4 (d).

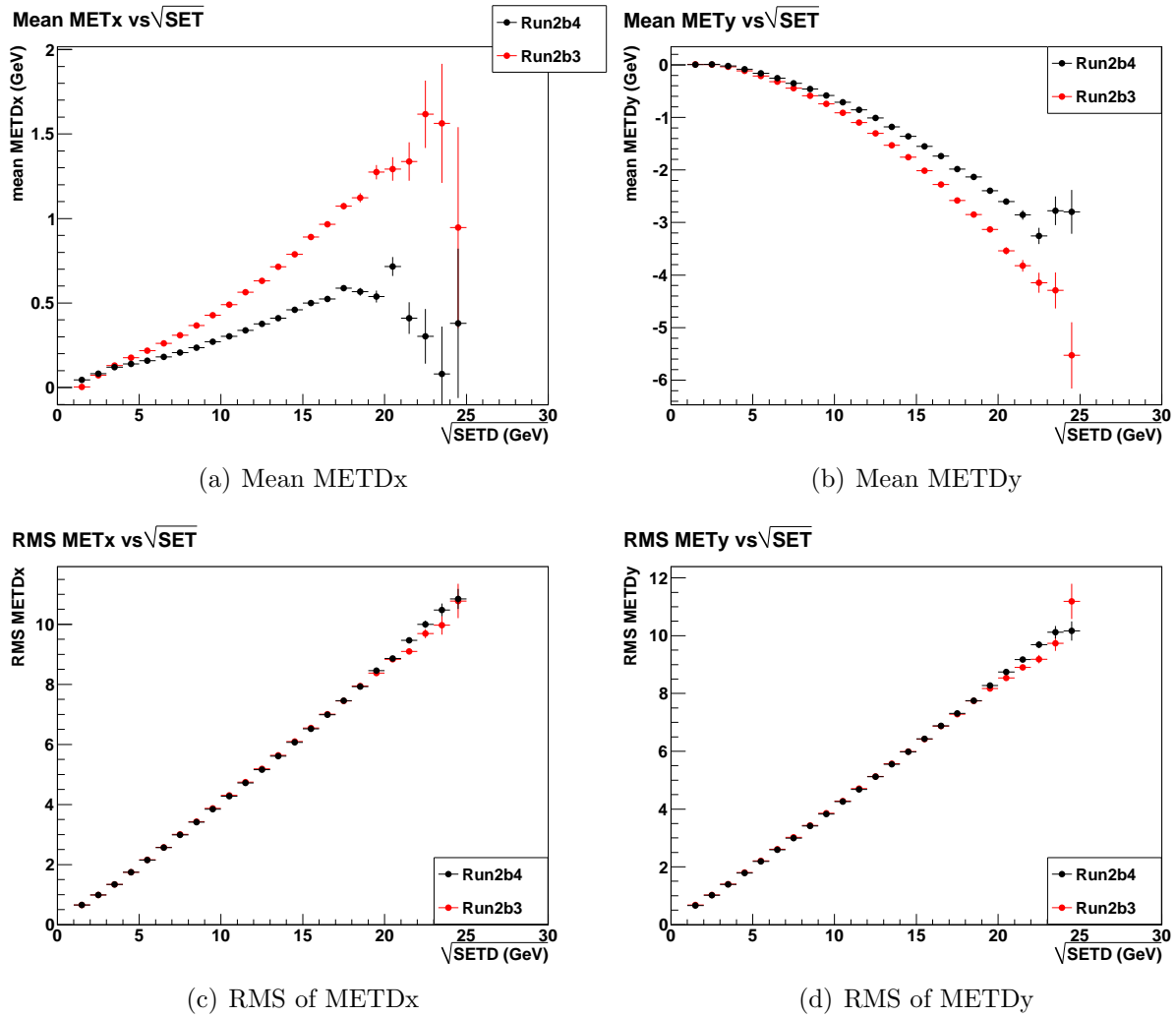


Figure 2.6 : Certification of the mean (a-b) and RMS (c-d) of METD<sub>x,y</sub> as functions of  $\sqrt{SETD}$  in RunIIb4 ZBMB events.

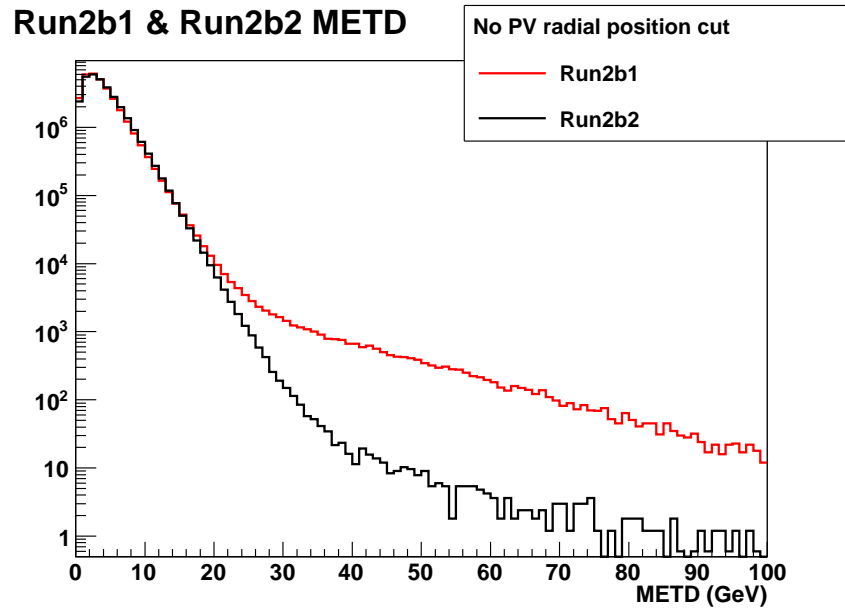


Figure 2.7 : METD distributions in RunIIb1 and RunIIb2 show tail excesses in RunIIb1.

Data Epoch	SAM Definition	N events
RunIIb1	CSG_CAF_ZBMB_PASS2_p21.10.00	39585760
RunIIb2	CSG_CAF_ZBMB_PASS4_p21.1x.00	60805480
RunIIb3	CSG_CAF_ZBMB_PASS5_p21.18.00	68885411
RunIIb4	CSG_CAF_ZBMB_PASS6_p21.20.00	45617957
	CSG_CAF_ZBMB_PASS6_p21.21.00	

Table 2.1 : Primary vertex study data samples.

Peak events, regardless of data epoch, tend to have highly central primary vertex positions, with a small fraction of events uniformly scattered outward (Fig. 2.8). Tail events, however, do not show a uniform scatter (Fig. 2.9). The primary vertex is either central, corresponding to well-vertexed events with real  $\cancel{E}_T$ , or greater than approximately 2 cm away.

This effect is especially noticeable for RunIIb1 and RunIIb4 data, which have significantly more tail events than RunIIb2 and RunIIb3 because of changes in requirements for identifying a primary vertex. During RunIIb1 only two tracks were required for a vertex to be labeled a primary vertex. For RunIIb2 and RunIIb3 the requirement was changed to three tracks, although four or more tracks were preferred. In RunIIb4 a fake track killer was implemented, so the requirement was loosened to two tracks.

While the ratio of peak to tail events falls relatively smoothly (Fig. 2.10), a plot of radial primary vertex position for peak and tail events in all RunIIb epochs shows a bimodal distribution for the tail events, with a clear minimum near 1.0-1.5 cm (Fig. 2.11). The minimum region is in good agreement with the 1.42 cm inner radius of the beampipe [11], and cuts at 1 cm greatly improve the agreement in METD distributions across data epochs (Fig. 2.12). This is an appropriate cut for many analyses studying events with two-particle vertices, especially those which also rely heavily on  $\cancel{E}_T$ .

RunIIb4 was reconstructed in five segments, and the final two segments place a radial cut of 1.6 cm on the primary vertex position, consistent with the results of this study. No manual vertex cut was needed to reduce  $\cancel{E}_T$  tails in these segments. Combined with vertex

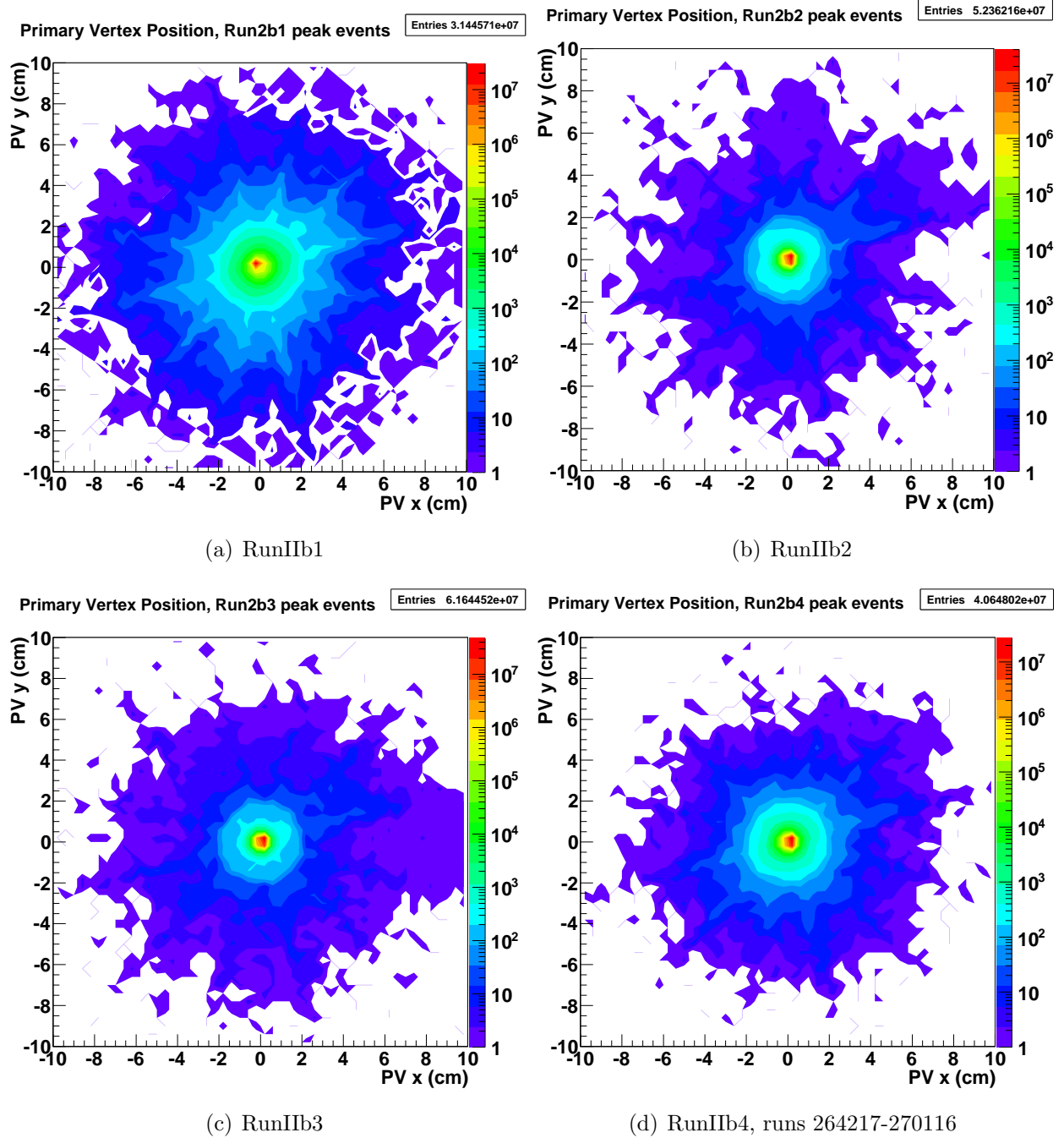


Figure 2.8 : Primary vertex position of peak events in each RunIIb epoch.



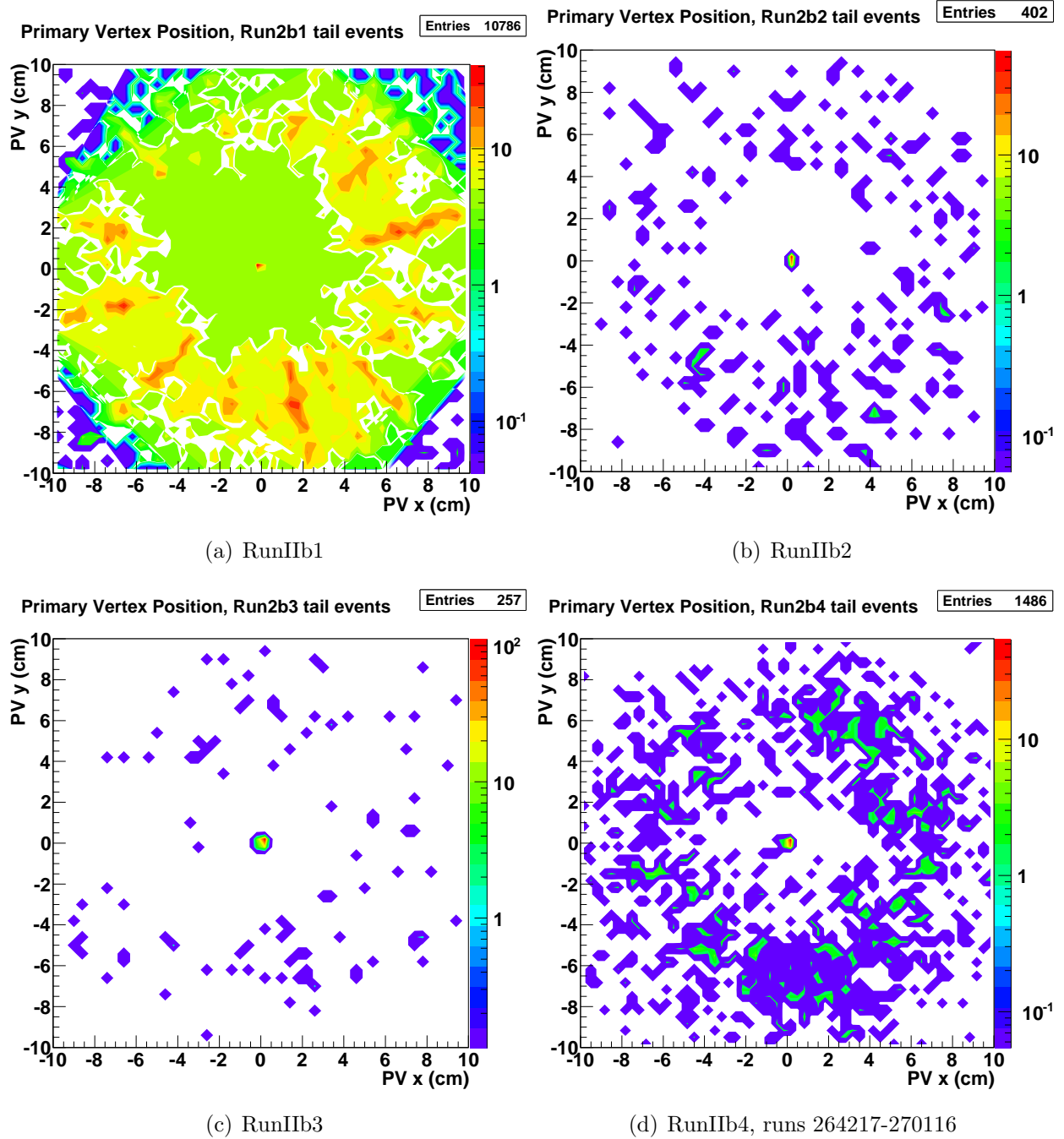


Figure 2.9 : Primary vertex position of tail events in each RunIIb epoch.

### Run2b Peak/Tail Ratio

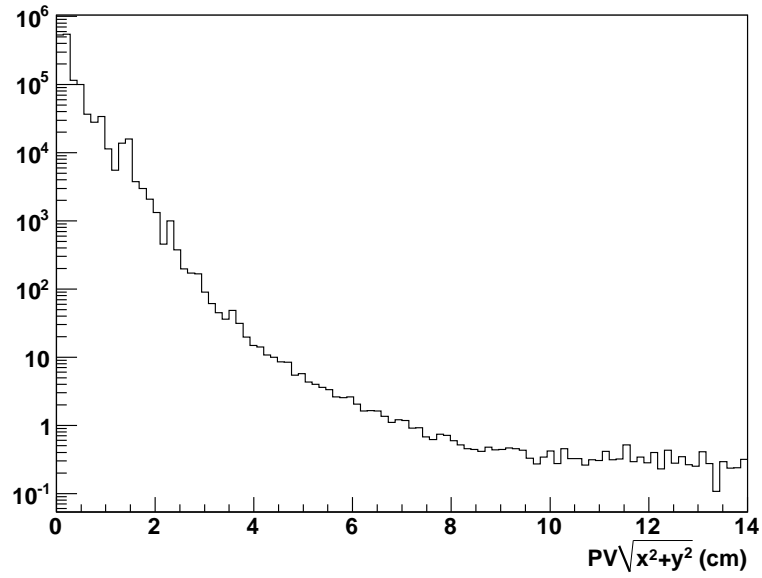


Figure 2.10 : Ratio of RunIIb peak events to tail events versus radial primary vertex position.

### Run2b PV Radial Position

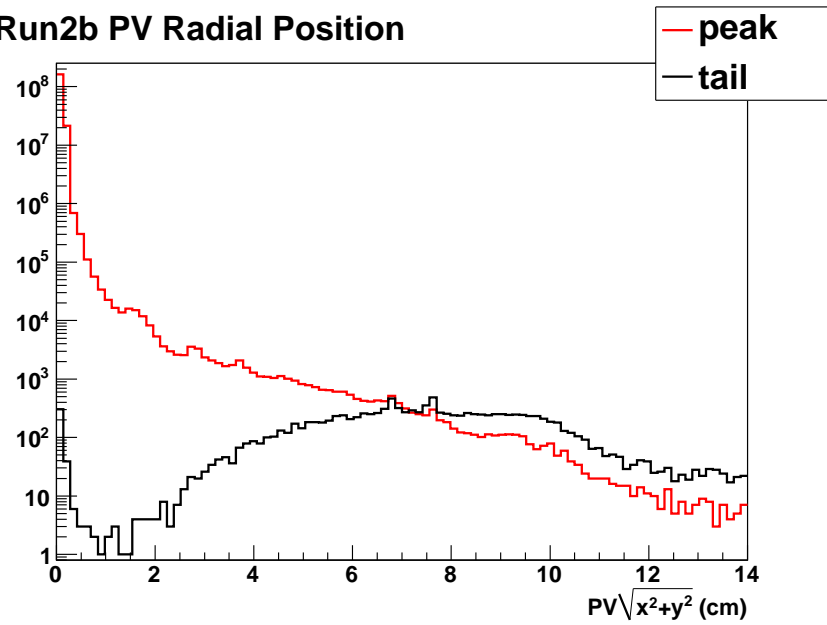


Figure 2.11 : Radial primary vertex position for RunIIb peak and tail events.

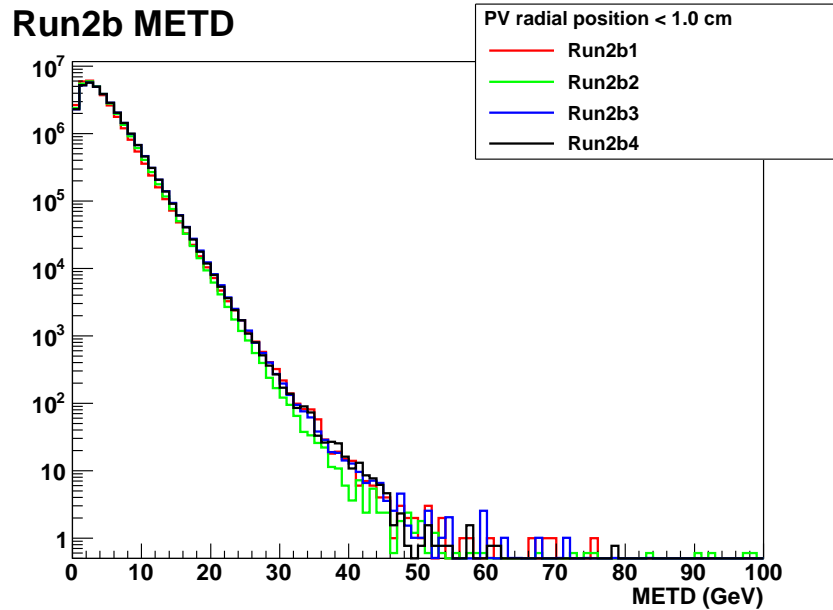


Figure 2.12 : METD distributions for each RunIIb epoch after a primary vertex cut at 1 cm.

cuts on the earlier RunIIb4 data the  $\cancel{E}_T$  distributions can be brought to agreement with earlier epochs.

### 2.3 $\cancel{E}_T$ Certification for Reprocessed Events

After the end of operations at DØ approximately fifteen percent of the total RunIIb data was reprocessed to apply improved calibrations and reconstruction algorithms. The reprocessed data was then certified against the original data to ensure good performance. Reprocessed data was matched to original data using the run and event numbers to ensure a direct event-to-event comparison. With few exceptions, agreement in the  $\cancel{E}_T$  distributions was nearly perfect. The only issues found were in RunIIb1 METMG and METICD, where the reprocessed data showed slightly less  $\cancel{E}_T$  than the original data (Fig. 2.13(e-f)). The origin

of these discrepancies is not clear, however the overall effect on the main  $\mathcal{E}_T$  definitions is negligible (Fig. 2.13(a-d)). Figures 2.13 - 2.16 show the uncorrected (METD) and corrected (CorrMET) versions of  $\mathcal{E}_T$  and scalar  $E_T$  for reprocessed data in each epoch.

Two versions of Monte Carlo were produced to simulate the reprocessed data: RunIIB1 and a combination of RunIIB2,3,4. Comparisons of  $\mathcal{E}_T$  in reprocessed data to reprocessed Monte Carlo show the same type of discrepancies seen in the original data and Monte Carlo (Figs. 2.17 - 2.20). The corrected version of  $\mathcal{E}_T$  from the `ReComputeMET` processor consistently provides the best agreement between data and Monte Carlo, but as seen in these figures there can be 10-20% disagreements even in the high statistics regions of the CorrMET distributions. An attempt to improve the modeling will be discussed in Chapter 5.

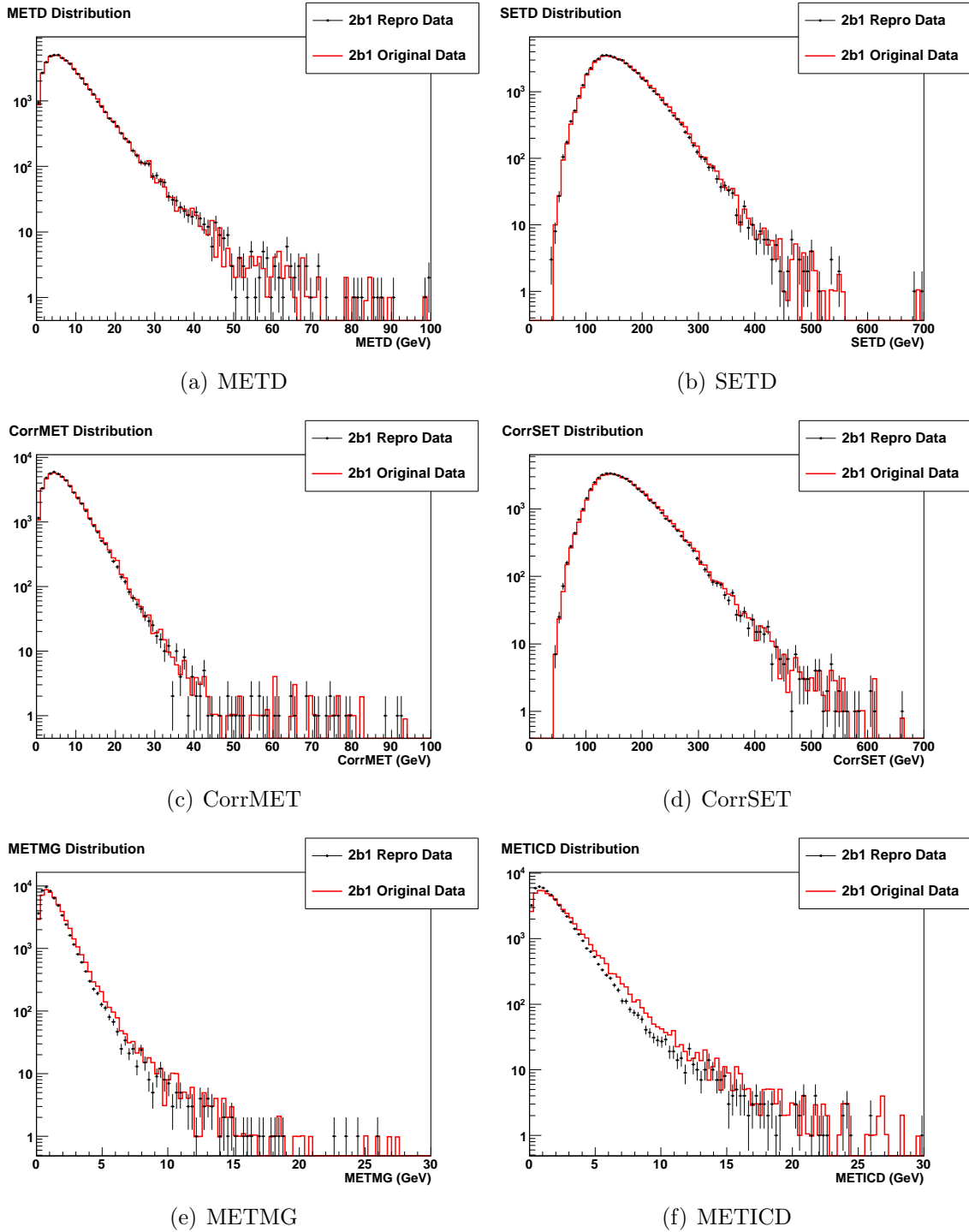


Figure 2.13 : RunIIb1 reprocessed  $Z \rightarrow ee$  data compared to original data. Discrepancies seen in METMG (e) and METICD (f) do not have a noticeable effect on METD (a).

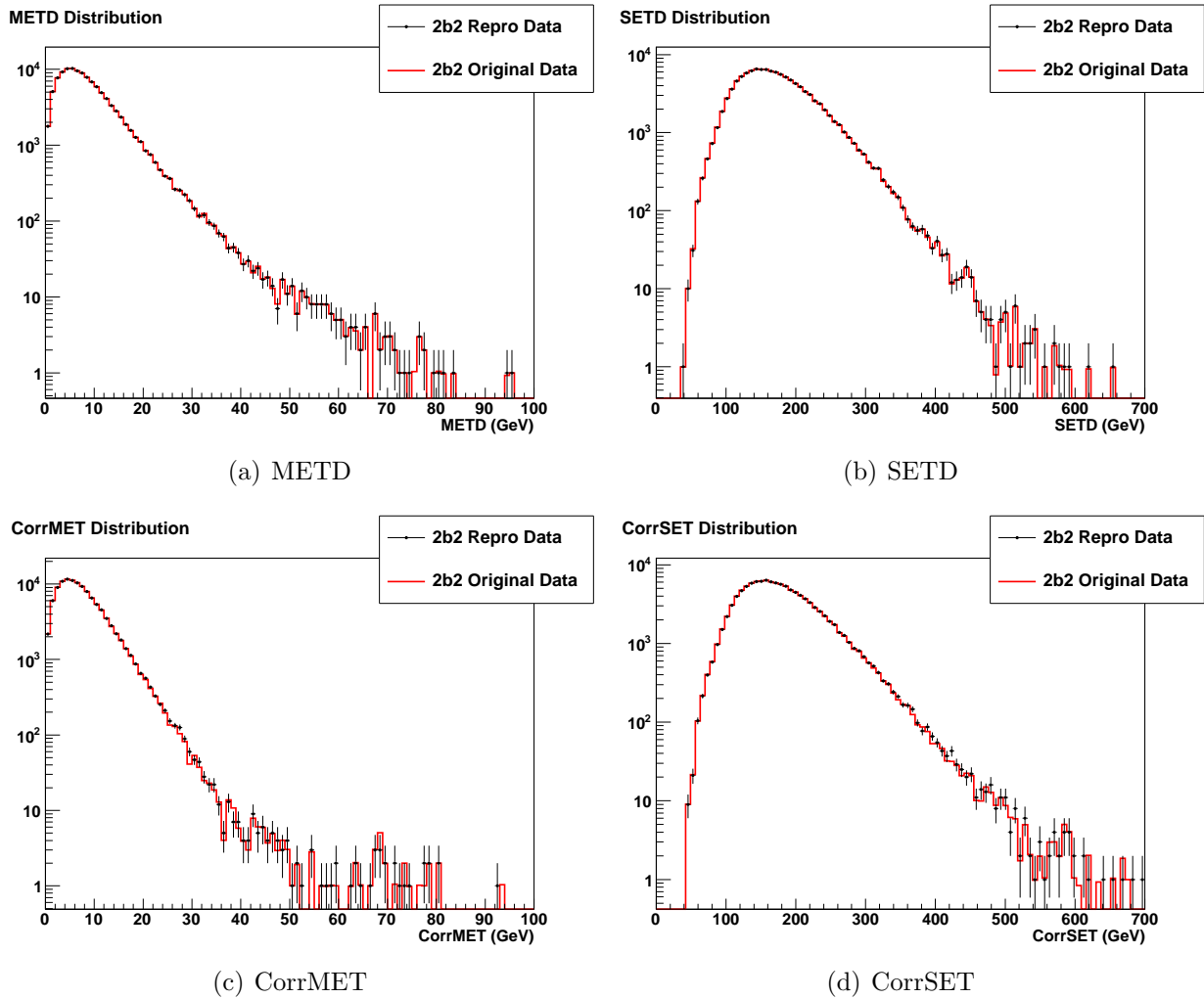


Figure 2.14 : RunIIb2 reprocessed  $Z \rightarrow ee$  data compared to original data.

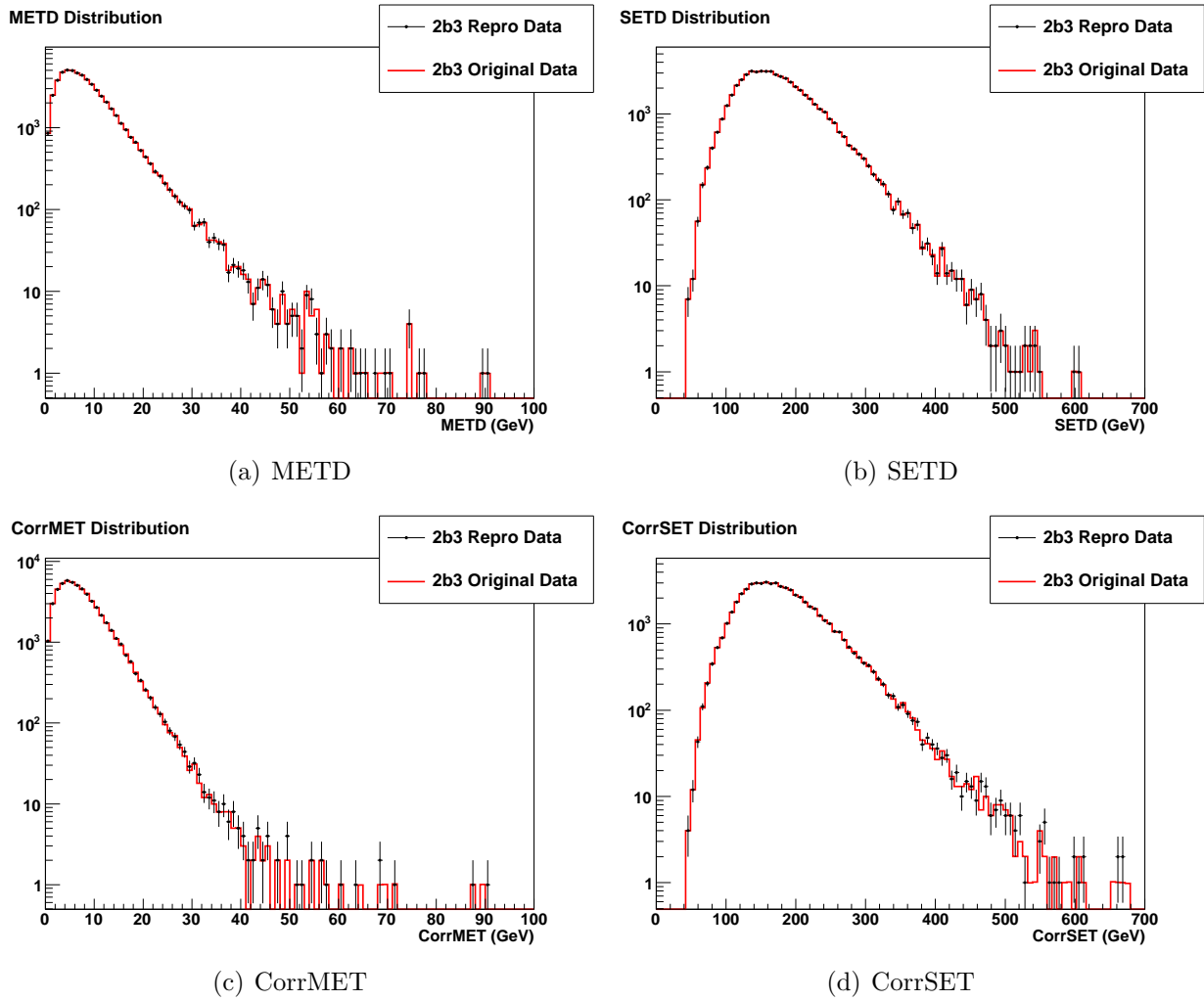


Figure 2.15 : RunIIb3 reprocessed  $Z \rightarrow ee$  data compared to original data.

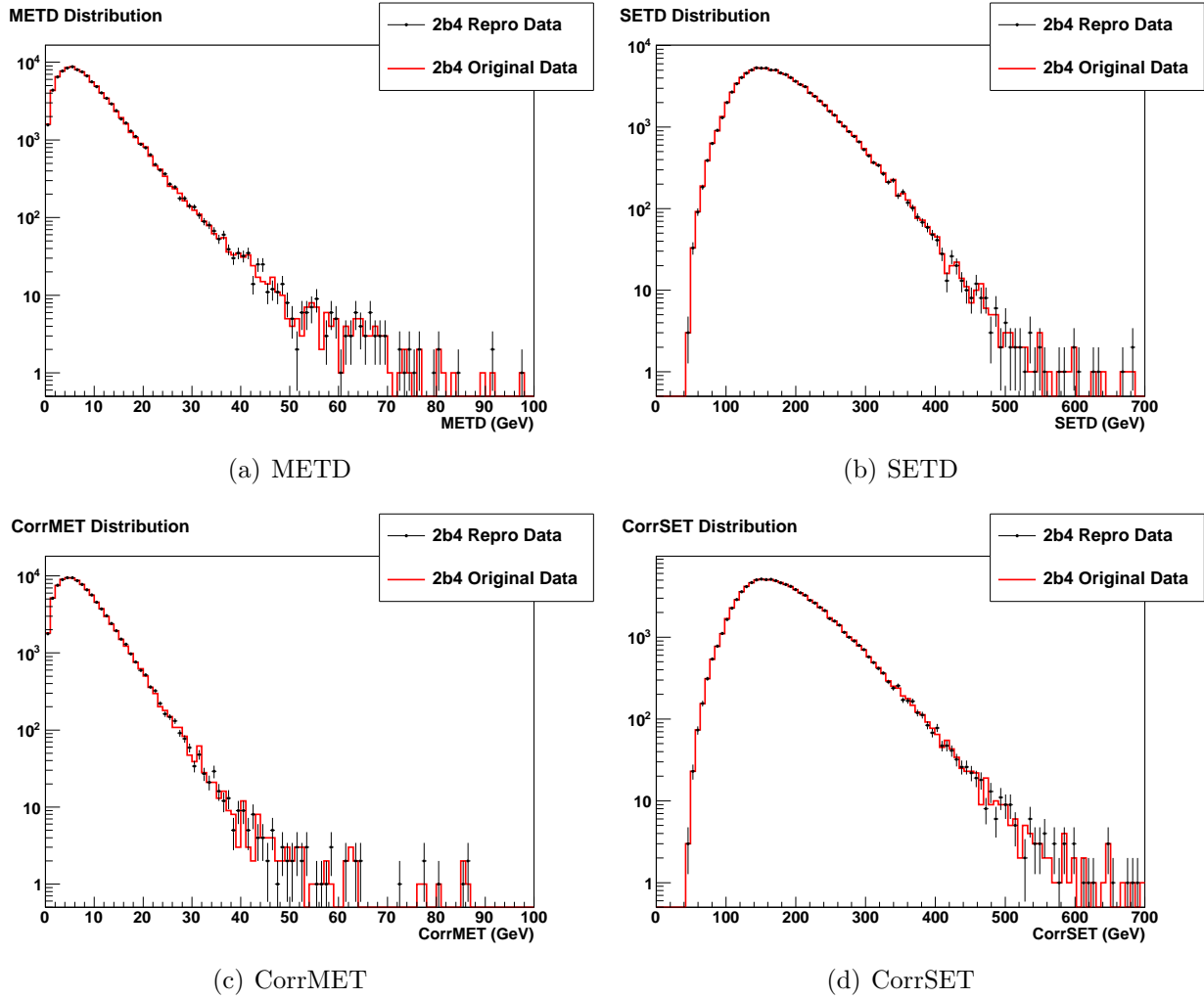


Figure 2.16 : RunIIb4 reprocessed  $Z \rightarrow ee$  data compared to original data.



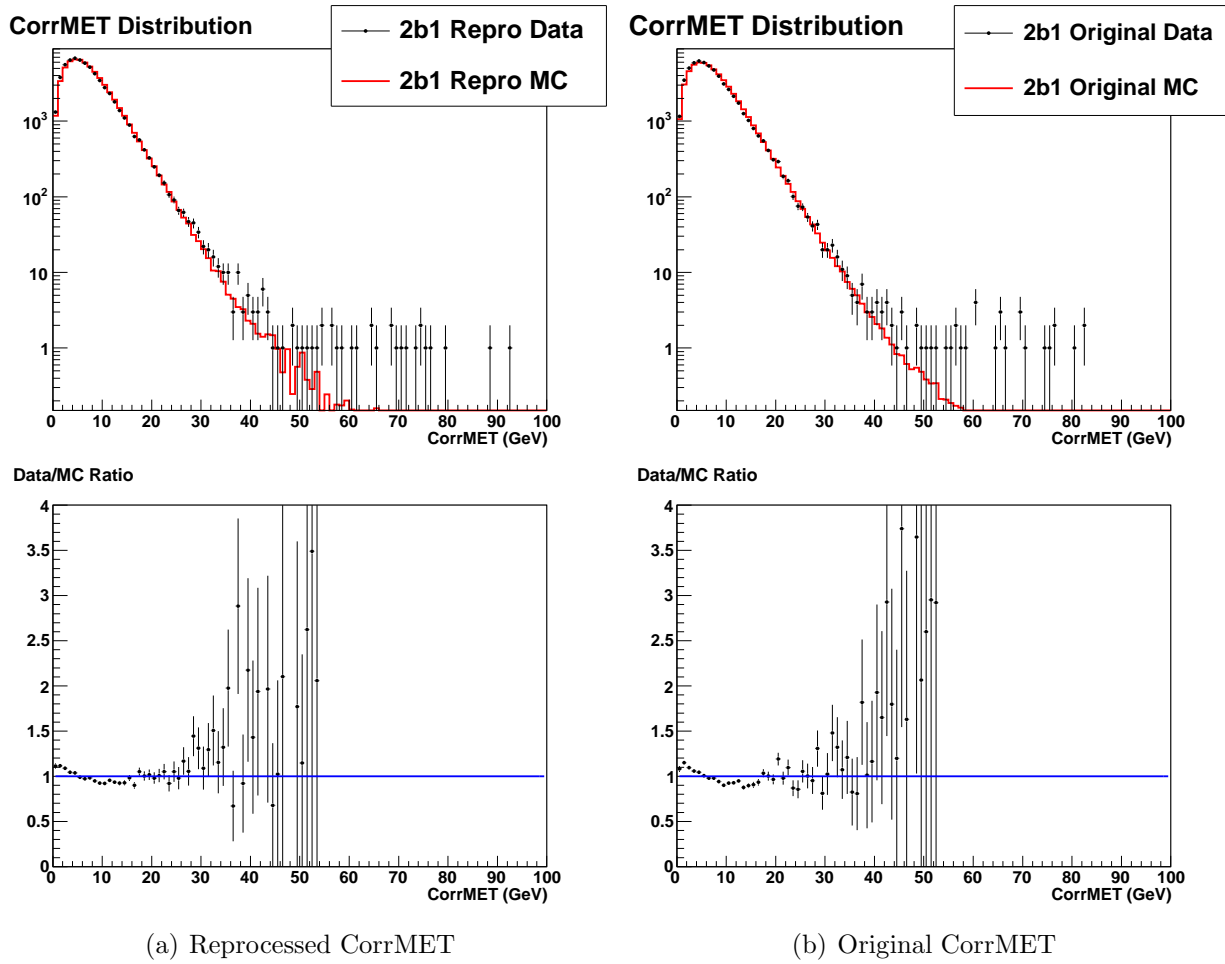


Figure 2.17 : CorrMET in RunIIB1 reprocessed  $Z \rightarrow ee$  data/MC and original data/MC. Agreement in the reprocessed version is similar to that of the original version.

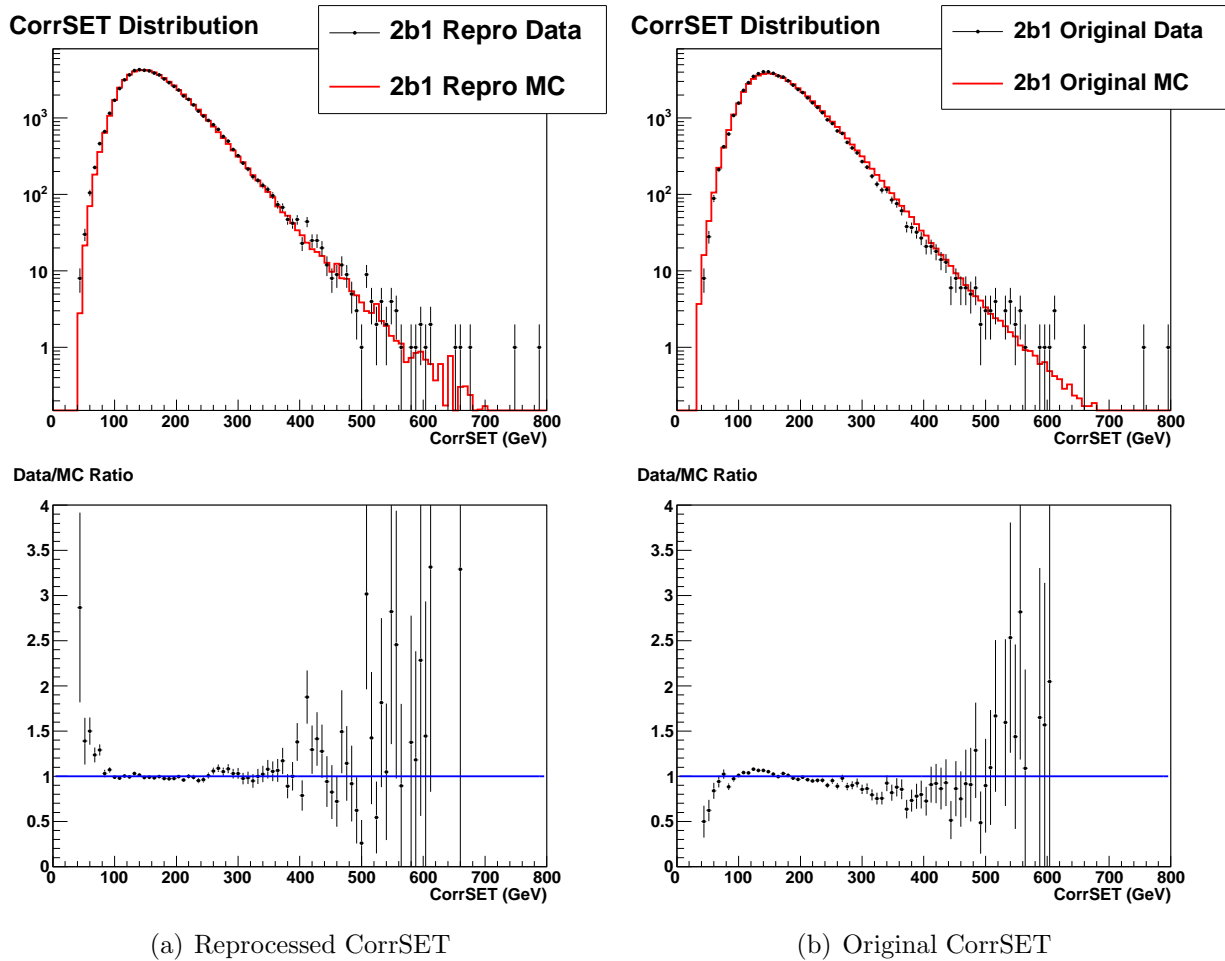


Figure 2.18 : CorrSET in RunIIb1 reprocessed  $Z \rightarrow ee$  data/MC and original data/MC. Agreement in the reprocessed version is similar to that of the original version.

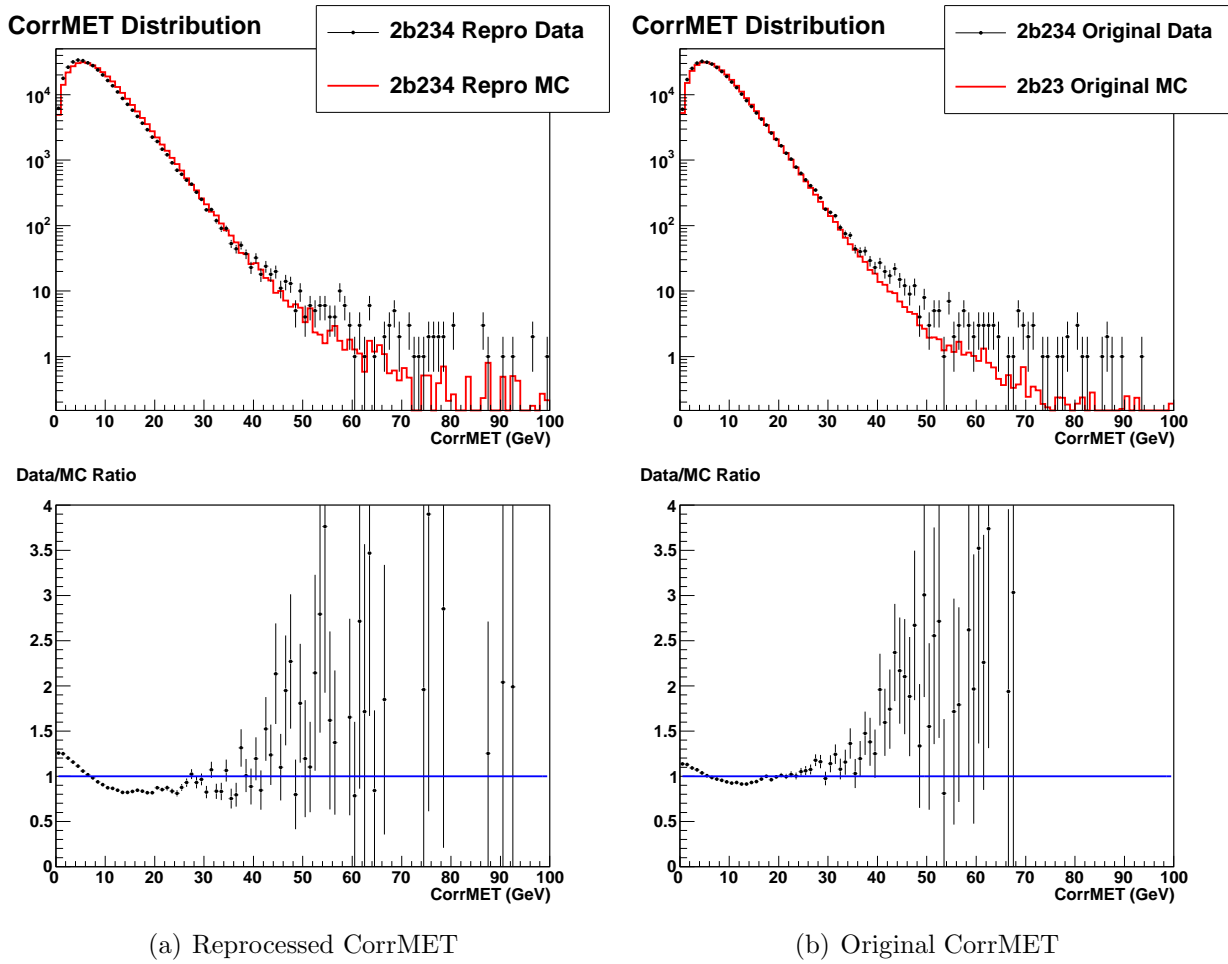


Figure 2.19 : CorrMET in RunIIb2,3,4 reprocessed  $Z \rightarrow ee$  data/MC and original data/MC. Agreement in the reprocessed version is similar to that of the original version.



## Chapter 3

# Unclustered Energy Resolution & Missing $E_T$ Significance

An algorithm known as  $\cancel{E}_T$  significance (METsig) was developed to identify events where it is unlikely that the  $\cancel{E}_T$  originated from a physics process. This algorithm calculates a measurement resolution for  $\cancel{E}_T$ , a key component of which is the resolution for unclustered energy, defined in detail below. While the detector resolutions for the physics objects (jets, muons, and electrons) have been maintained throughout the lifetime of DØ, until recently the unclustered energy resolution used to calculate METsig had not been updated since RunIIa. New resolution functions were derived in 2012 for both RunIIa and RunIIb, and issues discovered in certain analyses spurred a study of the behavior and origin of the older resolution functions.

### 3.1 Unclustered Energy

In all events recorded at DØ there are many energy deposits in the calorimeter which are not included in a reconstructed physics object. The vector sum of transverse energy in these cells is the “unclustered” energy (UE) and the scalar sum is labeled scalar unclustered energy (SUE). UE comes from a variety of sources: jet energy outside reconstruction cones, “soft” particles or jets with energies below the reconstruction thresholds, and “hot” or noisy

calorimeter cells (although data quality information allows rejection of events with excessive noise). In the DØ framework unclustered energy information is stored in a `TMBLeBob` object. Unclustered energy variables from this object will be denoted  $UE_x$ ,  $UE_y$ , and SUE.

The sum of physics object energies and unclustered energy describes all the transverse energy deposited in the calorimeter. Since  $\cancel{E}_T$  is defined as the opposite of this quantity, UE values can be calculated from  $\cancel{E}_T$ , scalar  $E_T$  (SET), and the physics object transverse momenta. This calculated version of unclustered energy will be denoted with lowercase letters:

$$\mathbf{ue} + \sum_{\text{objects}} \mathbf{p}_T = \sum_{\text{calo}} \mathbf{E}_T = -\cancel{\mathbf{E}}_T \quad (3.1)$$

$$\mathbf{ue} = -\cancel{\mathbf{E}}_T - \sum_{\text{leptons}} \mathbf{p}_T - \sum_{\text{jets}} \mathbf{p}_T \quad (3.2)$$

$$sue = SET - \sum_{\text{leptons}} p_T - \sum_{\text{jets}} p_T \quad (3.3)$$

### 3.2 $\cancel{E}_T$ Significance

$\cancel{E}_T$  Significance is a measure of how well  $\cancel{E}_T$  can be described by random fluctuations of the physics objects' energies within their energy resolutions [12]. The DØ detector measures energies of objects such as electrons and photons with good precision, while objects such as jets may have much larger resolutions. The measured value of  $\cancel{E}_T$  alone is often not sufficient to determine whether a real source of missing energy (i.e. a neutrino) was present in the event. METsig combines  $\cancel{E}_T$  with the information from the directions and energy resolutions of the physics objects to present a clearer picture of the source of missing energy in the event.

Assuming each term in the  $\cancel{E}_T$  calculation (Eq. 3.1) is independent of the others, the  $\cancel{E}_T$  resolution will equal a quadrature sum of their resolutions. Since the measured energy of each physics object fluctuates along its direction, which is generally well-measured at  $D\mathcal{O}$ , its contribution to the  $\cancel{E}_T$  resolution is the projection of the object's resolution in the direction of the  $\cancel{E}_T$ . Since UE comes from many small clusters of energy it can theoretically fluctuate in any direction, so no projection of its resolution is taken. Letting  $\sigma_{\text{object}}^2$  represent a physics object's resolution,  $\theta$  the angle between  $\cancel{E}_T$  and the physics object, and  $\sigma_{UE}^2$  the unclustered energy resolution, the  $\cancel{E}_T$  resolution ( $\sigma_{\cancel{E}_T}^2$ ) is written as:

$$\sigma_{\cancel{E}_T}^2 = \sum_{\text{objects}} \sigma_{\text{object}}^2 \cos^2 \theta + \sigma_{UE}^2 \quad (3.4)$$

To calculate METsig the  $\cancel{E}_T$  measurement's probability density function is taken to be a normalized Gaussian distribution,  $\mathcal{N}(\mu, \sigma)$ , centered at the value of  $\cancel{E}_T$  with variance equal to the calculated  $\cancel{E}_T$  resolution. METsig is defined as the natural logarithm of the ratio of two probabilities from this distribution: the probability of  $\cancel{E}_T$  equal to its measured value, and the probability of  $\cancel{E}_T$  equal to zero.

$$p(\cancel{E}_T) = \mathcal{N}(\cancel{E}_T, \sigma_{\cancel{E}_T}) \quad (3.5)$$

$$\text{METsig} \equiv \log \frac{p(\cancel{E}_T = \cancel{E}_{T,\text{meas}})}{p(\cancel{E}_T = 0)} \quad (3.6)$$

In general, events with large  $\cancel{E}_T$  resolutions or small amounts of  $\cancel{E}_T$  will have smaller METsig values. Events with narrow resolutions or large amounts of  $\cancel{E}_T$  will have high METsig values. Larger METsig values indicate a higher probability that the missing energy in the event originated from a physics source. The range of METsig values is determined by the

minimum value of the denominator in Eq. 3.6. To avoid division by zero a lower bound must be placed on that probability. To establish a convenient METsig range of approximately one through ten, the lower bound was traditionally set to:

$$p(\cancel{E}_T = 0) = 1 \times 10^{-4} \quad (3.7)$$

By changing the exponent in this relationship, the range of METsig can be extended and the shape of the distributions will change.

### 3.3 UE Resolution Functions

#### 3.3.1 Derivation Procedure

UE resolution functions are derived from  $Z \rightarrow ee$  events, which have well-measured electrons and no real missing energy. The UE vector can be described in component form in two ways, the simpler of which is  $UE_x$  and  $UE_y$  as defined by the physical positioning of the detector. UE is azimuthally symmetric to within a small effect from longer readout cables below the detector, which require higher noise thresholds. The  $UE_x$  and  $UE_y$  distributions are therefore nearly equivalent and have traditionally been combined to increase statistics. Figure 3.1 gives an example of this procedure: combining  $UE_x$  and  $UE_y$  produces only small changes in the RMS.

UE can also be decomposed onto the axes defined by the transverse momentum of the  $Z$  boson. The component of the unclustered energy parallel to this momentum describes the system's hadronic recoil from the  $Z$  boson. The orthogonal component ( $UE_{\perp}$ ) is a combination of noise, detector fluctuations, and unclustered energy from the underlying



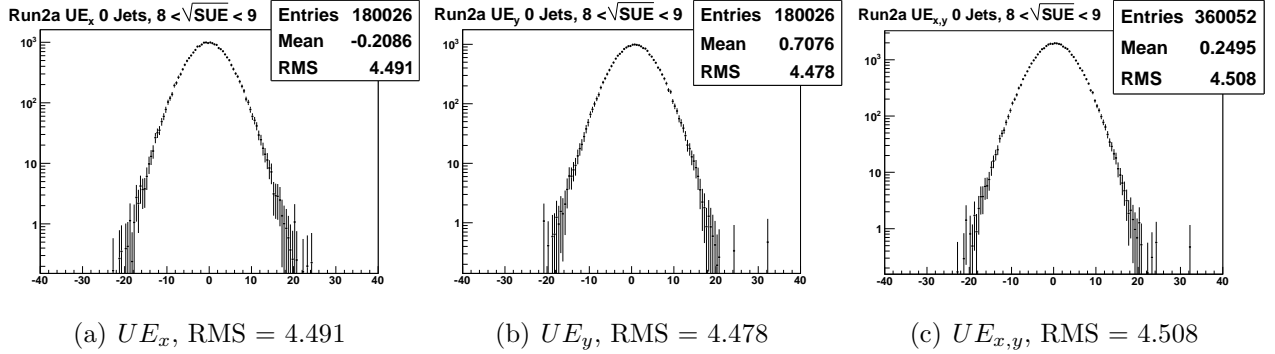


Figure 3.1 :  $UE_x$  (a) and  $UE_y$  (b) distributions are nearly equivalent and have traditionally been combined to derive UE resolution functions. In this example of RunIIa MC events with 0 jets, combination (c) increased the RMS of the bin ( $8 < \sqrt{SUE} < 9$ ) by less than one percent.

event. Using this component allows calculation of the UE detector resolution with less influence from the type of event.  $UE_{\perp}$  is constructed as follows:

$$Z_x = \sum_{\text{electrons}} p_x \quad (3.8)$$

$$Z_y = \sum_{\text{electrons}} p_y \quad (3.9)$$

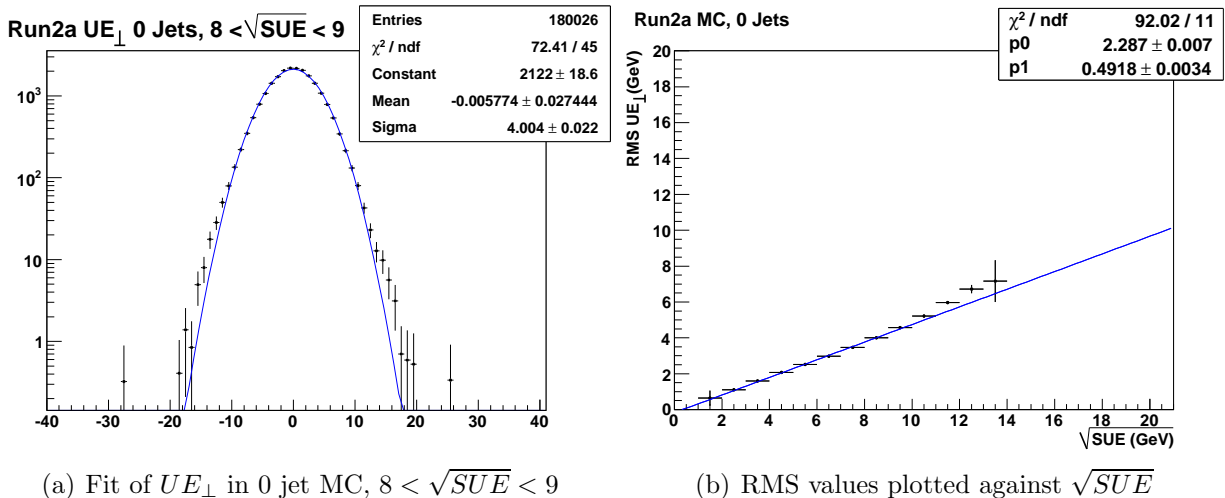
$$Z = \sqrt{Z_x^2 + Z_y^2} \quad (3.10)$$

$$UE_{\perp} = \frac{1}{Z}(UE_y Z_x - UE_x Z_y) \quad (3.11)$$

Because energy surrounding reconstructed jet cones is a major component of unclustered energy, a UE resolution function is derived separately for cases of 0, 1, and 2 or more jets. Events are further separated into bins of scalar unclustered energy (specifically  $\sqrt{SUE}$ ) and for each bin a histogram is filled with the values of a UE component ( $UE_{\perp}$  or  $UE_{x,y}$ ). These distributions have a Gaussian shape which is fitted using the ROOT program [13]. The fitted width of this Gaussian is the resolution value for that  $\sqrt{SUE}$  bin. The UE resolution

function is the function which describes the relationship between the fitted RMS values and  $\sqrt{SUE}$ . The parameters of a polynomial fit define a parametrization used in METsigAlg.

Figure 3.2 demonstrates this procedure for 0 jet events in RunIIa  $Z \rightarrow ee$  Monte Carlo.



(a) Fit of  $UE_{\perp}$  in 0 jet MC,  $8 < \sqrt{SUE} < 9$

(b) RMS values plotted against  $\sqrt{SUE}$

Figure 3.2 : Gaussian fits are performed on UE distributions in each bin of  $\sqrt{SUE}$  (a). The  $\sigma$  value and its uncertainty are plotted as a function of  $\sqrt{SUE}$  (b). The linear fit parameters are used in METsigAlg to calculate the UE resolution.

### 3.3.2 2012 RunIIa & RunIIb Resolutions

$Z \rightarrow ee$  events were selected according to the following criteria from the datasets listed in Tab. 3.1 and Tab. 3.2.

- 2 Point1 electrons [14]
- opposite sign electrons
- electron and jet  $p_T > 15$  GeV

- $75 \text{ GeV} < \text{dielectron mass} < 110 \text{ GeV}$
- primary vertex radial position  $< 1.0 \text{ cm}$

Electrons are selected using a “working point” (Point0, Point05, Point1, Point2), which is a collection of electron identification and quality requirements [14]. The requirements grow stricter at each successive working point. The Point1 definition requires that the energy cluster in the electromagnetic calorimeter match a track in the central tracking system.

All RunIIb epochs were combined, and it was determined (Fig. 3.3) that the resolutions did not show significant luminosity dependence. All  $Z \rightarrow ee$  events meeting the selection criteria in the complete  $D\bar{O}$  dataset were used in the derivation.

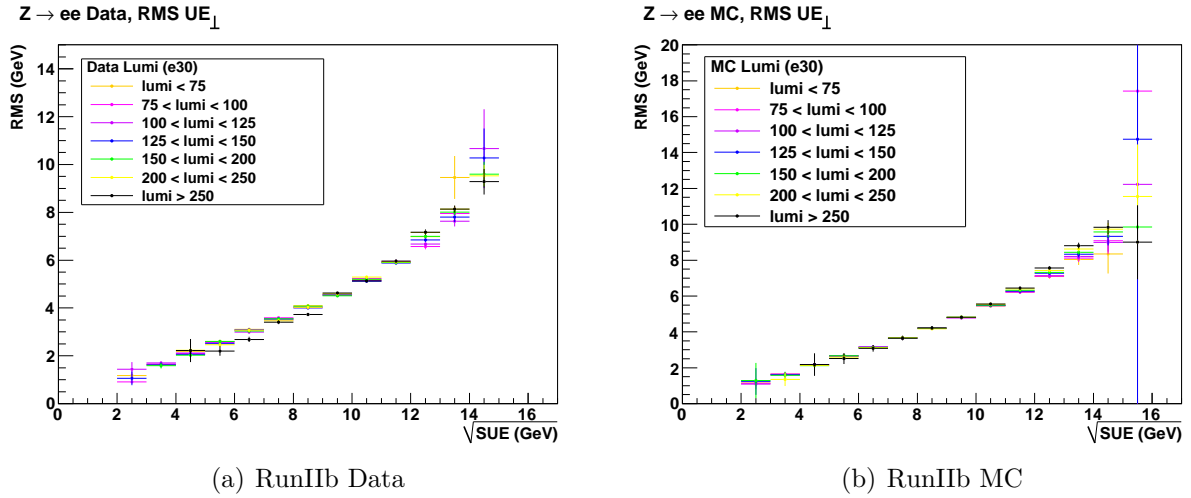


Figure 3.3 : RMS of  $UE_{\perp}$  in RunIIb  $Z \rightarrow ee$  events in several luminosity bins. The distributions overlap sufficiently that luminosity bins were deemed unnecessary for the RunIIb UE resolution functions.

In RunIIa, linear fits of the  $UE_{\perp}$  resolution in bins of  $\sqrt{SUE}$  gave the best description of the data. Fit variable  $\sqrt{SUE} - 5$  was used for consistency with previous convention.

Data Epoch	SAM Definition	0 jets	1 jet	2+ jets
RunIIa	CSG_CAF_2EMhighpt_PASS3	50235	11269	2851
RunIIb1	CSG_CAF_2EMhighpt_PASS2	44879	10676	2778
RunIIb2	CSG_CAF_2EMhighpt_PASS4	92451	24702	7230
RunIIb3	CSG_CAF_2EMhighpt_PASS5	65890	17727	5181
RunIIb4	CSG_CAF_2EMhighpt_PASS6	79344	21120	6903
RunIIb Total		282564	74225	22092

Table 3.1 : Data samples used to derive UE resolutions

MC Epoch	SAM Definition	0 jets	1 jet	2+ jets
	CSG_alpgepythia_gamz_ee_75_130_			
RunIIa	p181400_v12	1294278	523195	248054
RunIIb1	p211100_v12	4888894	2017022	831796
RunIIb2	p211800_Run2b2_v6	2277634	803296	287149
RunIIb3	p212100_Run2b3_v3	1810744	630164	231810
RunIIb Total		8977272	3450482	1350755

Table 3.2 : Monte Carlo samples used to derive UE resolutions

For RunIIb, better fits were achieved by linear fits in bins of SUE. Resolution functions for RunIIa and RunIIb are listed in Tabs. 3.3 and 3.4, with fits shown in Figs. 3.4 and 3.5.

### 3.3.3 2006 RunIIa Resolutions

The original unclustered energy resolution functions were derived in 2006 for the top quark group, using the calculated version of UE and decomposing the  $ue$  vector along the standard  $x$  and  $y$  axes rather than finding  $ue_{\perp}$ . The presentation of the derivation by Peter Renkel [15] notes the following selection criteria, but not specific data samples.

- 2 tight electrons
- opposite sign electrons
- $p_T$  of second electron  $> 15$  GeV
- $p_T$  of second jet (or only jet in 1-jet events)  $> 20$  GeV

The 2006 resolution functions, which were used in `METsigAlg` from its creation in 2007 until 2012, are summarized in Tab. 3.5.

### 3.3.4 2007 RunIIa Resolutions

In January 2007, Renkel presented updated UE resolution parameters with improvements in the 2 or more jet bin [16]. Data to Monte Carlo agreement was substantially improved with the update, and the slope parameters in the 2 or more jet bin were decreased by approximately a factor of two, bringing them more in line with slope parameters in the other

N jets	Type	p0	p1
0 jet	Data	$2.184 \pm 0.009$	$0.4374 \pm 0.0047$
	MC	$2.287 \pm 0.007$	$0.4918 \pm 0.0034$
1 jet	Data	$2.99 \pm 0.03$	$0.5256 \pm 0.0145$
	MC	$2.774 \pm 0.022$	$0.5765 \pm 0.0087$
2+ jet	Data	$3.259 \pm 0.097$	$0.536 \pm 0.041$
	MC	$2.995 \pm 0.065$	$0.6376 \pm 0.0198$

Table 3.3 : RunIIa UE Resolution Functions.  $\sigma_{UE_{\perp}} = p0 + p1(\sqrt{SUE} - 5)$ . The resolution grows, as seen in both  $p0$  and  $p1$  values, with increases in jet multiplicity.

N jets	Type	p0	p1
0 jet	Data	$1.432 \pm 0.011$	$0.03292 \pm 1.7 \times 10^{-4}$
	MC	$1.48 \pm 0.01$	$0.03571 \pm 1.5 \times 10^{-4}$
1 jet	Data	$2.323 \pm 0.032$	$0.03128 \pm 3.9 \times 10^{-4}$
	MC	$2.007 \pm 0.029$	$0.03543 \pm 3.5 \times 10^{-4}$
2+ jet	Data	$2.487 \pm 0.07$	$0.03158 \pm 7.6 \times 10^{-4}$
	MC	$2.302 \pm 0.074$	$0.03544 \pm 7.6 \times 10^{-4}$

Table 3.4 : RunIIb UE Resolution Functions.  $\sigma_{UE_{\perp}} = p0 + p1 * SUE$ . As jet multiplicity increases the resolution grows, as seen in the  $p0$  values.

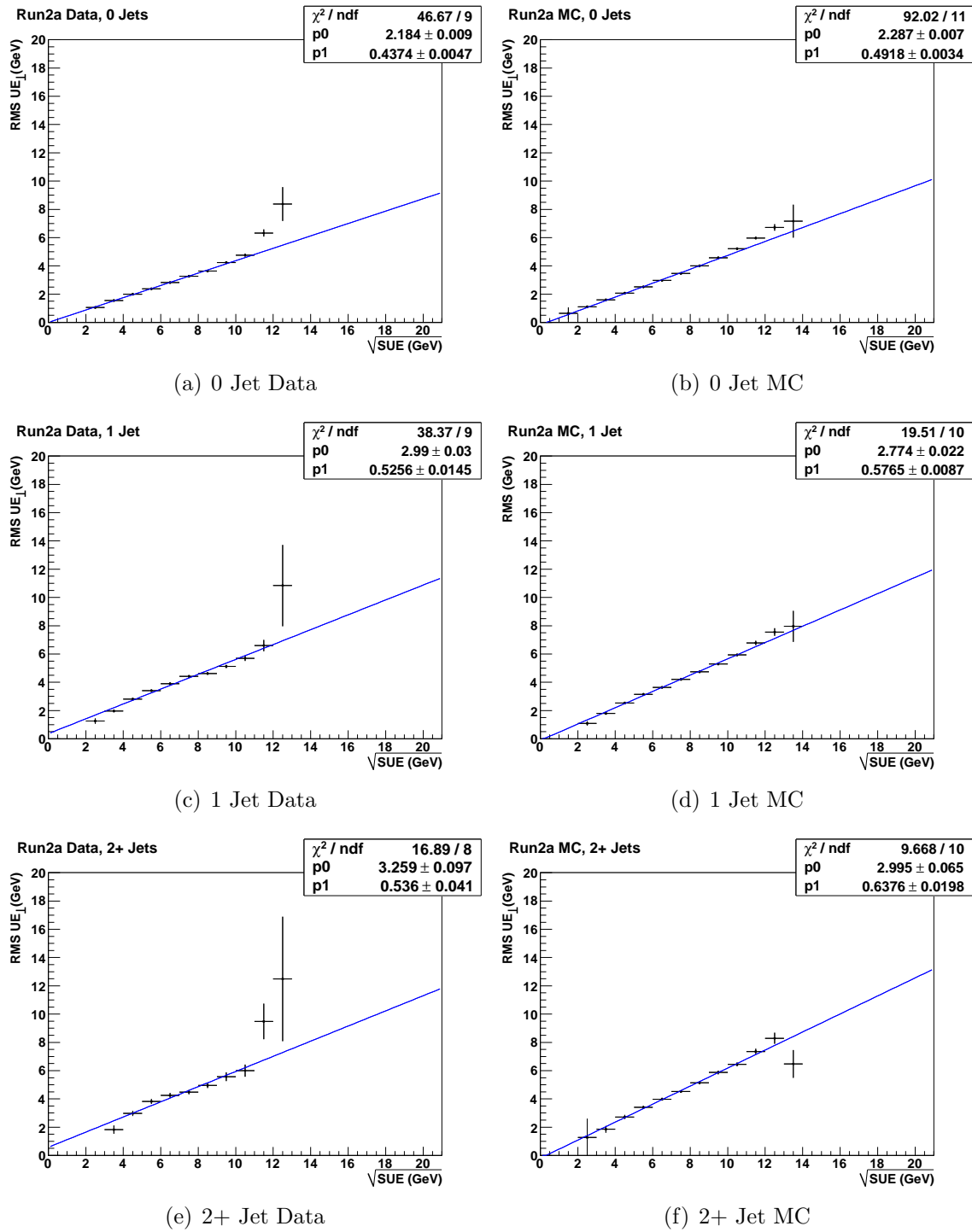
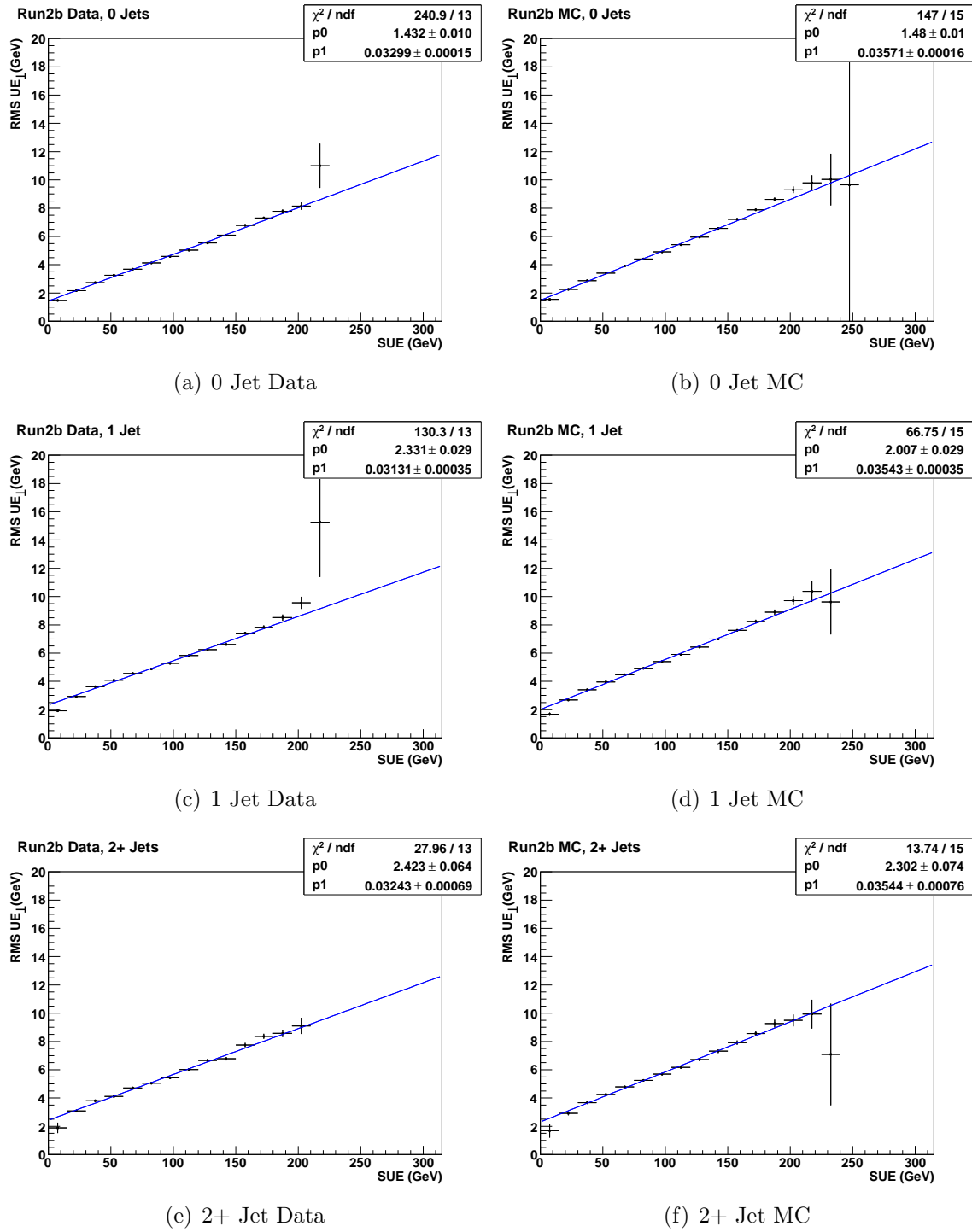


Figure 3.4 : RunIIa RMS of  $UE_{\perp}$  in bins of  $\sqrt{SUE}$  with linear fits.

Figure 3.5 : RunIIb RMS of  $UE_{\perp}$  in bins of SUE, with linear fits.



N jets	Type	p0	p1
0 jet	Data	2.1	0.4
	MC	2.1	0.4
1 jet	Data	3.0	0.5
	MC	3.2	0.6
2+ jet	Data	3.0	1.7
	MC	4.0	1.1

Table 3.5 : October 2006 UE Resolution Functions.  $\sigma_{ue_{x,y}} = p0 + p1(\sqrt{sue} - 5)$

jet cases. The updated functions are summarized in Tab. 3.6. The 2007 functions are more reproducible in the current framework (Fig. 3.6), however this update was never propagated to METsigAlg.

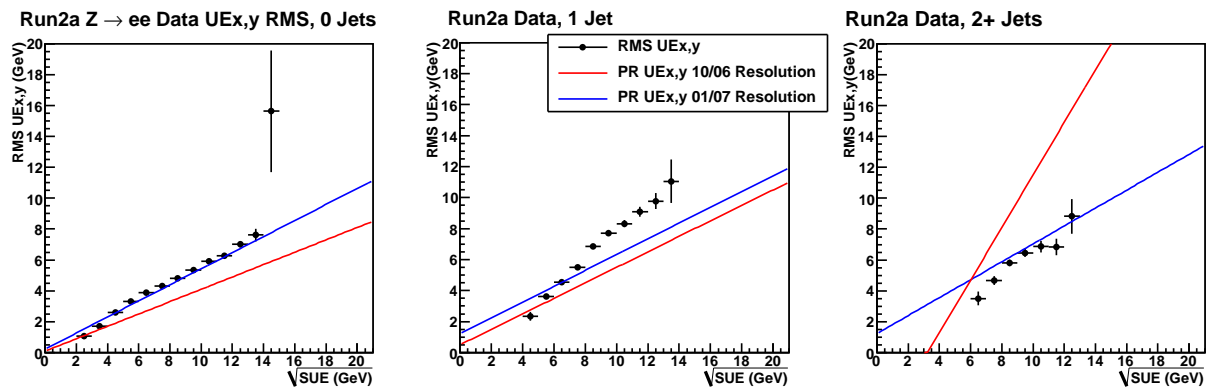


Figure 3.6 : RMS of  $ue_{x,y}$  versus  $\sqrt{sue}$  in RunIIa  $Z \rightarrow ee$  data events (0, 1, and 2+ jets) compared to UE resolution functions from October 2006 and January 2007.

N jets	Type	p0	p1
0 jet	Data	$2.83 \pm 0.02$	$0.52 \pm 0.08$
	MC	1.97	0.65
1 jet	Data	$3.77 \pm 0.07$	$0.51 \pm 0.024$
	MC	3.06	0.60
2+ jet	Data	$4.14 \pm 0.19$	$0.58 \pm 0.065$
	MC	4.38	0.52

Table 3.6 : January 2007 UE Resolution Functions.  $\sigma_{ue_{x,y}} = p0 + p1(\sqrt{sue} - 5)$

## 3.4 Effect on $\cancel{E}_T$ Significance

### 3.4.1 Jet-Inclusive Comparison

Effects on  $\cancel{E}_T$  significance of switching from the 2006 resolution functions to the 2012 functions were tested on the RunIIa and RunIIB3 samples listed in Tab. 3.7.  $Z \rightarrow ee$  events were selected with the same criteria listed in section 3.3.2.  $W \rightarrow e\nu$  Monte Carlo events were required to have exactly one Point1 electron, and QCD data events were required to have exactly one Point0 electron and pass one of several jet triggers which define the “QCD” data skim. The Point0 electron definition has looser requirements than Point1 and does not require that the energy cluster be matched to a track.

Figure 3.7 shows that in  $Z \rightarrow ee$  events the main effect of using the new resolutions was a decrease of high METsig events, which is appropriate since well-measured  $Z \rightarrow ee$  events

Name	Epoch	SAM Definitions	N events
$Z \rightarrow ee$ MC	RunIIa	CSG_alpgenpythia_w_lnu_p181400_v12	32854
	RunIIb3	CSG_alpgenpythia_w_lnu_p212100_Run2b3_v3	25994
2EM Data	RunIIa	CSG_CAF_2EMhighpt_PASS3_p18.14.00	64364
	RunIIb3	CSG_CAF_2EMhighpt_PASS5_p21.18.00_p20.16.08	38135
$W \rightarrow e\nu$ MC	RunIIa	CSG_alpgenpythia_w_lnu_p181400_v12	32355
	RunIIb3	CSG_alpgenpythia_w_lnu_p212100_Run2b3_v3	16415
QCD Data	RunIIa	CSG_CAF_QCD_PASS3_p18.14.00	34143
	RunIIb3	CSG_CAF_QCD_PASS5_p21.18.00_p20.16.08	35541

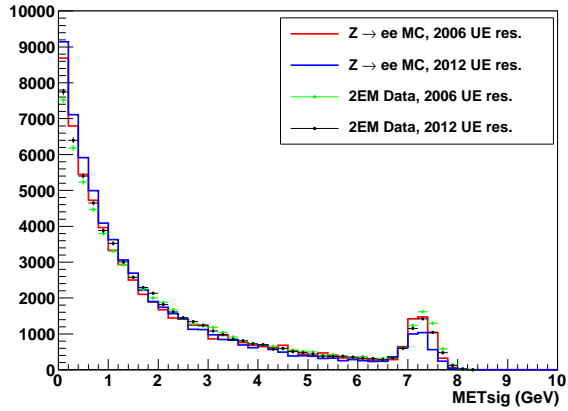
Table 3.7 :  $\cancel{E}_T$  significance UE resolution test samples

should not have  $\cancel{E}_T$  from any physics process. METsig in  $W \rightarrow e\nu$  Monte Carlo events changes slightly: the double peak structure seen when using the old resolutions broadens into a single peak. QCD data events do not show any significant change in METsig.

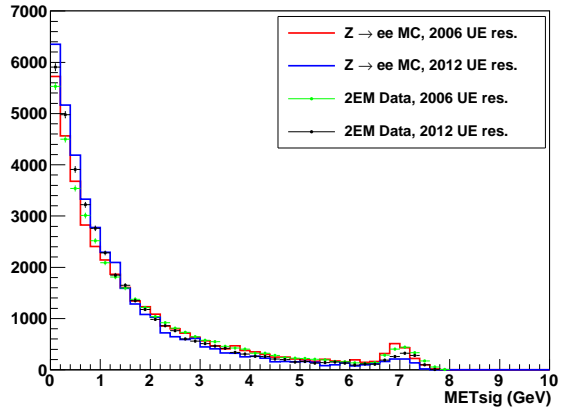
### 3.4.2 Issues in 2+ Jet Case

For analyses interested exclusively in the case of two or more jets, separation between multijet data and high METsig signal samples was negatively affected by using the 2012 UE resolutions, especially when a high  $\cancel{E}_T$  requirement is added (Fig. 3.8(e-f)). This issue was identified in the  $ZH \rightarrow \nu\bar{\nu}b\bar{b}$  Higgs boson analysis and made it clear that the 2006 resolution functions were not well understood.

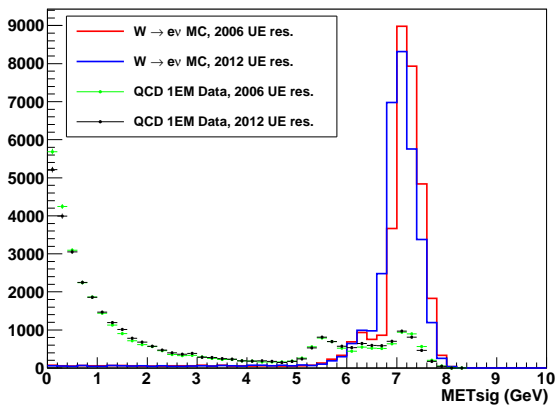
Run2a UE Resolution Comparison

(a) RunIIa  $Z \rightarrow ee$ 

Run2b3 UE Resolution Comparison

(b) RunIIb3  $Z \rightarrow ee$ 

Run2a UE Resolution Comparison

(c) RunIIa  $W \rightarrow e\nu$  and QCD

Run2b3 UE Resolution Comparison

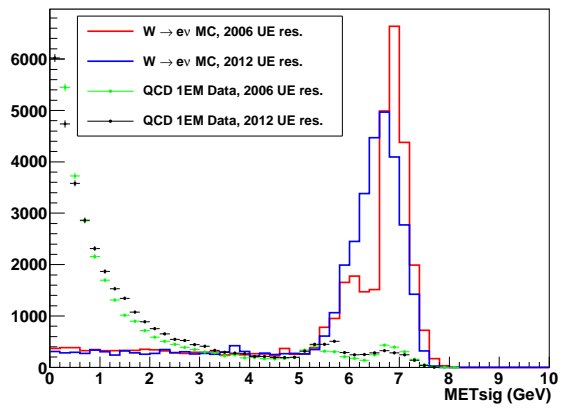
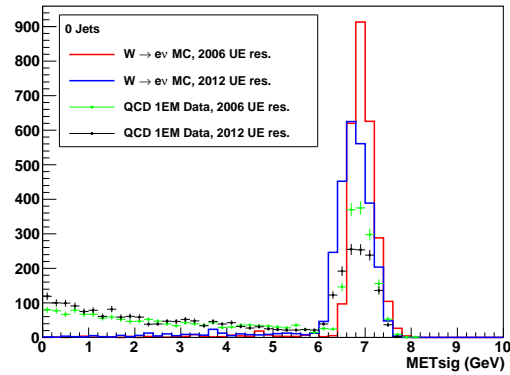
(d) RunIIb3  $W \rightarrow e\nu$  and QCD

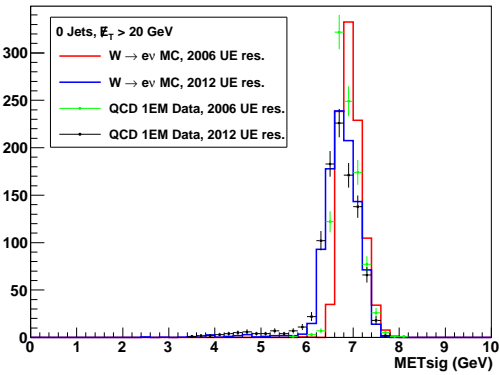
Figure 3.7 :  $\cancel{E}_T$  significance distributions with 2006 and 2012 UE resolutions in  $Z \rightarrow ee$  data/MC (a-b),  $W \rightarrow e\nu$  MC, and QCD data (c-d).

Run2b3 UE Resolution Comparison

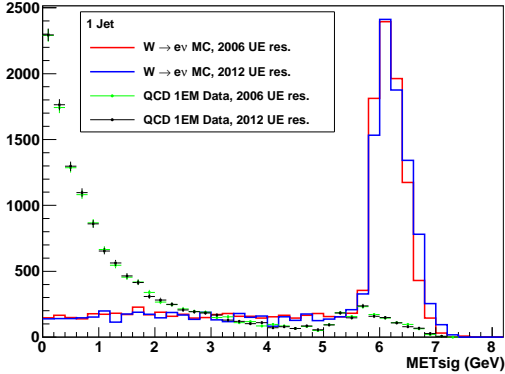


(a) 0 jets

Run2b3 UE Resolution Comparison

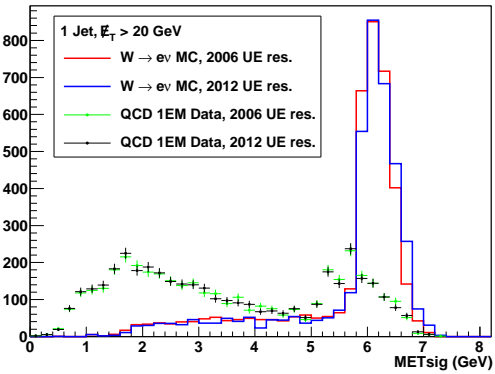
(b) 0 jets,  $\cancel{E}_T > 20$  GeV

Run2b3 UE Resolution Comparison

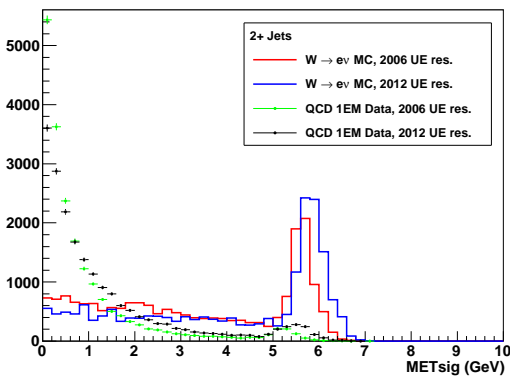


(c) 1 jet

Run2b3 UE Resolution Comparison

(d) 1 jet,  $\cancel{E}_T > 20$  GeV

Run2b3 UE Resolution Comparison



(e) 2 or more jets

Run2b3 UE Resolution Comparison

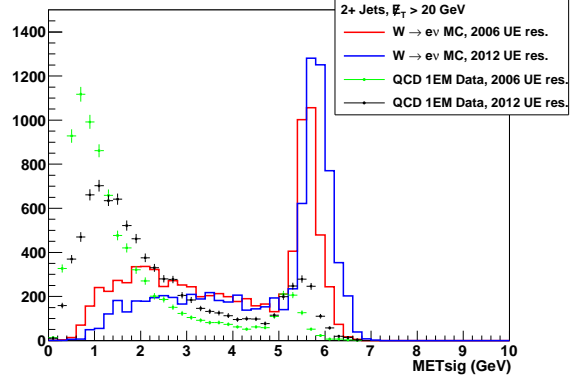
(f) 2 or more jets,  $\cancel{E}_T > 20$  GeV

Figure 3.8 :  $\cancel{E}_T$  significance distributions in each jet case with 2006 and 2012 UE resolutions in RunIIb3  $W \rightarrow e\nu$  MC and QCD data. The 2+ jet case (e), especially combined with high  $\cancel{E}_T$  (f), shows QCD events moving into the  $W$  boson region.

### 3.4.3 Resolution Function Comparison in $ZH \rightarrow \nu\bar{\nu}b\bar{b}$ Samples

The effects on METsig of all UE resolution parameter sets were tested using two samples from the  $ZH \rightarrow \nu\bar{\nu}b\bar{b}$  analysis. A “multijet” selection on data from the New Physics skim and a “signal” selection on  $W \rightarrow l\nu$  Monte Carlo were performed according to criteria detailed by the  $ZH \rightarrow \nu\bar{\nu}b\bar{b}$  group [17]. Of importance in this study is that both selections required two or more jets. The data samples are listed in Tab. 3.8.

While the “true” UE resolution of any given sample will vary based on selection criteria, ideally the resolution parameters in `METsigAlg` will produce a reasonable estimate of the true resolution. The true resolution function is derived using the procedure from section 3.3.1, with UE from `TMBLeBob` and  $x, y$  components. The width of the  $UE_{x,y}$  distribution in bins of  $\sqrt{SUE}$  is fitted with a polynomial. Figure 3.9 compares the true UE resolutions of these samples to the three available resolution functions. The 2006 function consistently overestimates the true resolution, driving METsig values down. Because of data/MC disagreement in the 2006 function this effect on METsig will be more pronounced in data distributions.

Figure 3.10 compares METsig calculated using the true UE resolutions to METsig calcu-

Name	SAM Definition	N events
Multijet	CSG_CAF_NP_PASS5_p21.18.00_p20.16.08	44924
Signal	CSG_alpgenpythia_w+2lp_lnu+2lp_Run2b3_v3	10317

Table 3.8 :  $ZH \rightarrow \nu\bar{\nu}b\bar{b}$  samples.

lated using the three available resolutions. It is clear from these comparisons that the 2006 resolutions are a poor estimate of the true METsig of these samples, and that either the 2007 or 2012 parameterizations are reasonable choices.

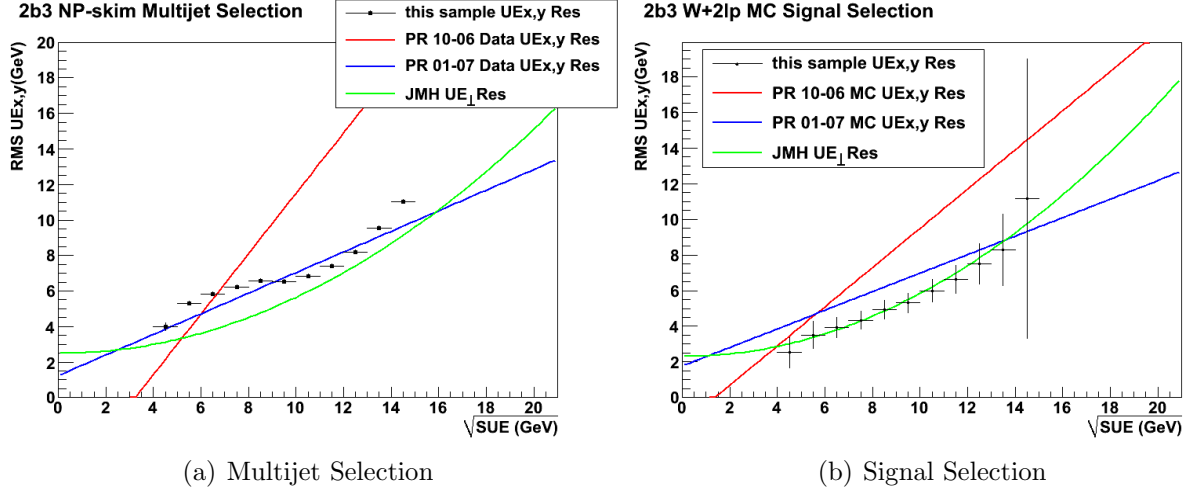


Figure 3.9 : UE Resolution comparison in a  $ZH \rightarrow \nu\bar{\nu}b\bar{b}$  multijet and signal selection

Figure 3.10 confirms that the true METsig of the  $ZH \rightarrow \nu\bar{\nu}b\bar{b}$  samples is not as effective for separating multijet events from signal-like events as METsig calculated using the 2006 UE resolution functions. To some extent this effect is dependent on the minimum probability used in the METsig calculation (Eq. 3.7). For the case of the  $ZH \rightarrow \nu\bar{\nu}b\bar{b}$  samples, separation of multijet and signal-like events similar to that achieved by using the 2006 UE resolutions can be reproduced by extending the traditional limit to  $1 \times 10^{-6}$  or  $1 \times 10^{-8}$  [18]. Figure 3.11 compares METsig for these two samples with four different limits.

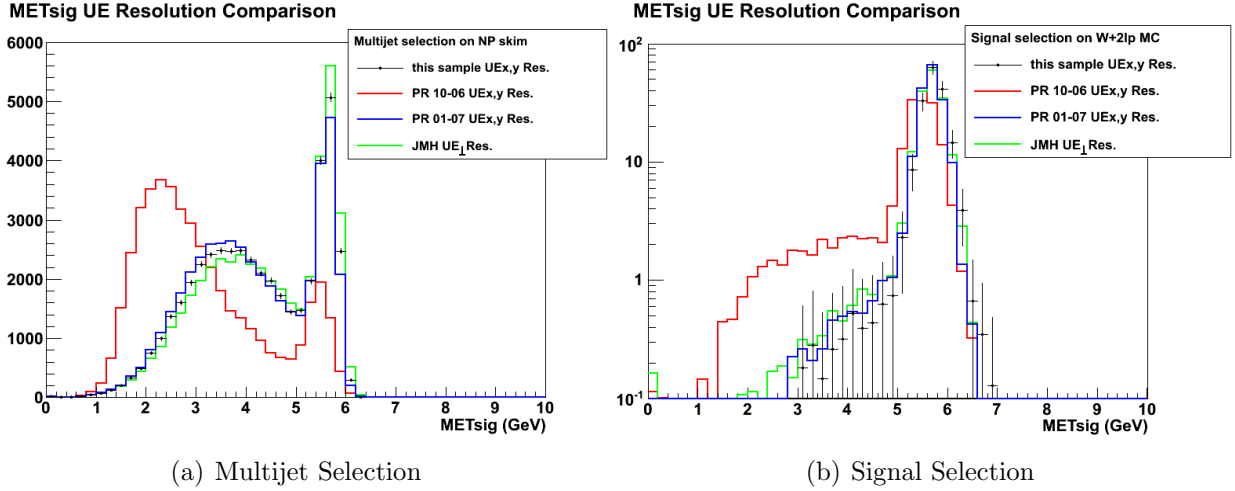


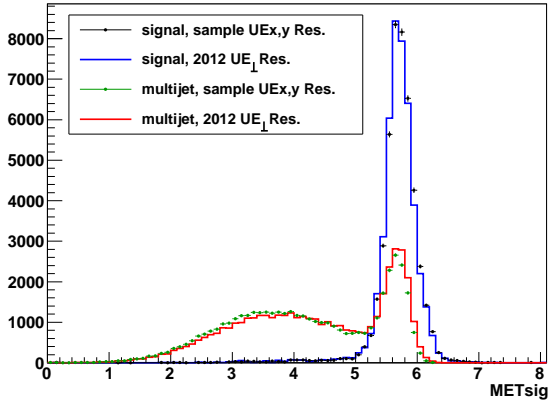
Figure 3.10 :  $\cancel{E}_T$  significance comparison in a  $ZH \rightarrow \nu\bar{\nu}b\bar{b}$  multijet and signal selection

### 3.5 Summary & Application

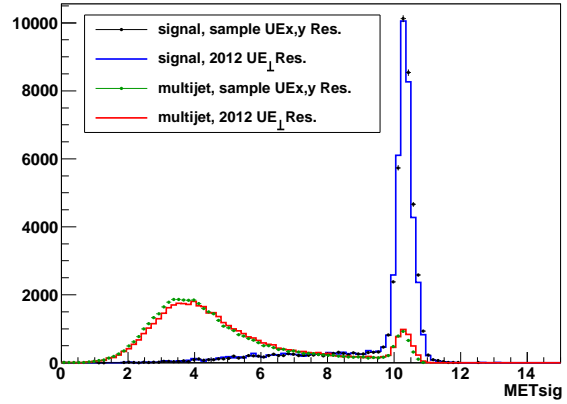
Unclustered energy resolution functions have now been derived for use with RunIIb data and Monte Carlo, dependent on the number of jets and the value of scalar unclustered energy. Resolution functions for RunIIa were shown to overestimate the unclustered energy resolution in two jet samples, so new functions were also derived for RunIIa data and Monte Carlo. While the update to these resolution parameters caused a loss of separation power for two jet analyses, by adding the option for a flexible minimum probability this problem has been resolved.

In the  $D\bar{O}$  analysis framework  $\cancel{E}_T$  significance is calculated by the `METsigAlg` processor, which calculates uses the known values of SUE and the number of jets to set the correct function parameters and obtain the UE resolution value. The `METsigAlg` configuration flags related to unclustered energy are described in Tab. 3.9.

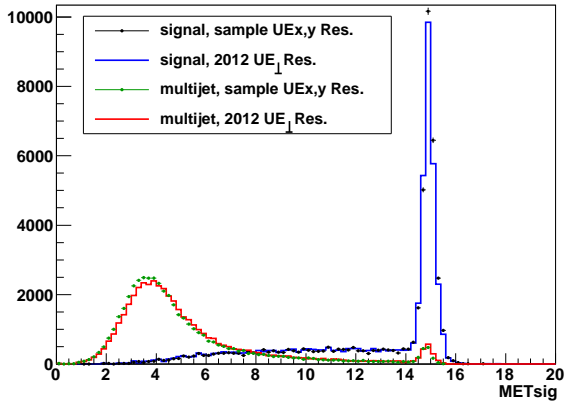


MET Significance: Minimum Probability  $1 \times 10^{-4}$ 

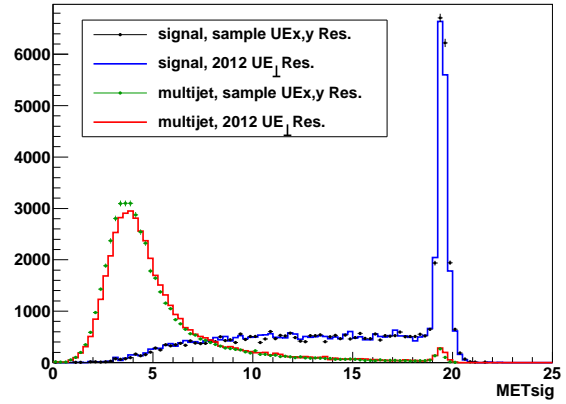
$$(a) p(\cancel{E}_T = 0) \geq 1 \times 10^{-4}$$

MET Significance: Minimum Probability  $1 \times 10^{-6}$ 

$$(b) p(\cancel{E}_T = 0) \geq 1 \times 10^{-6}$$

MET Significance: Minimum Probability  $1 \times 10^{-8}$ 

$$(c) p(\cancel{E}_T = 0) \geq 1 \times 10^{-8}$$

MET Significance: Minimum Probability  $1 \times 10^{-10}$ 

$$(d) p(\cancel{E}_T = 0) \geq 1 \times 10^{-10}$$

Figure 3.11 :  $\cancel{E}_T$  Significance comparison in a multijet and signal selection with four lower probability limits.

Flag Name	Description	Default	Allowed Values
<code>UseOldUERes</code>	Turn on 2006 UE resolution	false	true/false
<code>Use07UERes</code>	Turn on 2007 UE resolution	false	true/false
<code>UseUESmearing</code>	Turn on RunIIb MC SUE smearing	false	true/false
<code>metLMinProbability</code>	Adjust minimum probability	$1 \times 10^{-08}$	$[1 \times 10^{-37}, 1]$

Table 3.9 : `METsigAlg` processor configuration options

In the most recent version of `METsigAlg` the default UE resolution is the 2012 derivation and the minimum probability is set to  $1 \times 10^{-8}$ . Also updated is the default value for `UseUESmearing`. Since 2009 the value of SUE was smeared in the UE resolution calculation for RunIIb Monte Carlo events. This smearing has now been shown to severely degrade agreement between data and Monte Carlo in the SUE distribution [18], so the default has been changed to “false” to turn off the smearing. The default settings of the `METsigAlg` processor now use a reliable model of the unclustered energy resolution with a minimum probability designed to regain familiar separation power against multijet events.

## Chapter 4

### Missing Momentum from Tracks

`TrackMPT` is a new processor in the  $D\bar{O}$  analysis framework which calculates missing transverse momentum from tracks and other related quantities. These variables show promise for helping analysts separate out background events from signal events expected to have large amounts of real missing energy. Many background events can pass high  $\cancel{E}_T$  requirements and tools to compare  $\cancel{E}_T$  with both the magnitude and direction of missing momentum from the particle tracks can help reduce these backgrounds further.

#### 4.1 Missing $p_T$ and $Dphi$

Missing transverse momentum from tracks ( $\cancel{p}_T$ ) is the negative vector sum of track momenta transverse to the beamline. Its magnitude is expressed as  $\cancel{p}_T$ . In the  $D\bar{O}$  framework tracks are stored using a `TMBTrack` object. Two accessible parameters are azimuthal angle  $\phi$  and charge/momentum ( $q/p_T$ ), called  $c$  for curvature. These variables are used to calculate  $p_{x,y}$  for each track associated with the primary vertex.

$$p_{Tx} = p_T \cos \phi = \frac{\cos \phi}{|c|} \quad (4.1)$$

$$p_{Ty} = p_T \sin \phi = \frac{\sin \phi}{|c|} \quad (4.2)$$

Track momenta are summed such that:

$$\cancel{p}_{Tx} = - \sum_{\text{tracks}} p_{Tx} \quad (4.3)$$

$$\cancel{p}_{Ty} = - \sum_{\text{tracks}} p_{Ty} \quad (4.4)$$

And therefore:

$$\cancel{p}_T = \sqrt{\cancel{p}_{Tx}^2 + \cancel{p}_{Ty}^2} \quad (4.5)$$

$$\phi_{\cancel{p}_T} = \tan^{-1} \left( \frac{\cancel{p}_{Ty}}{\cancel{p}_{Tx}} \right) \quad (4.6)$$

The angle between  $\cancel{\mathbf{p}}_T$  from tracks and calorimeter missing transverse energy ( $\cancel{\mathbf{E}}_T$ ) is labeled *Dphi*.

$$Dphi \equiv |\phi_{\cancel{\mathbf{E}}_T} - \phi_{\cancel{p}_T}|, \quad 0 \leq Dphi \leq \pi \quad (4.7)$$

## 4.2 Significance Variables

To construct a significance measure for  $\cancel{p}_T$ , similar to  $\cancel{E}_T$  significance, the variance on the magnitude of  $\cancel{p}_T$  must be calculated. An error matrix is available for the track parameters  $c$  and  $\phi$ , and from this initial matrix a series of propagations yields the necessary  $\cancel{p}_T$  variance.

In the following derivation covariance matrices will be denoted with one index, i.e.  $\sigma_a^2$ , and their elements (the variances or covariances of specific quantities) will be denoted with two indices, i.e.  $\sigma_{cc}^2$ .

### 4.2.1 $p_x p_y$ Covariance Matrix

The covariance matrix of track parameters, labeled  $\sigma_{\text{track}}^2$ , is used to compute a covariance matrix in the  $p_x p_y$  coordinate system, labeled  $\sigma_p^2$ . The formula for propagating an error

matrix from one coordinate system to another is [19]:

$$(\sigma_x^2)_{ij} = \sum_{kl} \frac{\partial x_i}{\partial a_k} \frac{\partial x_j}{\partial a_l} (\sigma_a^2)_{kl} \quad (4.8)$$

To calculate  $\sigma_p^2$  from  $\sigma_{\text{track}}^2$  for one track, let:

$$a_1 = |c| \quad x_1 = p_x = \frac{\cos \phi}{|c|} \quad \frac{\partial p_x}{\partial c} = -\frac{\cos \phi}{c^2} \quad \frac{\partial p_x}{\partial \phi} = -\frac{\sin \phi}{|c|} \quad (4.9)$$

$$a_2 = \phi \quad x_2 = p_y = \frac{\sin \phi}{|c|} \quad \frac{\partial p_y}{\partial c} = -\frac{\sin \phi}{c^2} \quad \frac{\partial p_y}{\partial \phi} = \frac{\cos \phi}{|c|} \quad (4.10)$$

$$\sigma_{\text{track}}^2 = \begin{bmatrix} \sigma_{cc}^2 & \text{cov}_{c\phi} \\ \text{cov}_{c\phi} & \sigma_{\phi\phi}^2 \end{bmatrix} \quad (4.11)$$

By applying Eqs. 4.9 - 4.11 to Eq. 4.8:

$$\sigma_{p_x p_x}^2 = \left( \frac{\partial p_x}{\partial c} \right)^2 \sigma_{cc}^2 + 2 \frac{\partial p_x}{\partial c} \frac{\partial p_x}{\partial \phi} \text{cov}_{c\phi} + \left( \frac{\partial p_x}{\partial \phi} \right)^2 \sigma_{\phi\phi}^2 \quad (4.12)$$

$$= \frac{\cos^2 \phi}{c^4} \sigma_{cc}^2 + 2 \frac{\cos \phi \sin \phi}{|c|^3} \text{cov}_{c\phi} + \frac{\sin^2 \phi}{c^2} \sigma_{\phi\phi}^2 \quad (4.13)$$

$$\text{cov}_{p_x p_y} = \frac{\partial p_x}{\partial c} \frac{\partial p_y}{\partial c} \sigma_{cc}^2 + \left( \frac{\partial p_x}{\partial c} \frac{\partial p_y}{\partial \phi} + \frac{\partial p_y}{\partial c} \frac{\partial p_x}{\partial \phi} \right) \text{cov}_{c\phi} + \frac{\partial p_x}{\partial \phi} \frac{\partial p_y}{\partial \phi} \sigma_{\phi\phi}^2 \quad (4.14)$$

$$= \frac{\cos(\phi) \sin(\phi)}{c^4} \sigma_{cc}^2 + \frac{\sin^2(\phi) - \cos^2(\phi)}{|c|^3} \text{cov}_{c\phi} + \frac{-\sin(\phi) \cos(\phi)}{c^2} \sigma_{\phi\phi}^2 \quad (4.15)$$

$$\sigma_{p_y p_y}^2 = \left( \frac{\partial p_y}{\partial c} \right)^2 \sigma_{cc}^2 + 2 \frac{\partial p_y}{\partial c} \frac{\partial p_y}{\partial \phi} \text{cov}_{c\phi} + \left( \frac{\partial p_y}{\partial \phi} \right)^2 \sigma_{\phi\phi}^2 \quad (4.16)$$

$$= \frac{\sin^2 \phi}{c^4} \sigma_{cc}^2 - 2 \frac{\cos \phi \sin \phi}{|c|^3} \text{cov}_{c\phi} + \frac{\cos^2 \phi}{c^2} \sigma_{\phi\phi}^2 \quad (4.17)$$

$$(\sigma_p^2)_{\text{track}} = \begin{bmatrix} \sigma_{p_x p_x}^2 & \text{COV}_{p_x p_y} \\ \text{COV}_{p_x p_y} & \sigma_{p_y p_y}^2 \end{bmatrix} \quad (4.18)$$

### 4.2.2 $\not{p}_T$ Covariance Matrix

Measurements of individual tracks within an event are not correlated to each other, so the tracks'  $p_x p_y$  error matrices are summed in quadrature, following Eqs. 4.3 - 4.4:

$$(\sigma_p^2)_{\not{p}_T} = \sum_{\text{tracks}} (-1)^2 (\sigma_p^2)_{\text{track}} \quad (4.19)$$

Another propagation yields the covariance matrix for the  $\not{p}_T$ - $\phi_{\not{p}_T}$  magnitude-direction coordinate system, labeled  $\sigma_{\not{p}_T}^2$ .

$$\text{For brevity, let: } X \equiv \not{p}_{Tx}, \quad Y \equiv \not{p}_{Ty}, \quad P \equiv \not{p}_T, \quad \phi \equiv \phi_{\not{p}_T} \quad (4.20)$$

$$a_1 = X \quad x_1 = P = \sqrt{X^2 + Y^2} \quad \frac{\partial P}{\partial X} = \frac{X}{P} \quad \frac{\partial P}{\partial Y} = \frac{Y}{P} \quad (4.21)$$

$$a_2 = Y \quad x_2 = \phi = \tan^{-1} \left( \frac{Y}{X} \right) \quad \frac{\partial \phi}{\partial X} = -\frac{Y}{P^2} \quad \frac{\partial \phi}{\partial Y} = \frac{X}{P^2} \quad (4.22)$$

$$\sigma_a^2 = (\sigma_p^2)_{\not{p}_T} = \begin{bmatrix} \sigma_{XX}^2 & \text{COV}_{XY} \\ \text{COV}_{XY} & \sigma_{YY}^2 \end{bmatrix} \quad (4.23)$$

By applying Eqs. 4.21 - 4.23 to Eq. 4.8:

$$\sigma_{PP}^2 = \left( \frac{\partial P}{\partial X} \right)^2 \sigma_{XX}^2 + 2 \frac{\partial P}{\partial X} \frac{\partial P}{\partial Y} \text{COV}_{XY} + \left( \frac{\partial P}{\partial Y} \right)^2 \sigma_{YY}^2 \quad (4.24)$$

$$= \frac{1}{P^2} (X^2 \sigma_X^2 + 2XY \text{COV}_{XY} + Y^2 \sigma_Y^2) \quad (4.25)$$

$$\text{cov}_{P\phi} = \frac{\partial P}{\partial X} \frac{\partial \phi}{\partial X} \sigma_{XX}^2 + \left( \frac{\partial P}{\partial X} \frac{\partial \phi}{\partial Y} + \frac{\partial \phi}{\partial X} \frac{\partial P}{\partial Y} \right) \text{cov}_{XY} + \frac{\partial P}{\partial Y} \frac{\partial \phi}{\partial Y} \sigma_{YY}^2 \quad (4.26)$$

$$= \frac{1}{P^3} (-XY \sigma_{XX}^2 + (X^2 - Y^2) \text{cov}_{XY} + XY \sigma_{YY}^2) \quad (4.27)$$

$$\sigma_{\phi\phi}^2 = \left( \frac{\partial \phi}{\partial X} \right)^2 \sigma_{XX}^2 + 2 \frac{\partial \phi}{\partial X} \frac{\partial \phi}{\partial Y} \text{cov}_{XY} + \left( \frac{\partial \phi}{\partial Y} \right)^2 \sigma_{YY}^2 \quad (4.28)$$

$$= \frac{1}{P^4} (Y^2 \sigma_{XX}^2 - 2XY \text{cov}_{XY} + X^2 \sigma_{YY}^2) \quad (4.29)$$

$$\sigma_{\not{p}_T}^2 = \begin{bmatrix} \sigma_{PP}^2 & \text{cov}_{P\phi} \\ \text{cov}_{P\phi} & \sigma_{\phi\phi}^2 \end{bmatrix} \quad (4.30)$$

### 4.2.3 $p_T$ Significance

$\not{p}_T$  significance (MPTsig) is computed in the same manner as  $\cancel{E}_T$  significance (METsig) [12].

Knowing the  $\not{p}_T$  magnitude variance from Eq. 4.25, a probability distribution  $p(\text{MPT})$  can be written for  $\not{p}_T$ . Probabilities are then evaluated for two hypotheses:  $\not{p}_T$  equal to its measured value, and  $\not{p}_T$  equal to zero. MPTsig is a measure of the difference in probability between these two hypotheses. Low significance values indicate that the  $\not{p}_T$  in an event can be reasonably explained by fluctuations in the track momenta, while large significance values indicate genuine  $\not{p}_T$ . MPTsig is computed as follows, where  $\mathcal{N}$  represents a normalized Gaussian distribution:

$$p(\text{MPT}) = \mathcal{N} \left( \not{p}_T, \sqrt{\sigma_{PP}^2} \right) \quad (4.31)$$

$$\text{MPTsig} \equiv \log \frac{p(\text{MPT} = \not{p}_{T,\text{meas}})}{p(\text{MPT} = 0)} \quad (4.32)$$

The range of the MPTsig distribution is set by the minimum probability in Eq. 4.32, as was done for METsig in section 3.2. `TrackMPT` is constructed using double precision, so the

probability limit can be pushed close to the minimum double. The relevant equation is:

$$1 \times 10^{308} = \frac{p(\text{MPT} = \not{p}_{T,\text{meas}})}{\text{ProbabilityLimit}} \quad (4.33)$$

A substantial “buffer” of  $1 \times 10^8$  is chosen for the numerator, which gives a probability limit of  $1 \times 10^{-300}$ . This value was chosen to provide good separation between  $W$  boson and  $Z$  boson events.

#### 4.2.4 “MM” Significance

A variable called “MMsig” is a significance measure for the difference of  $\not{p}_{\mathbf{T}}$  and  $\not{E}_{\mathbf{T}}$ . The difference vector is  $\text{MM} = \alpha \not{p}_{\mathbf{T}} - \not{E}_{\mathbf{T}}$ , where  $\alpha$  allows comparison of  $\not{p}_{\mathbf{T}}$  with some fraction of  $\not{E}_{\mathbf{T}}$ . The  $p_x p_y$  covariance matrices for  $\not{p}_T$  and  $\not{E}_T$  are summed to produce a covariance matrix for  $MM$ .

$$(\sigma_p^2)_{MM} = \alpha^2 (\sigma_p^2)_{\not{p}_T} + (\sigma_p^2)_{\not{E}_T} \quad (4.34)$$

The matrix  $(\sigma_p^2)_{\not{p}_T}$  is known from Eq. 4.19, and the  $p_x p_y$  covariance matrix for  $\not{E}_T$  is constructed by summing matrices for each calorimeter object. These matrices are calculated using the method in Eqs. 4.8 - 4.18, with the following input for each calorimeter object:

$$a_1 = E_T \quad E_x = E_T \cos \phi \quad \frac{\partial E_x}{\partial E_T} = \cos \phi \quad \frac{\partial E_x}{\partial \phi} = -E_T \sin \phi \quad (4.35)$$

$$a_2 = \phi \quad E_{Ty} = E_T \sin \phi \quad \frac{\partial E_y}{\partial E_T} = \sin \phi \quad \frac{\partial E_y}{\partial \phi} = E_T \cos \phi \quad (4.36)$$

$$\sigma_a^2 = \begin{bmatrix} \sigma_{E_T E_T}^2 & 0 \\ 0 & 0 \end{bmatrix} \quad (4.37)$$



In Eq. 4.37 the energy variances of the individual objects are known, and for the unknown elements a value of zero is assumed. Direction is generally well-measured at  $D\emptyset$ , and from a study of the covariance matrix for track parameters it is clear that variance on energy or momentum is much larger than matrix elements involving angle. Application of Eq. 4.8 gives:

$$(\sigma_p^2)_{\text{object}} = \begin{bmatrix} \sigma_{E_x E_x}^2 & \text{COV}_{E_x E_y} \\ \text{COV}_{E_x E_y} & \sigma_{E_y E_y}^2 \end{bmatrix} = \begin{bmatrix} \sigma_{E_T E_T}^2 \cos^2 \phi & \sigma_{E_T E_T}^2 \cos \phi \sin \phi \\ \sigma_{E_T E_T}^2 \cos \phi \sin \phi & \sigma_{E_T E_T}^2 \sin^2 \phi \end{bmatrix} \quad (4.38)$$

$$(\sigma_p^2)_{\cancel{E}_T} = \sum_{\text{objects}} (\sigma_p^2)_{\text{object}} \quad (4.39)$$

From  $(\sigma_p^2)_{MM}$ , an analog of Eq. 4.25 gives  $\sigma_{MM}^2$ , the variance of the magnitude of  $\mathbf{MM}$ , and  $\text{MMsig}$  can be calculated.  $\text{MMsig}$  is a measure of how the probability of  $MM = MM_{\text{measured}}$  differs from the probability of  $MM = 0$ .

$$p(\text{MM}) = \mathcal{N}\left(MM, \sqrt{\sigma_{MM}^2}\right) \quad (4.40)$$

$$\text{MMsig} \equiv \log \frac{p(\text{MM} = MM_{\text{meas}})}{p(\text{MM} = 0)} \quad (4.41)$$

Events in which  $\cancel{p}_T$  and  $\cancel{E}_T$  differ only slightly, considering their variances,  $\text{MMsig}$  will have a low value. Events with high  $\text{MMsig}$  indicate that  $\cancel{p}_T$  and  $\cancel{E}_T$  are clearly distinct from one another.

### 4.3 TrackMPT Processor

`TrackMPT` has been implemented in the  $D\emptyset$  framework as a processor which works alongside `ReComputeMET` and `METsigAlg`. The processor runs over the collection of tracks, filtering

them through quality and impact parameter requirements so that only good tracks associated with the primary vertex are used to calculate  $\mathbf{p}_T$ . A track's impact parameter is the closest distance between a point on the track and the primary vertex. Examples of impact parameters in the  $\hat{z}$  and  $\hat{r}$  directions are shown in Fig. 4.1. Track quality values are determined by a processor called `FakeTrackKiller`, which was designed to identify poorly reconstructed tracks, such as those originating from the unphysical vertices studied in section 2.2. `TrackMPT` output variables are listed in Tab. 4.1 and configuration options are listed in Tab. 4.2.

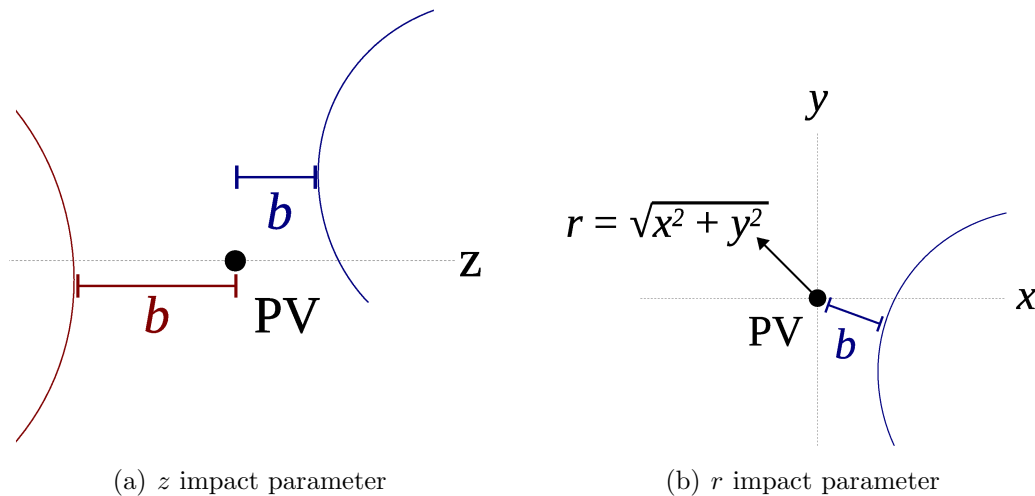


Figure 4.1 : A track's impact parameter, labeled  $b$ , marks the closest distance between the track and the primary vertex. `TrackMPT` calculates impact parameter along the  $z$  axis (a), and along the radial direction  $r$  in the  $xy$  plane (b).

#### 4.4 Performance in $Z \rightarrow ee$ events

`TrackMPT` variables have been studied in  $Z \rightarrow ee$  events for data/Monte Carlo consistency.

Name	Description
trackMPT	Magnitude of $\cancel{p}_T$
trackMPTphi	Direction of $\cancel{p}_T$
trackMPTDphi	Angle between $\cancel{E}_T$ and $\cancel{p}_T$
trackMPTsigmaMPT	Uncertainty on $\cancel{p}_T$
trackMPTsigmaDphi	Uncertainty on $Dphi$
trackMPTsignificance	$\cancel{p}_T$ significance
trackMPTMMsignificance	MM significance

Table 4.1 : TrackMPT processor output variables

Data and Monte Carlo events in the Run2b3 samples listed in Tables 3.1 and 3.2 were used for this study. Figure 4.2 shows distributions for  $\cancel{E}_T$  and  $\cancel{p}_T$ . Values of  $\cancel{p}_T$  below 10 GeV are modeled poorly compared to the rest of the distribution. Figure 4.3 shows distributions for  $\phi_{\cancel{p}_T}$  and  $\phi_{\cancel{E}_T}$ . The asymmetric mis-modeling in  $\phi_{\cancel{E}_T}$  produces asymmetric mis-modeling in  $Dphi$  values above  $\pi/2$  if it is calculated without taking an absolute value, though the area of common interest ( $Dphi \leq \pi/2$ ) shows good agreement (Fig. 4.4(a)). Taking the absolute value cancels out this effect, producing a well-modeled  $Dphi$  distribution (Fig. 4.4(b)). MPTsig and MMsig distributions are shown in Fig. 4.5. The uncertainty on  $\cancel{p}_T$  is generally underestimated by the Monte Carlo (Fig. 4.6), which leads to a slight overestimation of MPTsig, since narrower distributions in Eq. 4.31 produce larger significance values for constant  $\cancel{p}_T$ . These  $Z \rightarrow ee$  events show a tail to high  $\cancel{p}_T$  corresponding to events

Name	Description	Default	Allowed Range
FTKQuality	FakeTrackKiller minimum quality	0	(-1, 1)
PVdZ_CFTonly	Max Z impact par, CFT only tracks	2.0 cm	(0,∞)
PVdZ_hasSMT	Max Z impact par, tracks with SMT	1.0 cm	(0,∞)
PVdR_CFTonly	Max Radial ip, CFT only tracks	1.0 cm	(0,∞)
PVdR_hasSMT	Max Radial ip, tracks with SMT	0.5 cm	(0,∞)
MCscale_ccVar	c-c matrix element multiplier	1	(-∞,∞)
MCscale_cphiCov	c- $\phi$ matrix element multiplier	1	(-∞,∞)
MCscale_phiphiVar	$\phi$ - $\phi$ matrix element multiplier	1	(-∞,∞)
MMcoeffForMPT	$\alpha$ coefficient in <b>MM</b>	1	(-∞,∞)

Table 4.2 : TrackMPT processor configuration options

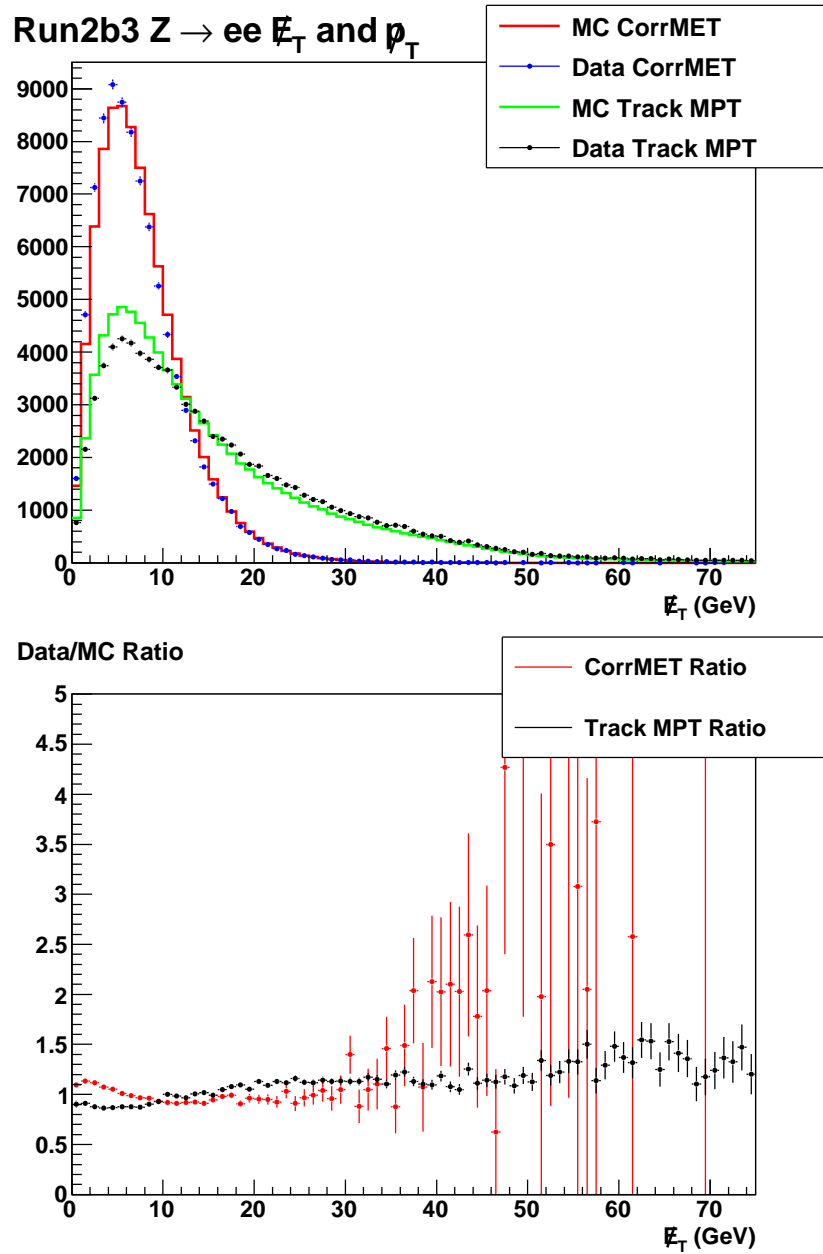
with very large track momentum uncertainties. The tails can be reduced by discarding events with  $\text{MPTsig}$  very close to zero (Fig. 4.7).

## 4.5 Multi-sample Comparisons

The anticipated usage of `TrackMPT` is in cases where  $\cancel{p}_T$  has contributions from neutral particles, as well as energy mis-measurement, dead cells, etc. Figures 4.8 and 4.9 show distributions of  $\cancel{p}_T$ ,  $Dphi$ ,  $\text{MPTsig}$ , and  $\text{MMsig}$  for the  $Z \rightarrow ee$  MC,  $W \rightarrow e\nu$  MC, and QCD Data samples listed in Tab. 4.3.  $W \rightarrow e\nu$  and QCD samples contain events with:

- 1 Point 0 (QCD) or Point1 ( $W \rightarrow e\nu$ ) electron
- electron  $p_T > 10$  GeV
- minimum 20 GeV of corrected  $\cancel{E}_T$
- primary vertex radial position  $< 1.0$  cm

Both the  $\cancel{p}_T$  and  $Dphi$  distributions show a clear distinction between the  $W$  boson events, with expected missing momentum from neutrinos, and events in which  $\cancel{p}_T$  is only expected from detector effects or an asymmetric distribution of neutral jet particles.  $\text{MPTsig}$  shows good separation between  $W$  and  $Z$  peaks, similar to that relied upon in  $\text{METsig}$ .  $\text{MMsig}$  is not as powerful a discriminant for these selections.



(a) All events

Figure 4.2 : Distributions of  $\cancel{E}_T$  and  $\cancel{p}_T$  in RunIIb3  $Z \rightarrow ee$  events.

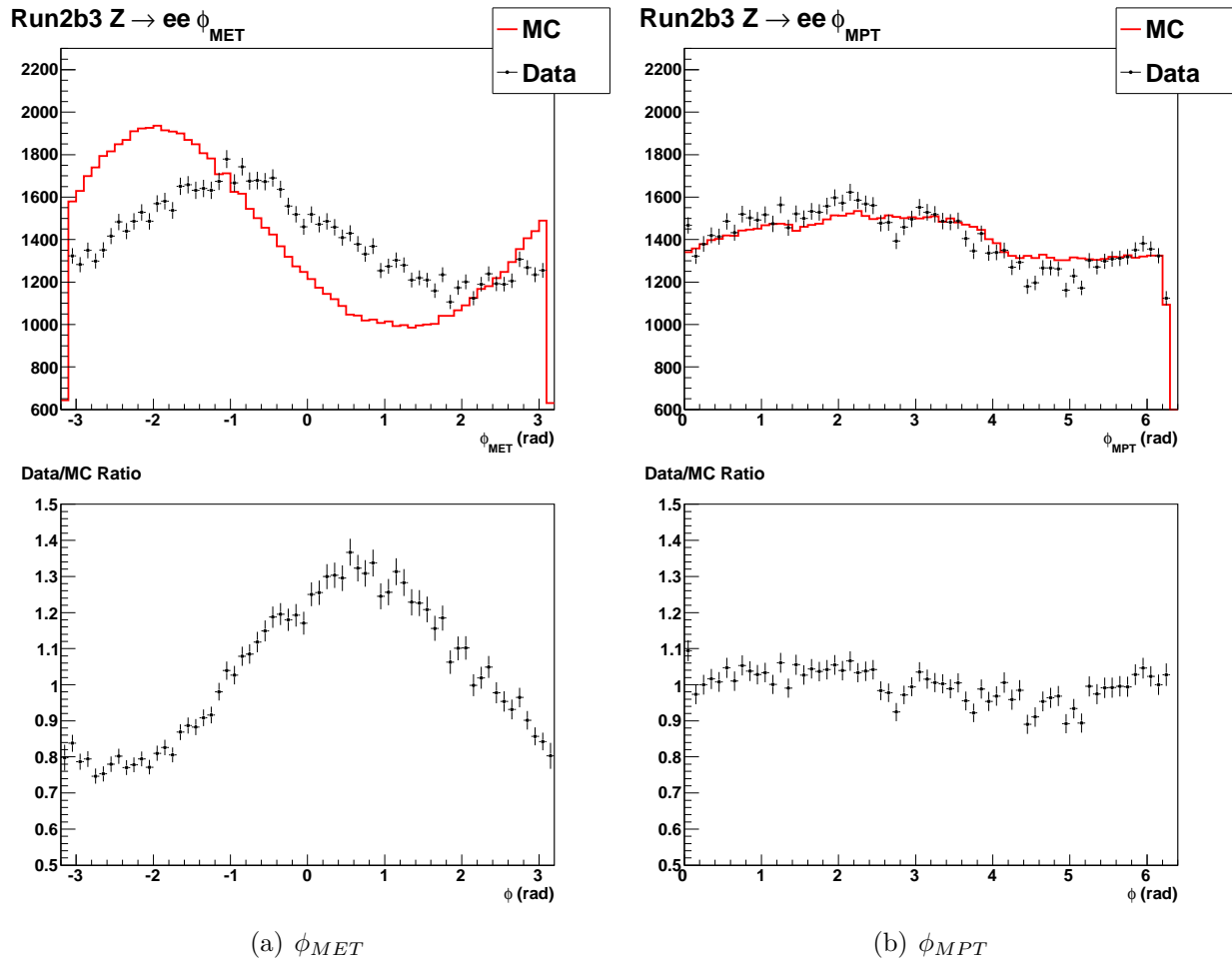


Figure 4.3 : Distributions of  $\phi_{E_T}$  and  $\phi_{\cancel{e}_T}$  in RunIIb3  $Z \rightarrow ee$  events.

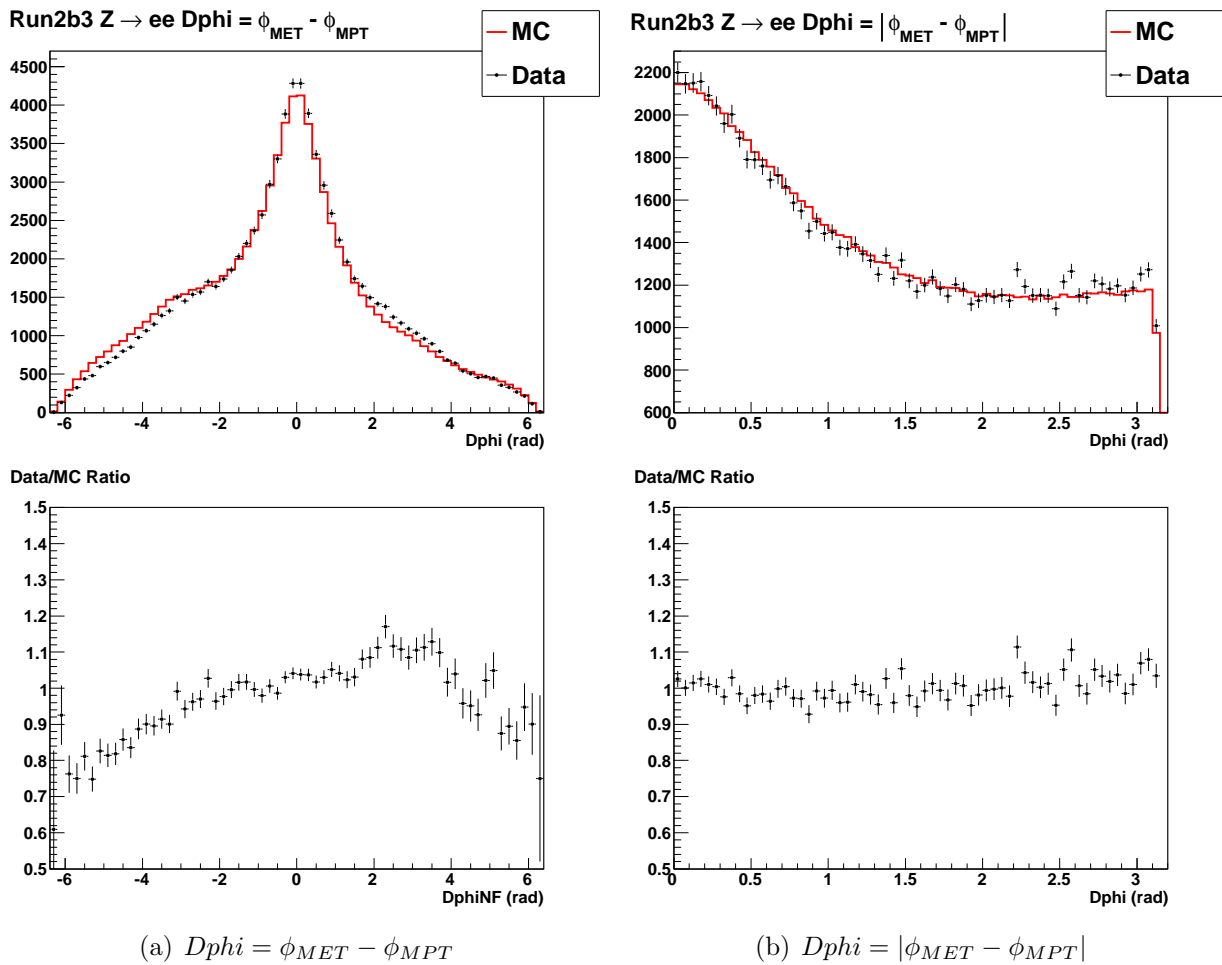


Figure 4.4 : Distributions of  $Dphi$  calculated without (a) and with (b) an absolute value in RunIIb3  $Z \rightarrow ee$  events.



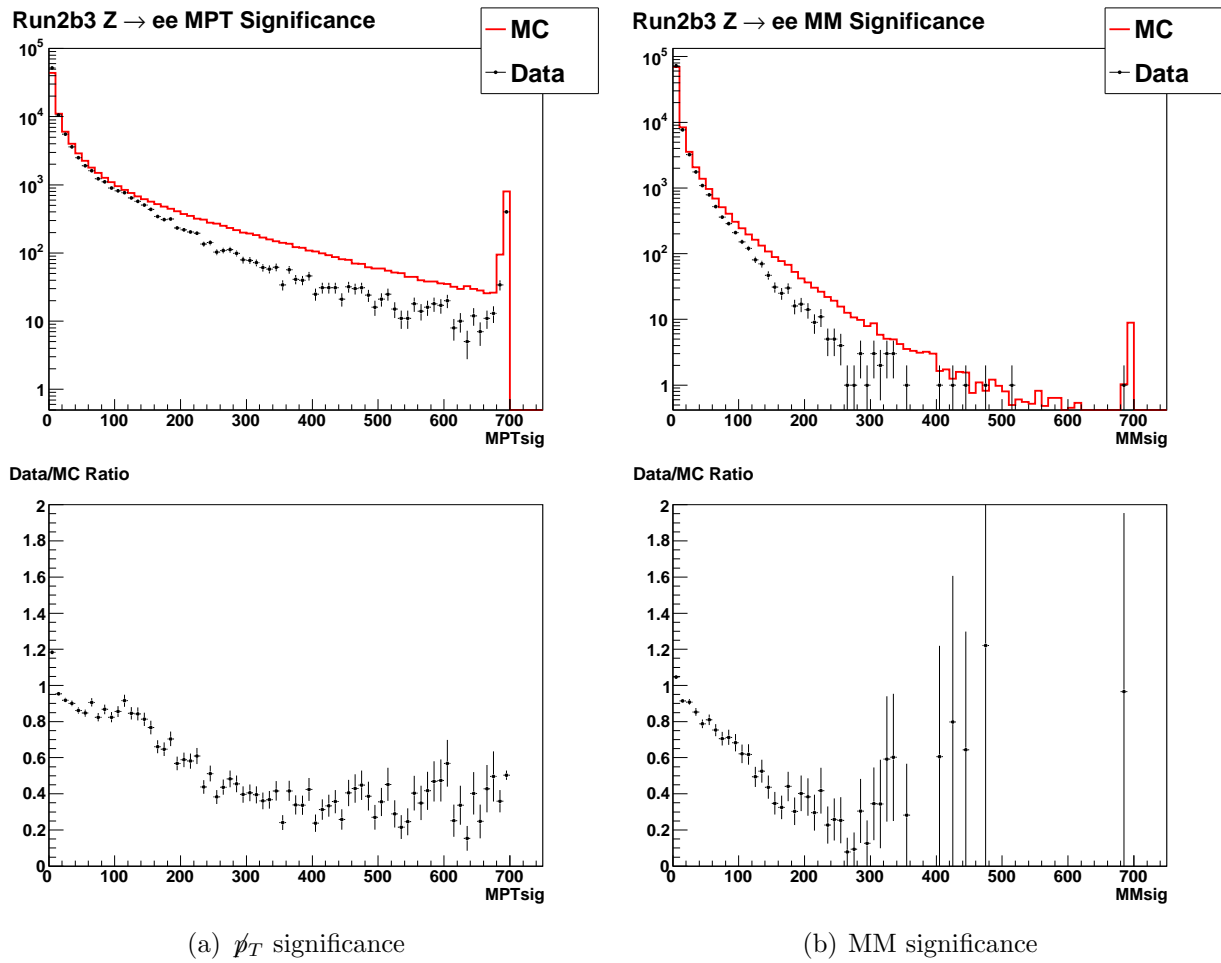


Figure 4.5 : Distributions of MPTsig and MMsig in RunIIb3  $Z \rightarrow ee$  events.

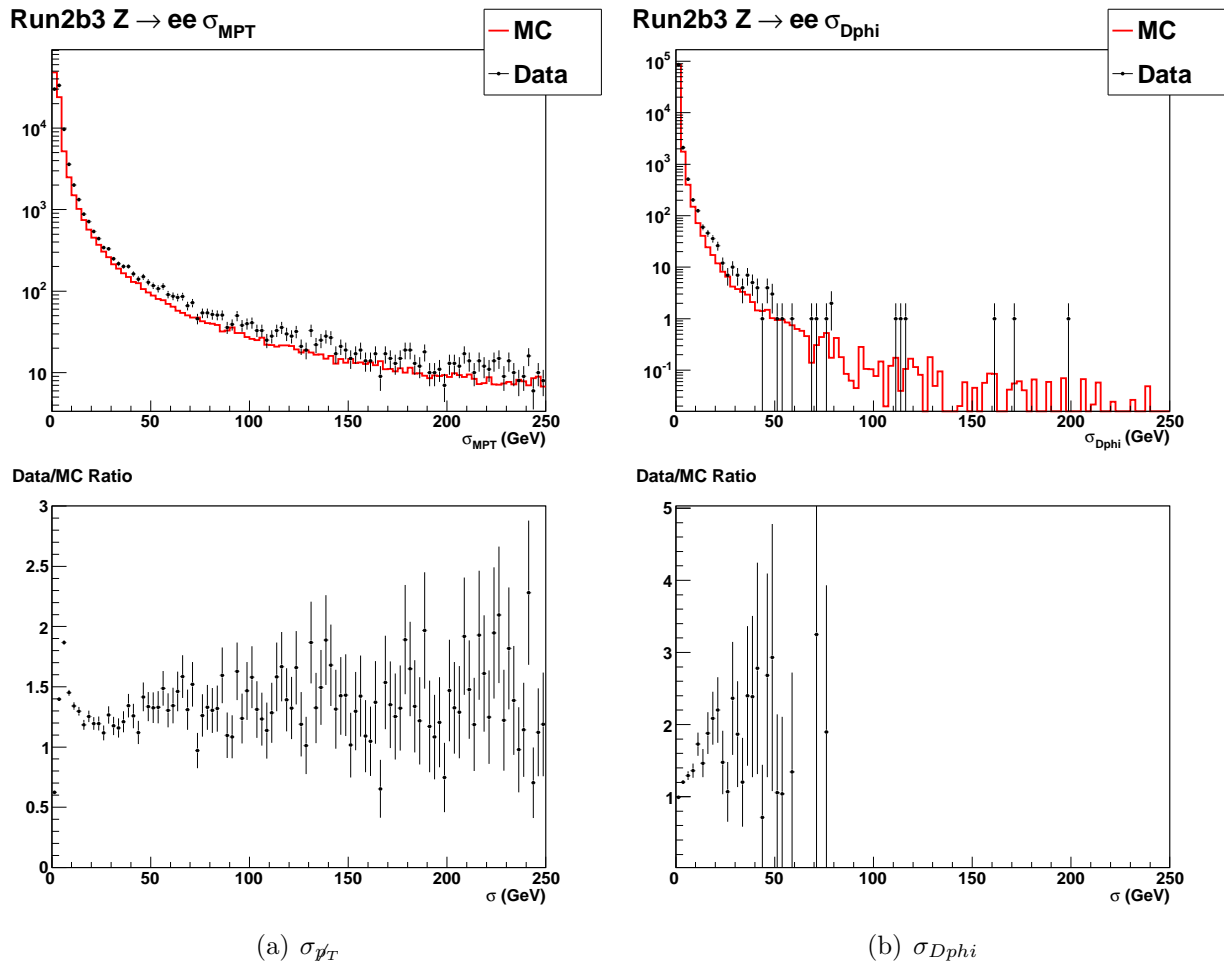


Figure 4.6 : Distributions of  $\sigma_{\psi_T}$  and  $\sigma_{Dphi}$  in RunIIb3  $Z \rightarrow ee$  events.

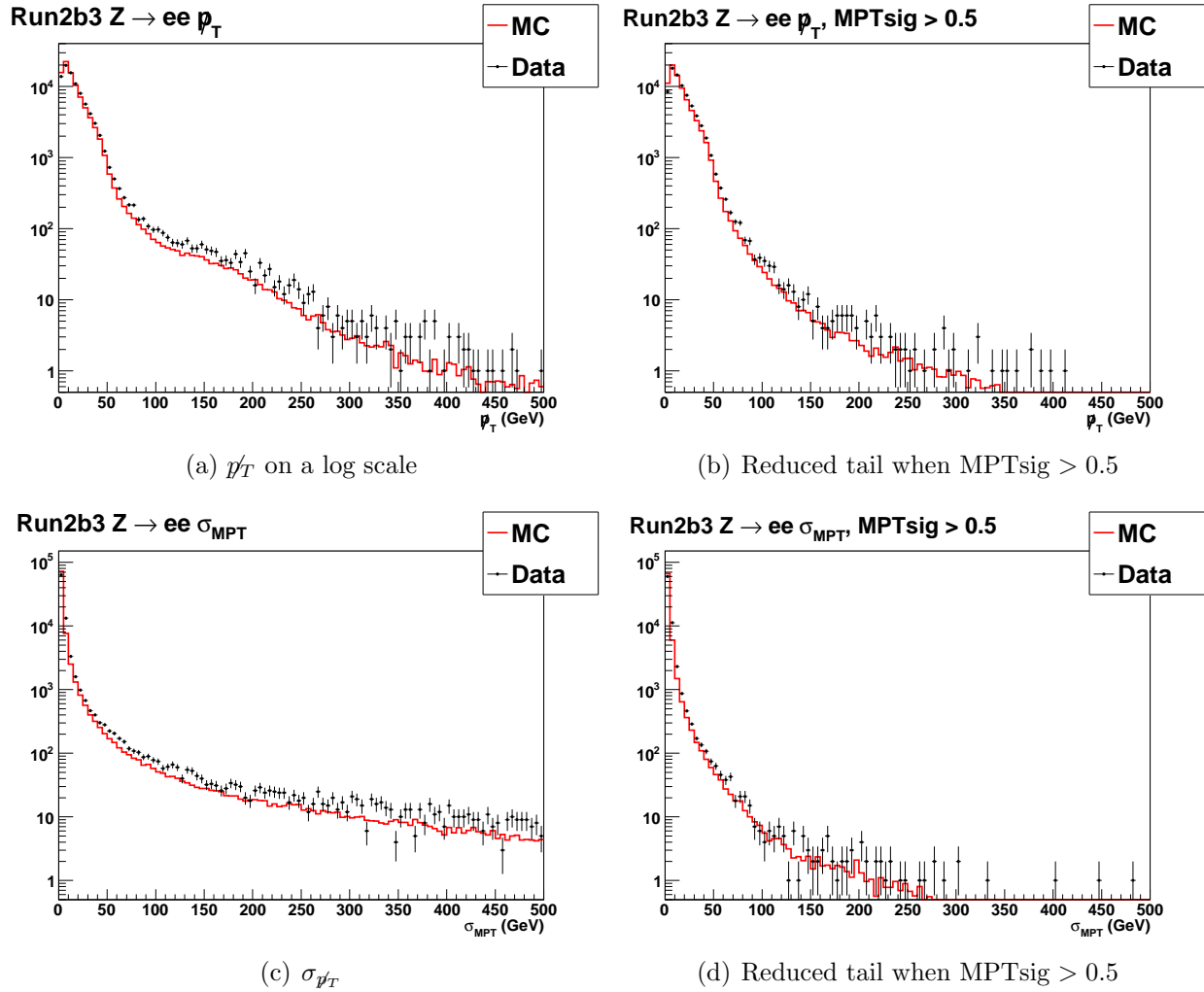


Figure 4.7 : Reduction of high  $p_T$  (a-b) and  $\sigma_{MPT}$  (c-d) tails by discarding events with  $MPTsig < 0.5$ .

Name	SAM Definition (CSG_)	N Events
DiElectron Data	CAF_2EMhighpt_PASS5_p21.18.00	88,798
$Z \rightarrow ee$ MC	alpgenpythia_gamz_ee_75_130_p212100_Run2b3_v3	2,672,718
EM Data	CAF_EMinclusive_PASS5_p21.18.00_p20.16.07_reduced2	195,952
QCD Data	CAF_QCD_PASS5_p21.18.00_p20.16.07_reduced2	11,859
$W \rightarrow e\nu$ MC	alpgenpythia_w_lnu_p212100_Run2b3_v3	1,188,714

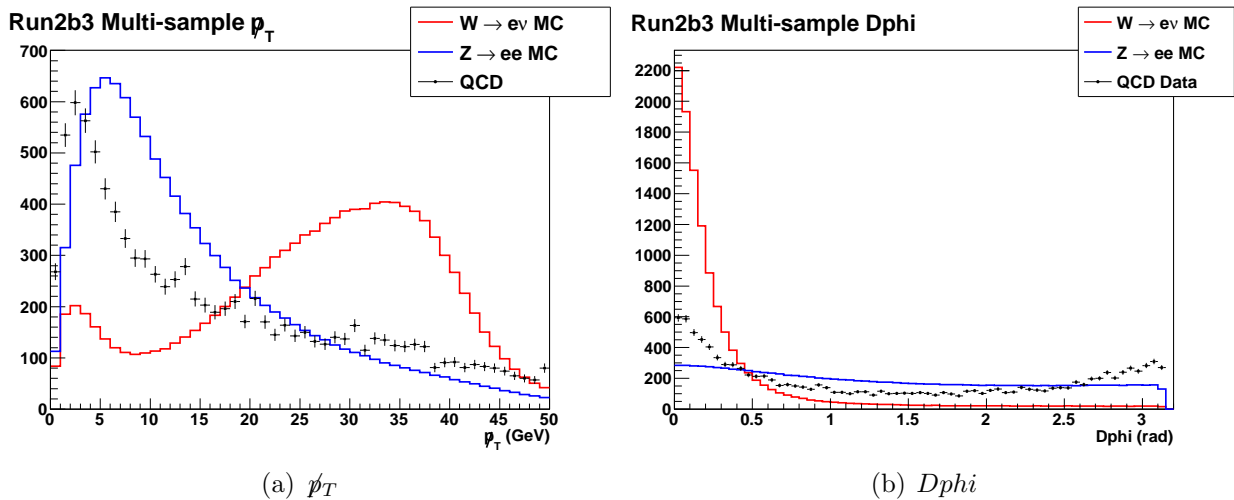
Table 4.3 : RunIIb3  $\cancel{p}_T$  test samples

Figure 4.8 : Comparisons of  $\cancel{p}_T$  and  $Dphi$  distributions in several RunIIb3 samples. From these distributions cuts are chosen at  $\cancel{p}_T = 15$  GeV and  $Dphi = \pi/4$  to separate  $W$  boson events from QCD events.

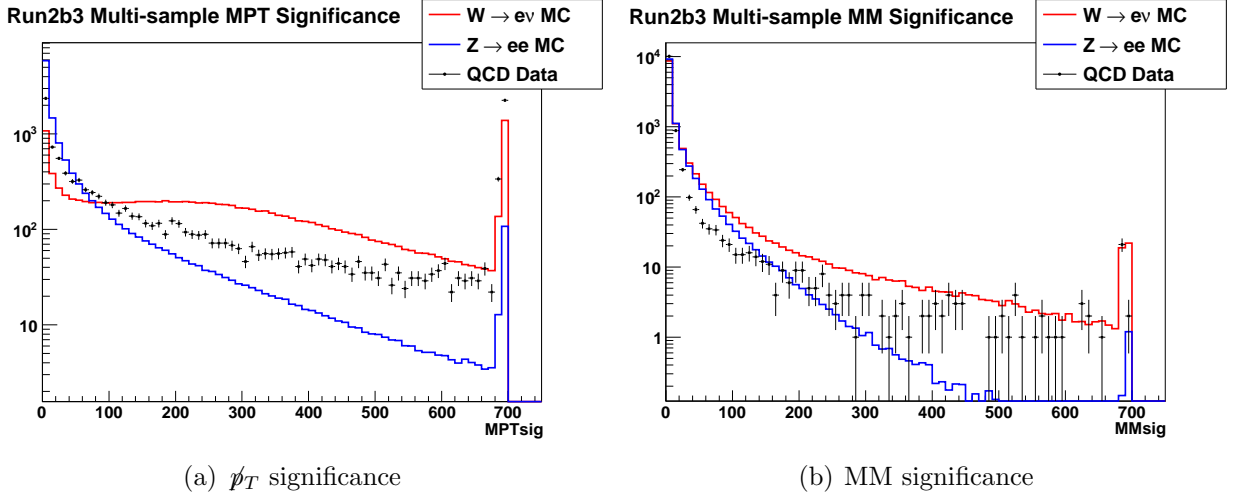


Figure 4.9 : Comparisons of MPTsig and MMsig distributions in several RunIIb3 samples.

## 4.6 $W$ Boson Sample Background Reduction

TrackMPT variables are very useful for reducing background from multijet processes. A combination of METsig,  $Dphi$ , and  $\cancel{p}_T$  cuts can significantly improve background reduction over a triangle cut, which is a common method for reducing multijet background in  $W$  boson samples. A triangle cut rejects events in the triangular area defined by the  $x$  and  $y$  axes and a line relating two quantities, traditionally  $\cancel{E}_T$  and the transverse mass of the  $W$  boson (Fig. 4.10).  $W$  transverse mass is calculated from the  $p_T$  of the electron,  $\cancel{E}_T$ , and the angle  $\theta$  between the electron and  $\cancel{E}_T$ :

$$M_T = \sqrt{2p_T^e \cancel{E}_T(1 - \cos \theta)} \quad (4.42)$$

The QCD data and  $W \rightarrow e\nu$  Monte Carlo samples from Tab. 4.3 were treated as a background/signal pair and used to test cuts for the EM Data sample, which was selected using the same criteria as the QCD data. From Fig. 4.8 cuts of  $\cancel{p}_T > 15$  GeV and  $Dphi < \pi/4$

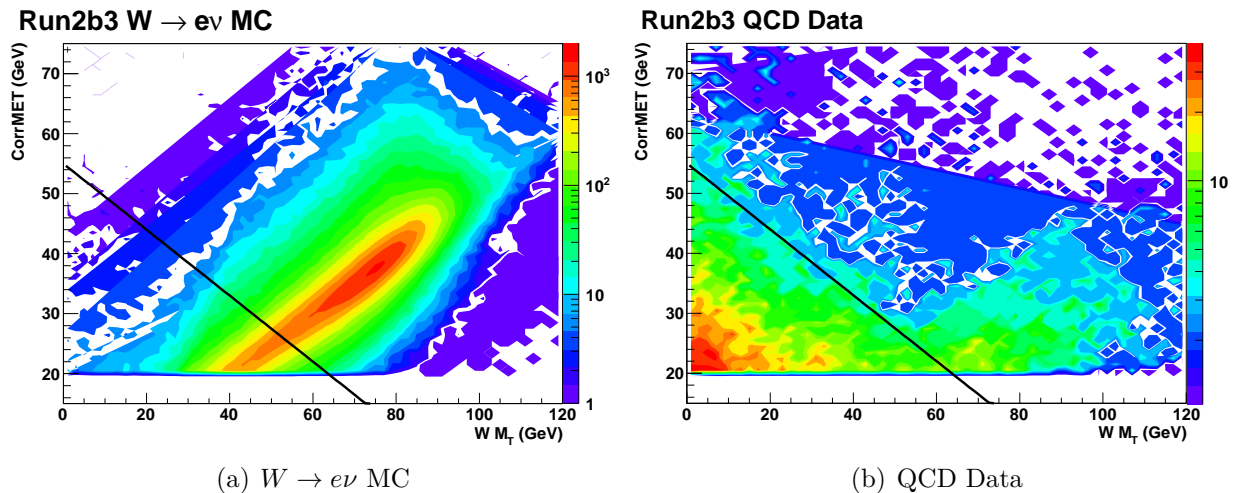


Figure 4.10 : Example of a triangle cut. Events that lie in the triangular area below the line  $\cancel{E}_T \geq 55 - \frac{11}{20}M_T$  are rejected. This cut rejects only a small percentage of  $W$  boson signal events while discarding a large percentage of QCD background events.

were chosen to reduce the multijet background in the EM Data sample and help isolate its  $W \rightarrow e\nu$  component. Figure 4.11 shows the effect of the chosen cuts on the EM Data  $M_T$  distribution, after a preliminary cut on METsig which is used frequently in high  $\cancel{E}_T$  analyses. These cuts remove a large portion of the low mass backgrounds, centering the  $M_T$  distribution near the known  $W$  boson mass of 80 GeV.

Figure 4.12 compares the effects of the chosen METsig and  $Dphi$  cuts to the effects of the following triangle cut, where  $M_T$  is the transverse mass of the  $W$  boson.

$$\cancel{E}_T \geq 55 - \frac{11}{20}M_T \quad (4.43)$$

Table 4.4 lists the efficiencies of these cuts for the  $W \rightarrow e\nu$  MC (signal), QCD Data (background), and EM Data samples. For the same signal efficiency, cuts on METsig and the TrackMPT variables remove substantially more background events; they also produce higher

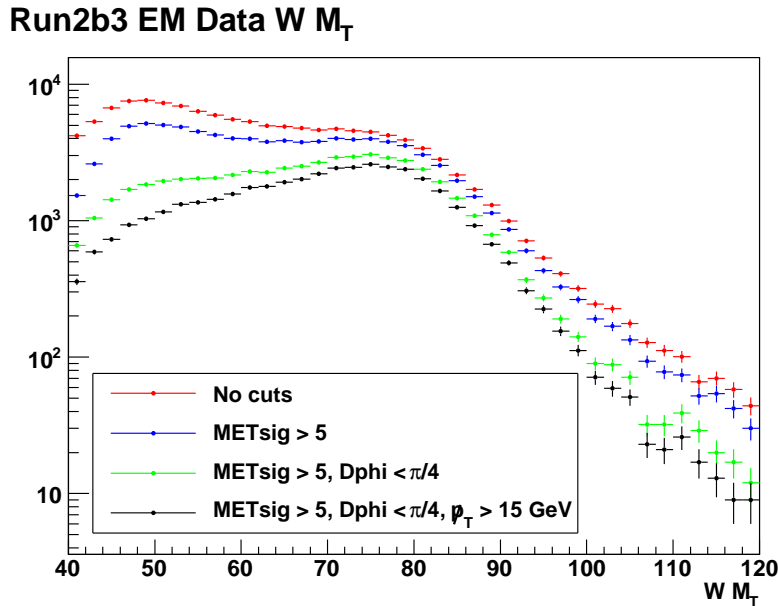


Figure 4.11 : Effect of various cuts on  $W$  boson transverse mass distribution in RunIIb3 EM Data. This study was performed prior to the METsig study detailed in Chapter 3. The METsig distributions of these samples are analogous to those in Fig. 3.7(d), hence the cut of METsig  $> 5$ .

signal to background ratios over a wide span of cut points (Fig. 4.13).

## 4.7 Summary

TrackMPT is a new processor for  $D\bar{O}$  analysts that calculates missing transverse momentum from tracks, and other useful variables such as the angle  $Dphi$  between  $\cancel{p}_T$  and  $\cancel{E}_T$ . Missing momentum variables are calculated from tracks belonging to the primary vertex, and a study of  $Z \rightarrow ee$  events shows good data/Monte Carlo agreement in the angular distributions and fair agreement in  $\cancel{p}_T$  distributions, similar to that seen for  $\cancel{E}_T$ . Distributions of  $Dphi$  and  $\cancel{p}_T$  show distinct differences in behavior between events with expected missing neutrino momentum and those where missing momentum arises from mis-measurement or other random

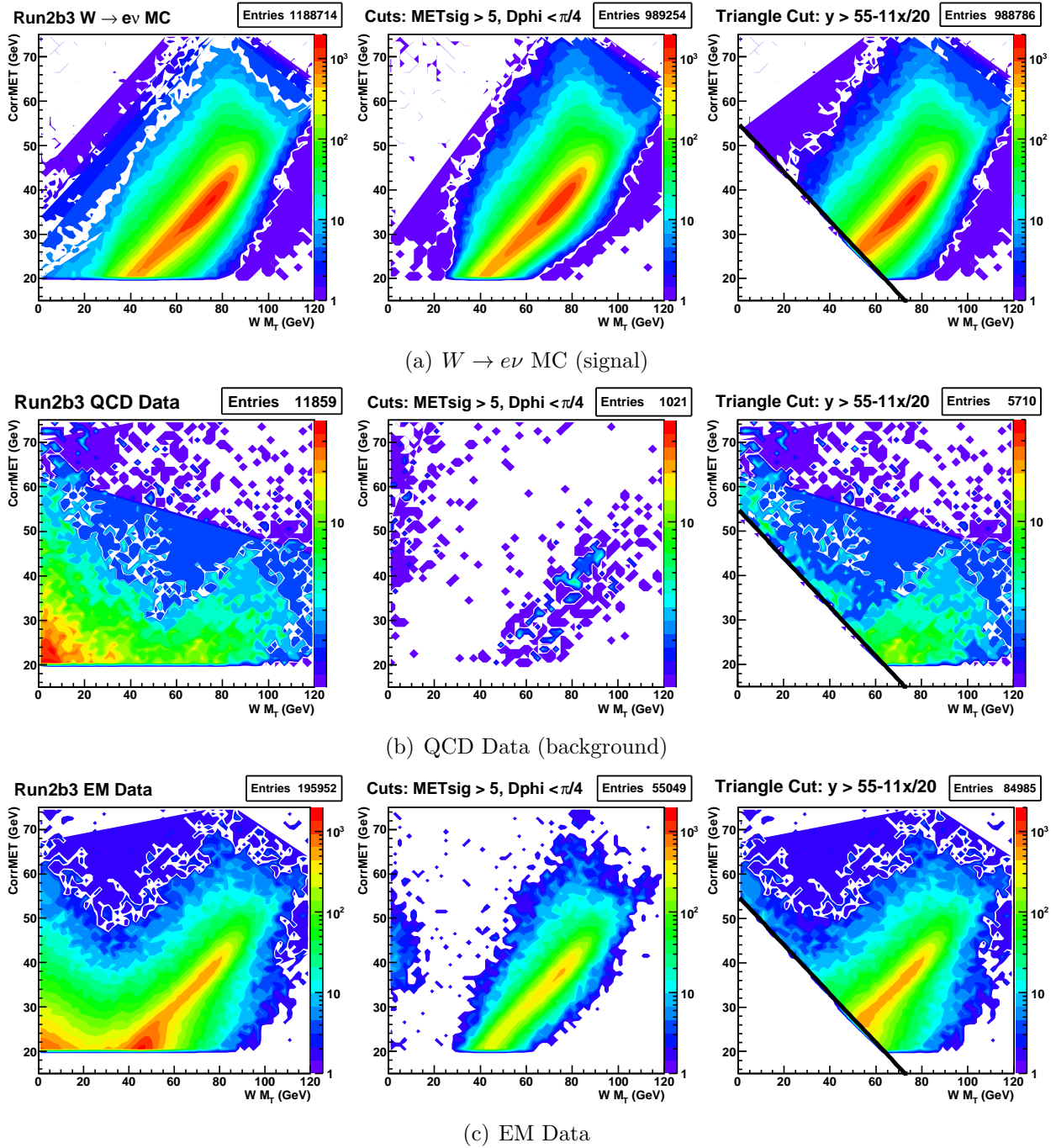
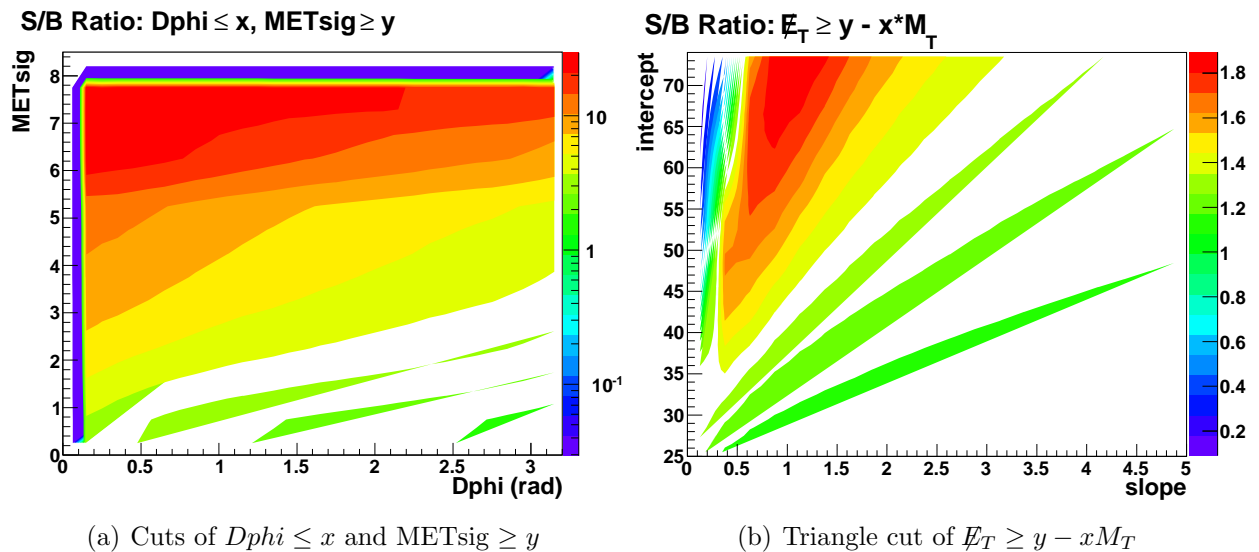


Figure 4.12 : Comparison of  $METsig$  and  $Dphi$  cuts (center column) to a triangle cut (right column) on RunIIB3  $W \rightarrow e\nu$  MC signal (a), QCD data background (b), and EM Data (c).



Sample	Triangle Cut	METsig > 5,	Add to cuts:
	$\cancel{E}_T > 55 - 0.55M_T$	$Dphi < \pi/4$	$\cancel{p}_T > 15 \text{ GeV}$
$W \rightarrow e\nu$ Signal	83.2%	83.2%	75.4%
QCD Background	48.1%	8.6%	5.6%
EM Data	43.4%	28.1%	21.2%

Table 4.4 : Cut Survival Efficiencies for Fig. 4.12

Figure 4.13 : Signal/Background ratios (shown by the color bands) for various METsig and  $Dphi$  cuts (a), and a triangle cut with varying slope and intercept (b).

factors. Cuts on METsig,  $Dphi$ , and  $p_T$  are shown to be especially powerful, compared to a triangle cut, for rejecting multijet background events which pass lepton and  $\cancel{E}_T$  selection criteria.

## Chapter 5

### Unclustered Energy Scale Development

A long-standing issue in the arena of  $\cancel{E}_T$  and unclustered energy is disagreement between data and Monte Carlo. Several analysis groups have employed reweighting schemes in order to force improved agreement, for example weighting MC events so that the scalar unclustered energy distribution is an exact match with data. It is possible that a general calibration of the unclustered energy measurement could improve data/MC agreement in a more natural manner. Unclustered energy contains the “soft” particles and jets which are not energetic enough to be reconstructed. A UE calibration would act as an energy correction for these particles, similar to the corrections applied to reconstructed objects. An attempt at such a calibration by the CMS experiment lead to an investigation of whether this could benefit DØ [20].

#### 5.1 Derivation

A vector  $\mathbf{O}_T$  can be defined as the sum of the transverse momenta of the physics objects (electrons, muons, jets, etc) in an event:

$$\mathbf{O}_T \equiv \sum_{\text{objects}} \mathbf{p}_T \quad (5.1)$$

Unclustered energy can then be written using  $\mathbf{O}_T$ , following Eq. 3.1:

$$\mathbf{ue} = -\cancel{E}_T - \mathbf{O}_T \quad (5.2)$$

The “missing” unclustered energy, or the UE component of  $\cancel{E}_T$ , is then:

$$\mathbf{mue} = -\mathbf{ue} = \mathbf{O}_T + \cancel{E}_T \quad (5.3)$$

In a coordinate system defined by the direction of  $\mathbf{O}_T$ , the parallel direction will be called  $\hat{\mathbf{o}}$ , and the component of an arbitrary vector  $\mathbf{V}$  parallel to  $\mathbf{O}_T$  will be denoted  $V_o$ :

$$\hat{\mathbf{o}} = \frac{\mathbf{O}_T}{O_T} \quad (5.4)$$

$$V_o = \frac{1}{O_T}(V_x O_x + V_y O_y) \quad (5.5)$$

In the sample of  $Z \rightarrow ee$  events used for this study (see Tabs. 3.1 - 3.2), the coordinate system defined by the transverse momentum of the  $Z$  boson can also be considered. The parallel unit vector will be labeled  $\hat{\mathbf{z}}$  and the component of  $\mathbf{V}$  in this direction will be denoted  $V_z$ :

$$\mathbf{Z}_T = \sum_{\text{electrons}} \mathbf{p}_T \quad (5.6)$$

$$\hat{\mathbf{z}} = \frac{\mathbf{Z}_T}{Z_T} \quad (5.7)$$

$$V_z = \frac{1}{Z_T}(V_x Z_x + V_y Z_y) \quad (5.8)$$

This study of unclustered energy scales will include  $\mathbf{V} = -\mathbf{UE}$  and  $\mathbf{V} = \mathbf{mue}$ . TMBLeBob UE is used with a negative sign to facilitate comparison with  $mue$ .

For a distribution of ideally measured  $Z \rightarrow ee$  events,  $\cancel{E}_T$  is expected to be zero on average since all missing energy arises from random fluctuations of noise or other measurement effects.

Considering Eq. 5.3 with no  $\mathbb{E}_T$ ,  $\mathbf{mue}$  is left to oppose  $\mathbf{O}_T$  (allowing for an unknown scale factor):

$$\mathbf{mue} = r \times \mathbf{O}_T \quad (5.9)$$

When unclustered energy has been scaled or calibrated correctly,  $r$  equals one. This corresponds to the situation where, on average,  $mue_o$  is equal to  $O_T$ ,  $mue$  perpendicular to  $\mathbf{O}_T$  is zero, and  $\mathbb{E}_T$  is zero. Since all  $\mathbb{E}_T$  in the derivation sample is expected to be fake, calibrating the unclustered energy could provide a more accurate  $\mathbb{E}_T$  value by reducing this fake  $\mathbb{E}_T$ .

In section 3.3.1 the component of unclustered energy perpendicular to the  $Z$  boson was used to derive the unclustered energy resolution because this component consists primarily of noise, fluctuations, and random energy from the underlying event. To isolate the unclustered energy to be calibrated according to Eq. 5.9, the parallel component  $mue_o$  is used [21]. The scale factor, or “response”, is the mean of the ratio  $mue_o/O_T$  as a function of an independent variable  $q$ . The mean of  $mue_o/O_T$  is calculated in each bin of  $q$ , and the response  $r(q)$  is the best fit curve through all bins.

$$\left\langle \frac{mue_o}{O_T} \right\rangle = r(q) \quad (5.10)$$

Calibrated  $mue_o$  can then be defined in terms of  $r(q)$ . Applying this calibration brings the mean value of  $mue_o^{\text{cal}}/O_T$  in each bin of  $q$  equal to one.

$$mue_o^{\text{cal}} \equiv \frac{mue_o}{r(q)} = \frac{1}{O_T} \left( \frac{mue_x}{r(q)} O_x + \frac{mue_y}{r(q)} O_y \right) \quad (5.11)$$

Calibrated  $mue_o$  can also be written as the component of  $\mathbf{mue}^{\text{cal}}$  in the direction of  $\mathbf{O}_T$ :

$$mue_o^{\text{cal}} = \frac{1}{O_T} (mue_x^{\text{cal}} O_x + mue_y^{\text{cal}} O_y) \quad (5.12)$$

Equating Eq. 5.11 with Eq. 5.12 shows that  $\mathbf{mue}^{\text{cal}}$  is found by dividing components of  $\mathbf{mue}$  by  $r(q)$ :

$$\mathbf{mue}^{\text{cal}} = \mathbf{mue}/r(q) \quad (5.13)$$

Scalar unclustered energy (Eq. 3.3) is the scalar sum of transverse energy in unclustered cells, so  $sue^{\text{cal}}$  is calculated as:

$$sue^{\text{cal}} = \sum_{\text{ue cells}} \sqrt{\frac{1}{r^2(q)}(ue_x^2 + ue_y^2)} \quad (5.14)$$

$$= \frac{1}{|r(q)|} \sum_{\text{ue cells}} ue_T = \frac{sue}{|r(q)|} \quad (5.15)$$

The effect of applying the *mue* calibration to UE and SUE from TMBLeBob as in Eqs. 5.13 - 5.15 will also be considered:

$$\mathbf{UE}^{\text{cal}} = \mathbf{UE}/r(q) \quad (5.16)$$

$$SUE^{\text{cal}} = \frac{SUE}{|r(q)|} \quad (5.17)$$

The calibrated unclustered energy can then used to calibrate other quantities. Calibrated  $\mathbf{E}_T$  and SET are found by replacing *mue* with  $\mathbf{mue}^{\text{cal}}$ :

$$\mathbf{E}_T^{\text{cal}} = \mathbf{E}_T + \mathbf{mue}^{\text{cal}} - \mathbf{mue} \quad (5.18)$$

$$SET^{\text{cal}} = SET + sue^{\text{cal}} - sue \quad (5.19)$$

As a sanity check for the algorithm, the calibrated version of  $O_T$  should be equivalent to the original version:

$$\mathbf{O}_T^{\text{cal}} = \mathbf{mue}^{\text{cal}} - \mathbf{E}_T^{\text{cal}} = \mathbf{O}_T \quad (5.20)$$

A similar calibration can be derived using the response of UE rather than  $mue$ , and in the case of events with no jets the  $Z_T$  frame can replace  $O_T$ . Distributions of average UE or  $mue$  with respect to  $Z_T$  are shown in Fig. 5.1, and with respect to  $O_T$  in Fig. 5.2.

One task of the calibration is to bring the response of the unclustered energy variable to the transverse momentum variable equal to one. The uncalibrated responses of UE and  $mue$  in bins of  $O_T$  are shown in Fig. 5.3. The independent variable  $q$  must be chosen so that the calibration meets this goal while also decreasing the widths of unclustered energy and  $\cancel{E}_T$  distributions and improving data/MC agreement. To function in the analysis framework,  $q$  should be a universally accessible variable which is not dependent on the type of event. Specifically,  $\mathbf{O}_T$  cannot be correctly defined in events with real missing energy since  $\cancel{E}_T$  from neutrinos cannot be separated from  $\cancel{E}_T$  from detector effects. While many options for  $q$  have been explored,  $q = -UE_o$ ,  $q = mue_o$ , and  $q = \sqrt{SET}$  will be presented here. The response as a function of  $O_T$  is used as a benchmark to judge improvement since response functions differ widely based on the choice of  $q$ .

## 5.2 Calibration based on UE

Following the example of CMS [21], an attempt was made to derive a calibration based on unclustered energy parallel to the  $Z$  boson momentum in zero jet events. To derive the calibration using  $UE_z$  the range of  $Z_T$  was limited to 10 GeV, below which  $UE_z$  has the expected linear relationship with  $Z_T$  (Fig. 5.1(a)). The derivation sample was extended to any number of jets by using the  $O_T$  frame, however the  $O_T$  range must still be capped around

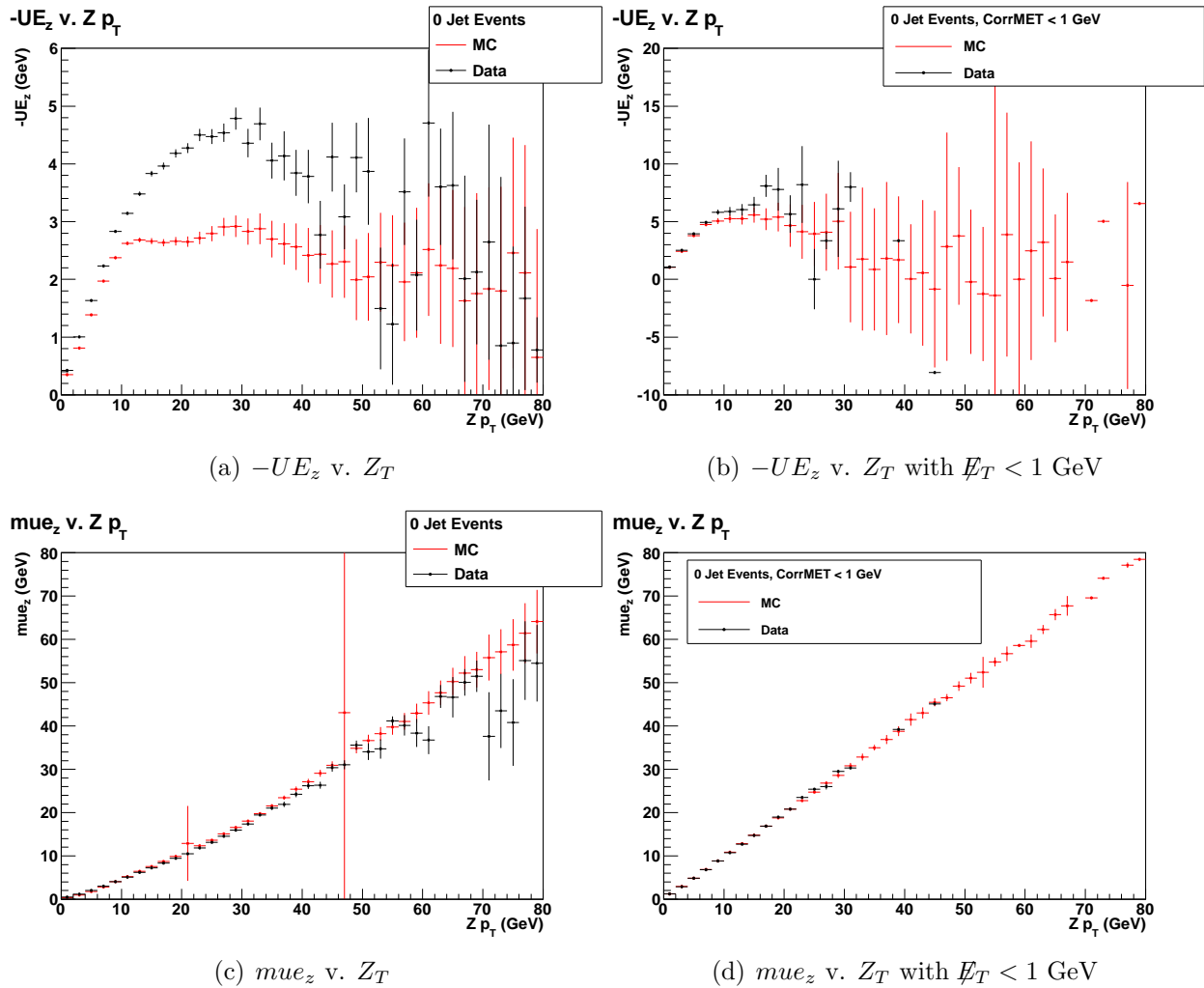


Figure 5.1 : In zero jet events, the  $O_T$  and  $Z_T$  frames are equivalent, but the TMBLeBob UE is not proportional to the  $Z$  momentum above 10 GeV (a), even with low  $\cancel{E}_T$  (b). As a sanity check, with 0 jets and very low  $\cancel{E}_T$  (d),  $mUE$  approximately equals  $Z_T$ .



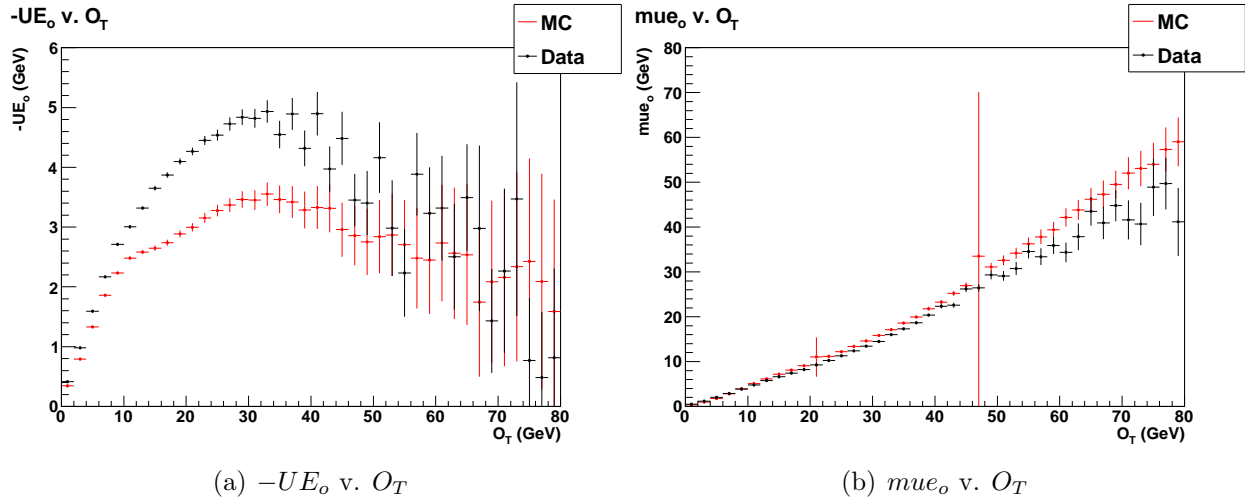


Figure 5.2 : Unclustered energy as a function of  $O_T$  in events with any number of jets.

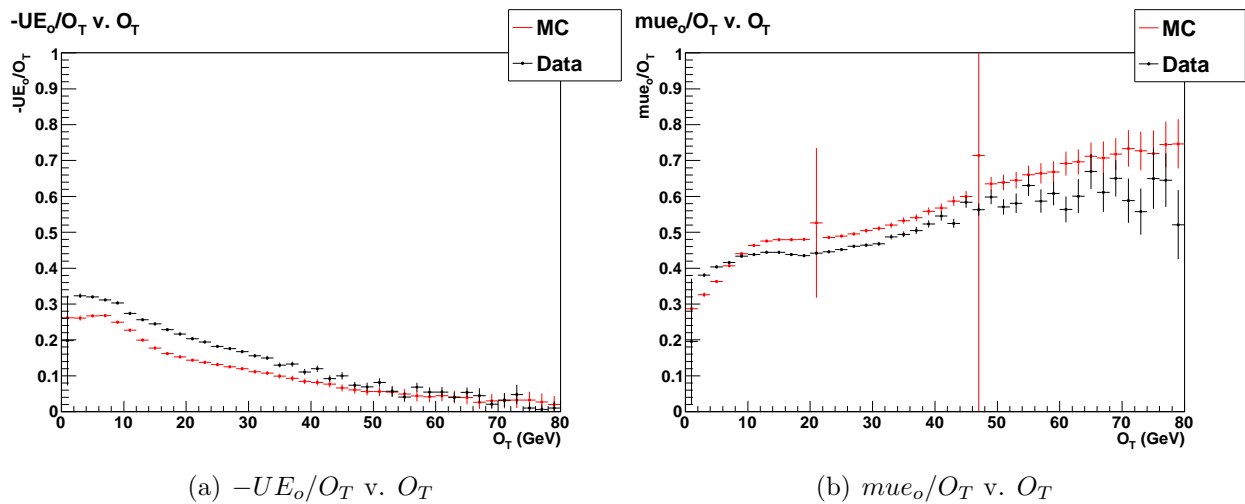


Figure 5.3 : Original responses of UE and  $mue$  to  $O_T$ , with  $q = O_T$ . Changes to these distributions (closer to or further from unity) will be used to judge the effectiveness of the calibrations.

10 GeV (Fig. 5.2(a)). For calibrations based on UE, Eqs. 5.18 and 5.19 are adjusted to read:

$$\cancel{E}_T^{\text{cal}} = \cancel{E}_T - \text{UE}^{\text{cal}} + \text{UE} \quad (5.21)$$

$$SET^{\text{cal}} = SET + SUE^{\text{cal}} - SUE \quad (5.22)$$

### 5.2.1 $q = \sqrt{SET}$

A calibration of the UE response in bins of  $\sqrt{SET}$  could be applied to any type of event.

The fit function is shown in Fig. 5.4 and written below, where  $x = \sqrt{SET}$ .

$$r = 4.161 - 1.484x + 0.217x^2 - 0.015x^3 + 0.0005x^4 - 6 \times 10^{-6}x^5 \quad (5.23)$$

Reasonable agreement between the corrected data and MC distributions was only obtained by correcting both data and MC distributions by the function derived for MC events. This calibration resulted in pronounced improvement in the slope of  $-UE_o^{\text{cal}}$  respect to  $O_T$  and the UE response in bins of  $O_T$  (Fig. 5.5). However, it failed to decrease widths or improve data/MC agreement in the UE and  $\cancel{E}_T$  distributions (Fig. 5.6).

### 5.2.2 $q = UE_o$

A UE calibration can also be derived by calculating the response as a function of  $-UE_o$ .

Since it is dependent on  $O_T$ , which cannot be correctly defined in events with real missing energy, this independent variable would not be directly applicable in the analysis framework.

Functions  $r(-UE_o)$  are listed in Tab. 5.1 and shown in Fig. 5.7. The response function

$r(-UE_o)$  is derived on events with  $O_T < 10$  GeV and then applied to the full sample.

Fig. 5.8 shows that this calibration is not effective in adjusting the slope of  $-UE_o$  with

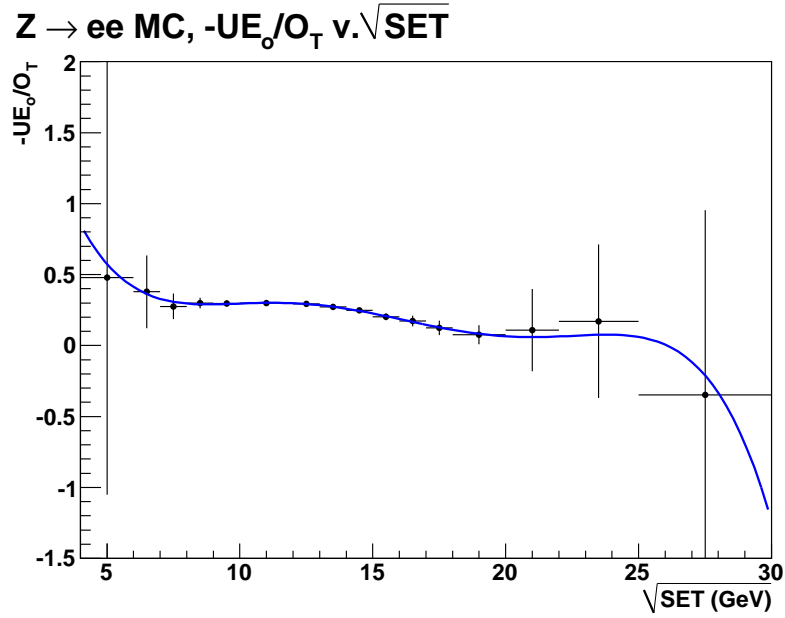


Figure 5.4 : MC fit of UE response  $r(\sqrt{SET})$ . To improve agreement in the calibrated distributions, this Monte Carlo function was used to calibrate both data and Monte Carlo events.

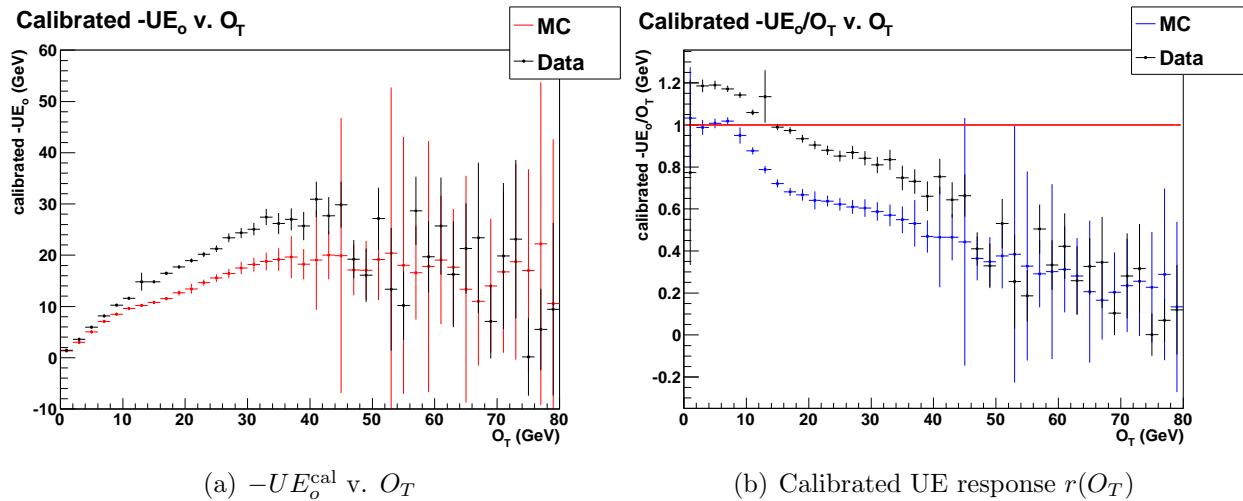


Figure 5.5 : Calibration of UE response  $r(\sqrt{SET})$ : significant improvement to the relationship between  $-UE_o$  and  $O_T$  (a) and the response  $r(O_T)$  (b).

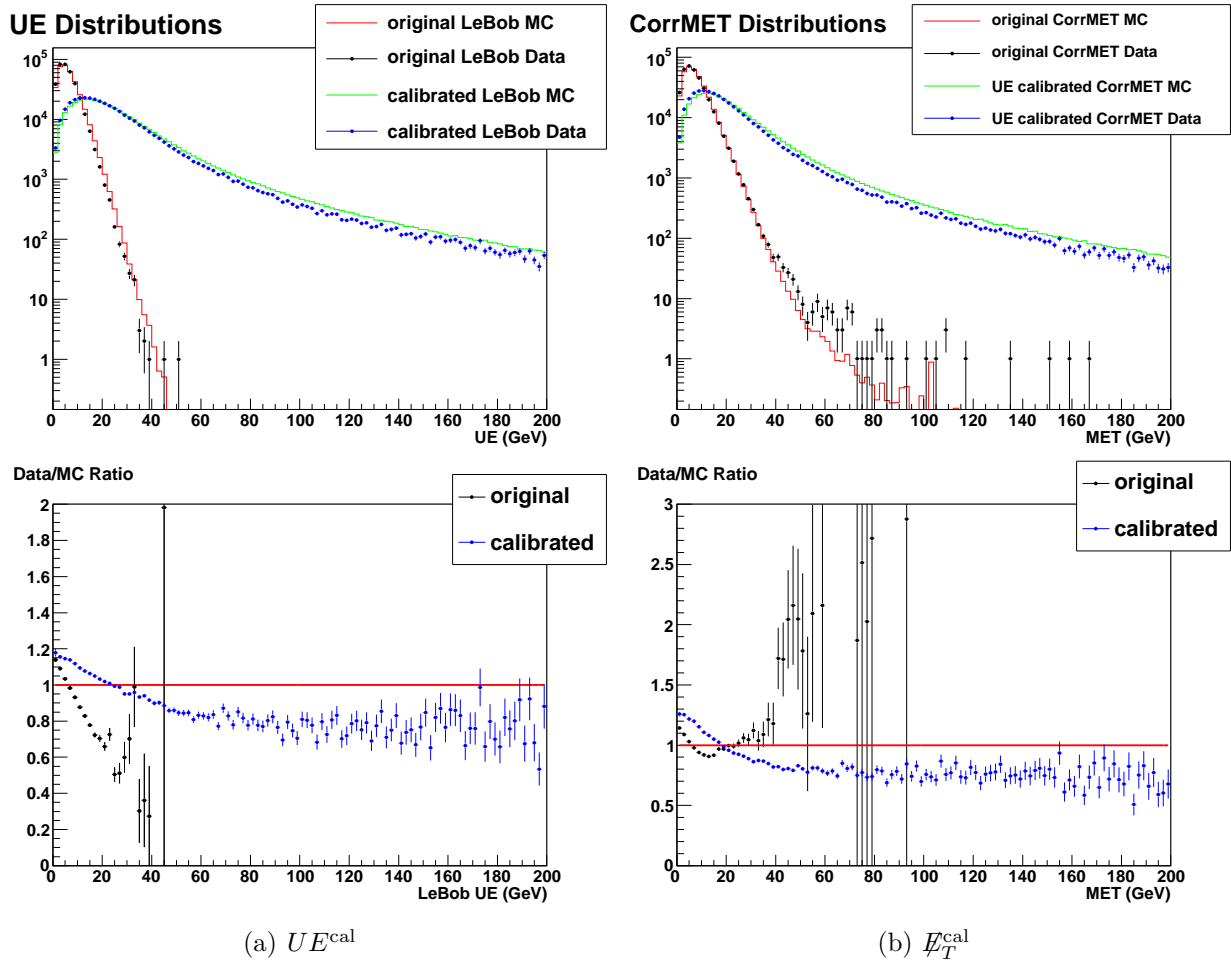


Figure 5.6 : Calibration of UE response  $r(\sqrt{SET})$ : widths of the UE and  $E_T$  distributions are greatly increased, showing that the calibration was unsuccessful.

respect to  $O_T$ , or improving the UE response  $r(O_T)$ . The width of the UE distribution is decreased but its shape is distorted, and the width of the  $\cancel{E}_T$  distribution is slightly increased. Both show better agreement between data and Monte Carlo (Fig. 5.9). Agreement was also improved in the scalar energy distributions (Fig 5.10).

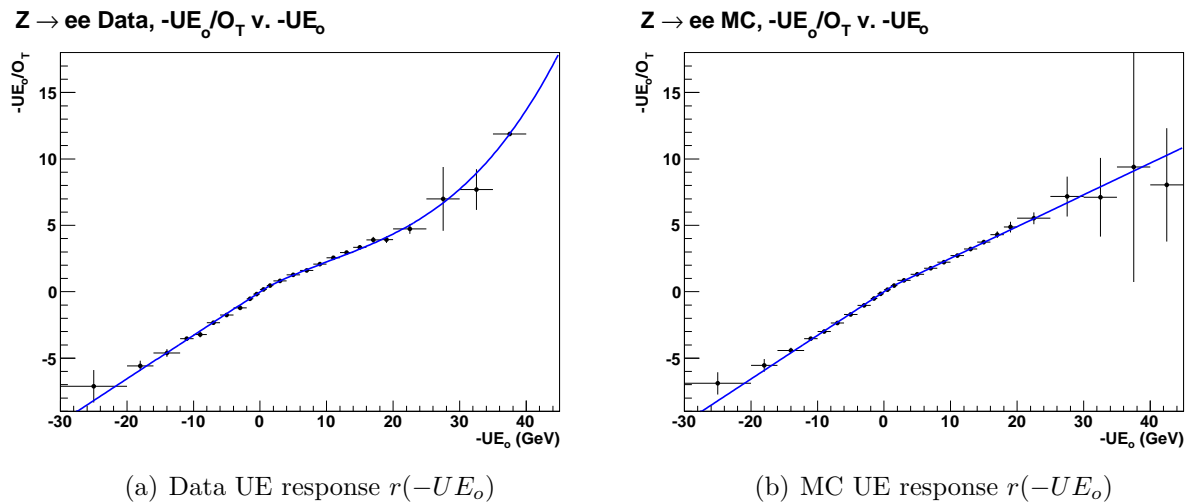


Figure 5.7 : Data and MC fits of UE response  $r(-UE_o)$ , in events with  $O_T < 10$  GeV.

Overall, no  $r(q)$  could be found which would appropriately calibrate UE in a way which would meet all the calibration requirements. Although UE from TMBLeBob is straightforward to access in the analysis framework, it is much less responsive than  $mue$  to changes in the momenta of objects in the event, so deriving an appropriate scale factor for UE is difficult. This study highlighted unexpected differences in the behavior of the two versions of unclustered energy which must be investigated more thoroughly in the future.

	Range (GeV)	$r(x = -UE_o)$	$\chi^2/\text{NDF}$
MC	$-UE_o < 1.5$	$r = -0.0028 + 0.329x$	30/10
	$-UE_o \geq 1.5$	$r = 0.120 + 0.239x$	14/13
Data	$-UE_o < 1.5$	$r = -0.012 + 0.327x$	58/10
	$-UE_o \geq 1.5$	$r = 0.087 + 0.261x - 0.007x^2 + 0.0002x^3$	21/10

Table 5.1 : Fit functions for the UE response  $r(-UE_o)$ , in events with  $O_T < 10$  GeV.

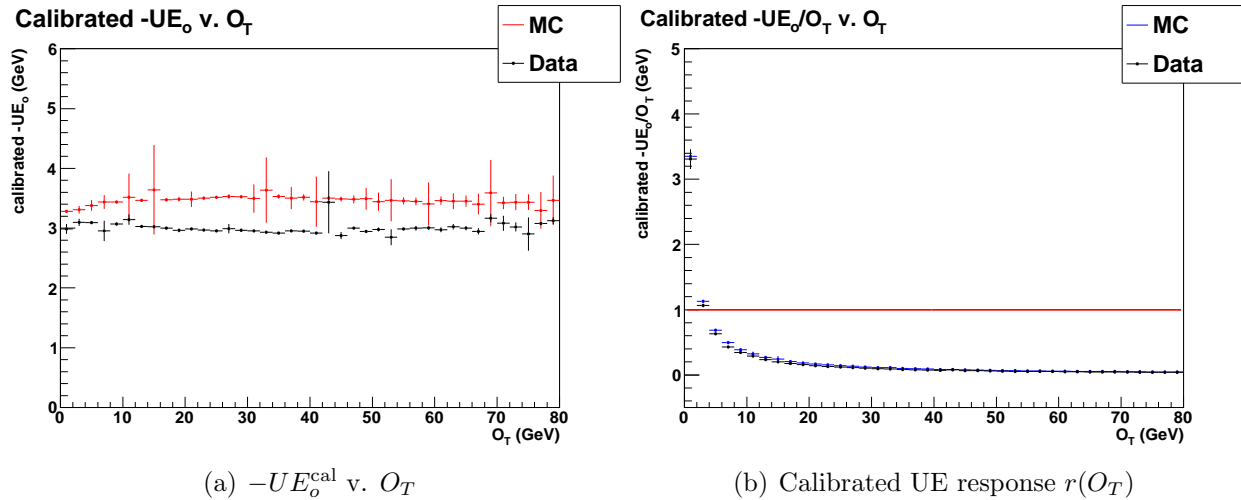


Figure 5.8 : Calibration of UE response  $r(-UE_o)$ : neither the slope of  $-UE_o^{\text{cal}}$  v.  $O_T$  (a) nor the response  $r(O_T)$  (b) are brought closer to one.

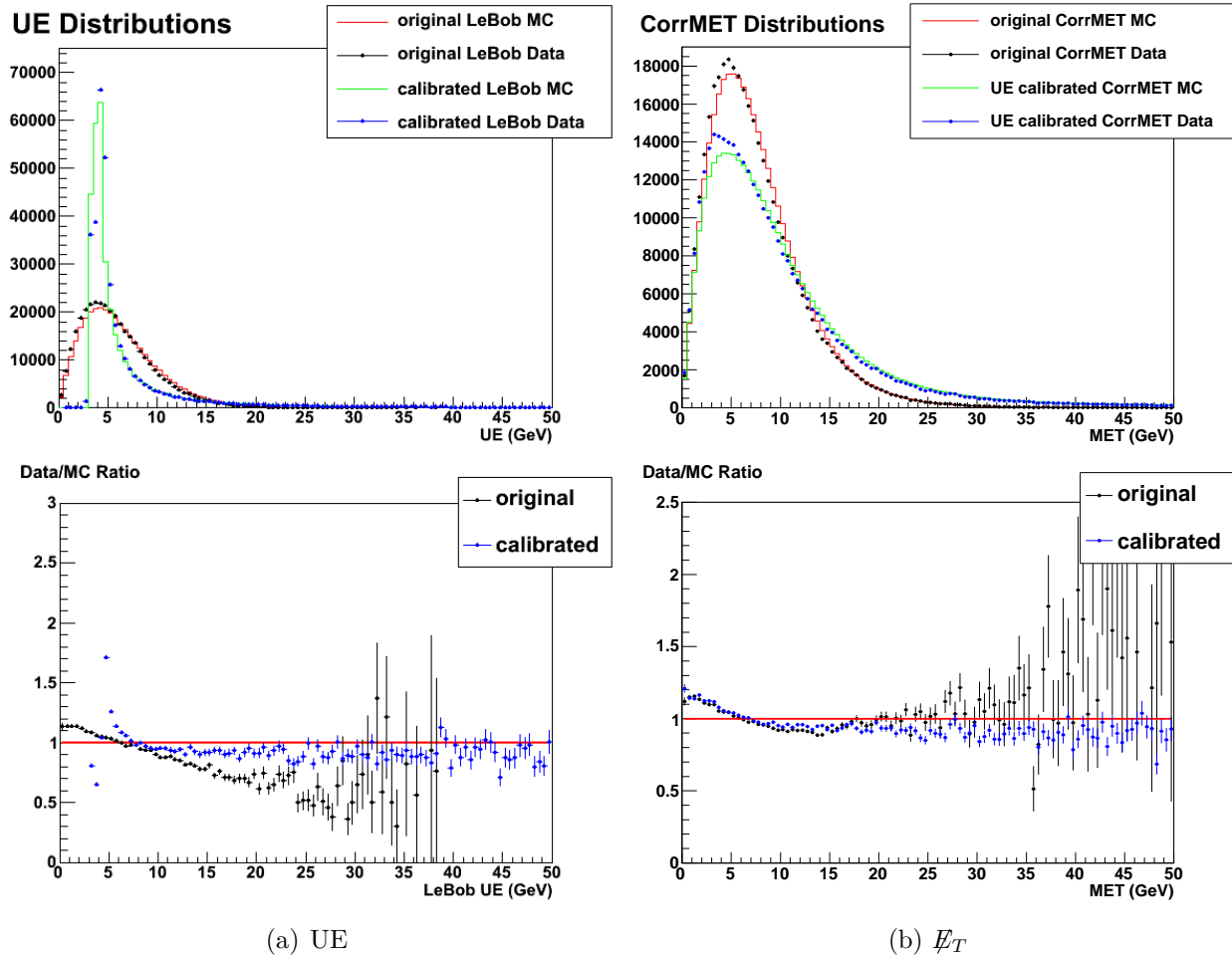


Figure 5.9 : Calibration of UE response  $r(-UE_o)$ : the shape of the UE distribution is distorted and the width of the  $\cancel{E}_T$  distribution is slightly increased. Both exhibit slight improvements in the data/MC agreement.

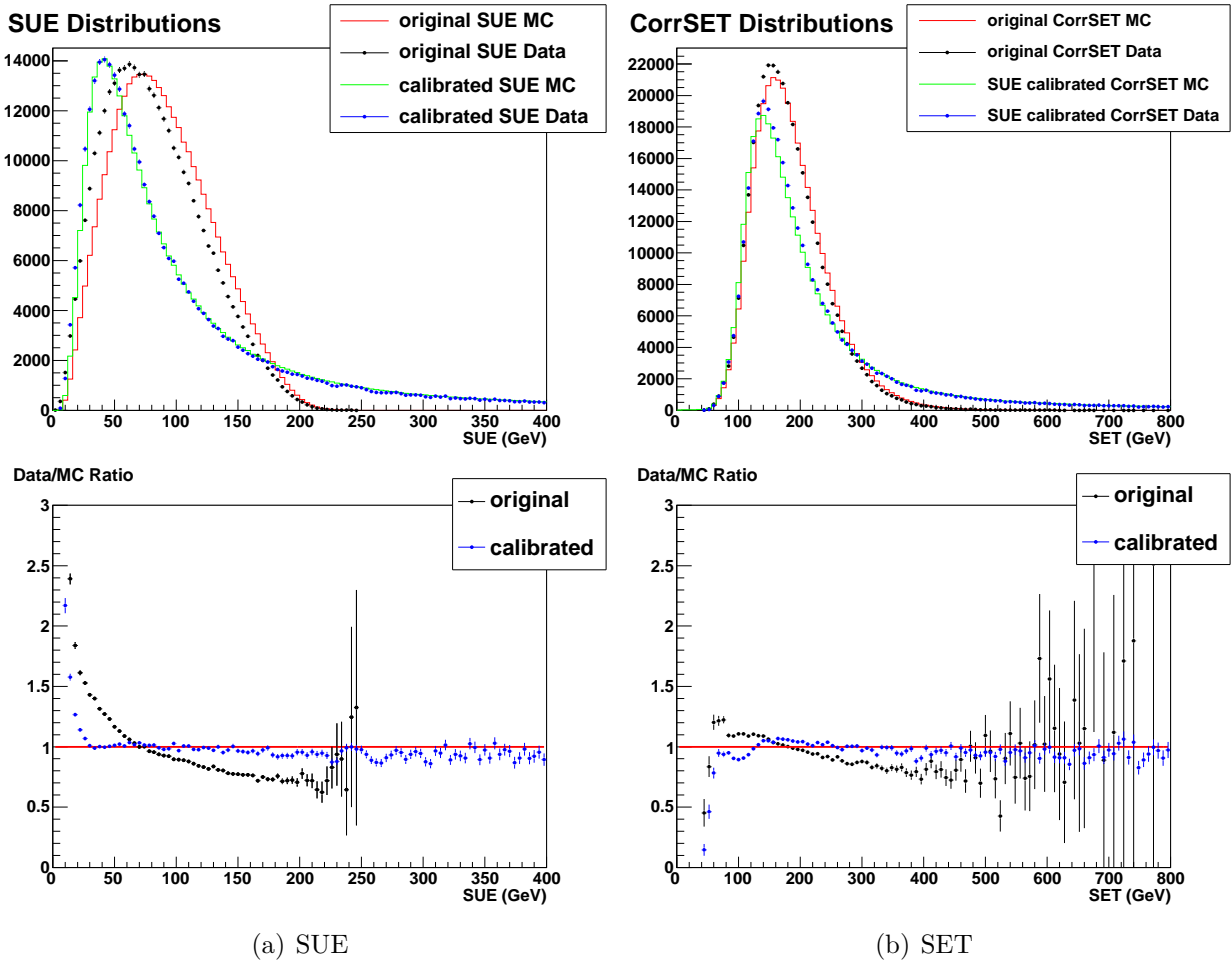


Figure 5.10 : Calibration of UE response  $r(-UE_o)$ : improved data/MC agreement in scalar energy distributions.



### 5.3 Calibration based on $mue$

#### 5.3.1 $q = \sqrt{SET}$

Calibrating the  $mue$  response to  $O_T$  as a function of  $\sqrt{SET}$  would produce a calibration that could be applied to all types of events. Figure 5.11 and Tab. 5.2 show the fitted response functions and Fig. 5.12 shows the effect of this calibration on  $mue_o$  with respect to  $O_T$ . In general the unclustered energy has been over-corrected, and the calibrated energy distributions are much wider than the original distributions (Fig. 5.13), so the calibration is unsuccessful.

#### 5.3.2 $q = mue_o$

As in the case of UE, a calibration of  $mue$  according to  $r(mue_o)$  cannot be applied to events with real missing energy. The fitted response functions are shown in Fig. 5.14 and listed in Tab. 5.3. Comparison of Fig. 5.15 with Figs. 5.2(b) and 5.3(b) shows that the response of  $mue_o^{\text{cal}}$  to  $O_T$  improves slightly with this calibration. Applying this calibration also produces the desired effects in the energy distributions: smaller resolutions in calibrated unclustered

	$r(x = \sqrt{SET})$	$\chi^2/\text{NDF}$
MC	$r = -0.756 + 0.209x - 0.012x^2 + 0.0002x^3$	1.3/12
Data	$r = -0.021 + 0.059x - 0.002x^2$	6.5/12

Table 5.2 : Fit functions for  $mue$  response  $r(\sqrt{SET})$ .

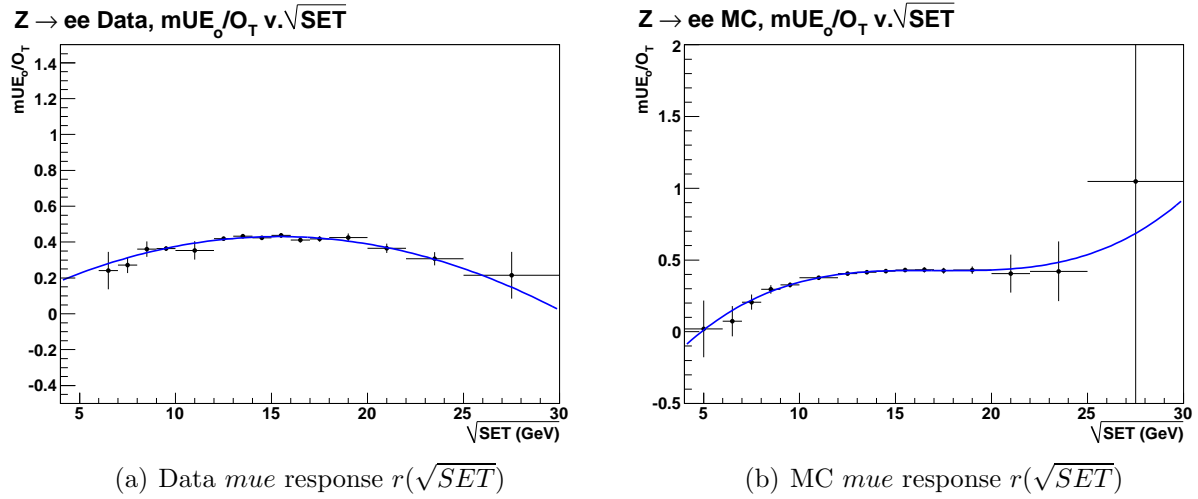


Figure 5.11 : Data and MC fits of  $mue$  response  $r(\sqrt{SET})$ .

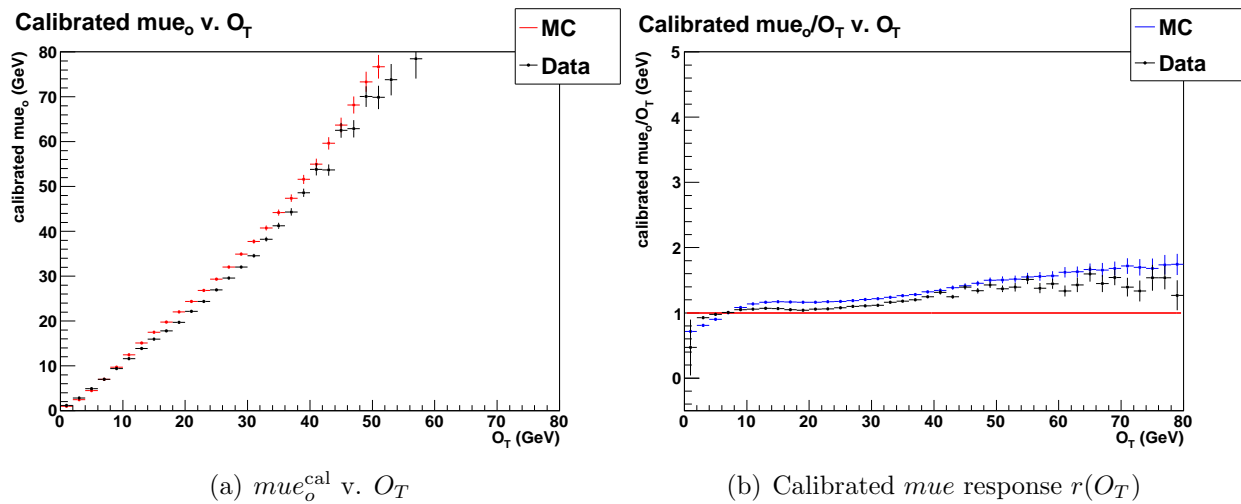


Figure 5.12 : Calibration of  $mue$  response  $r(\sqrt{SET})$ : general over-correction of  $mue_o$  with respect to  $O_T$ .

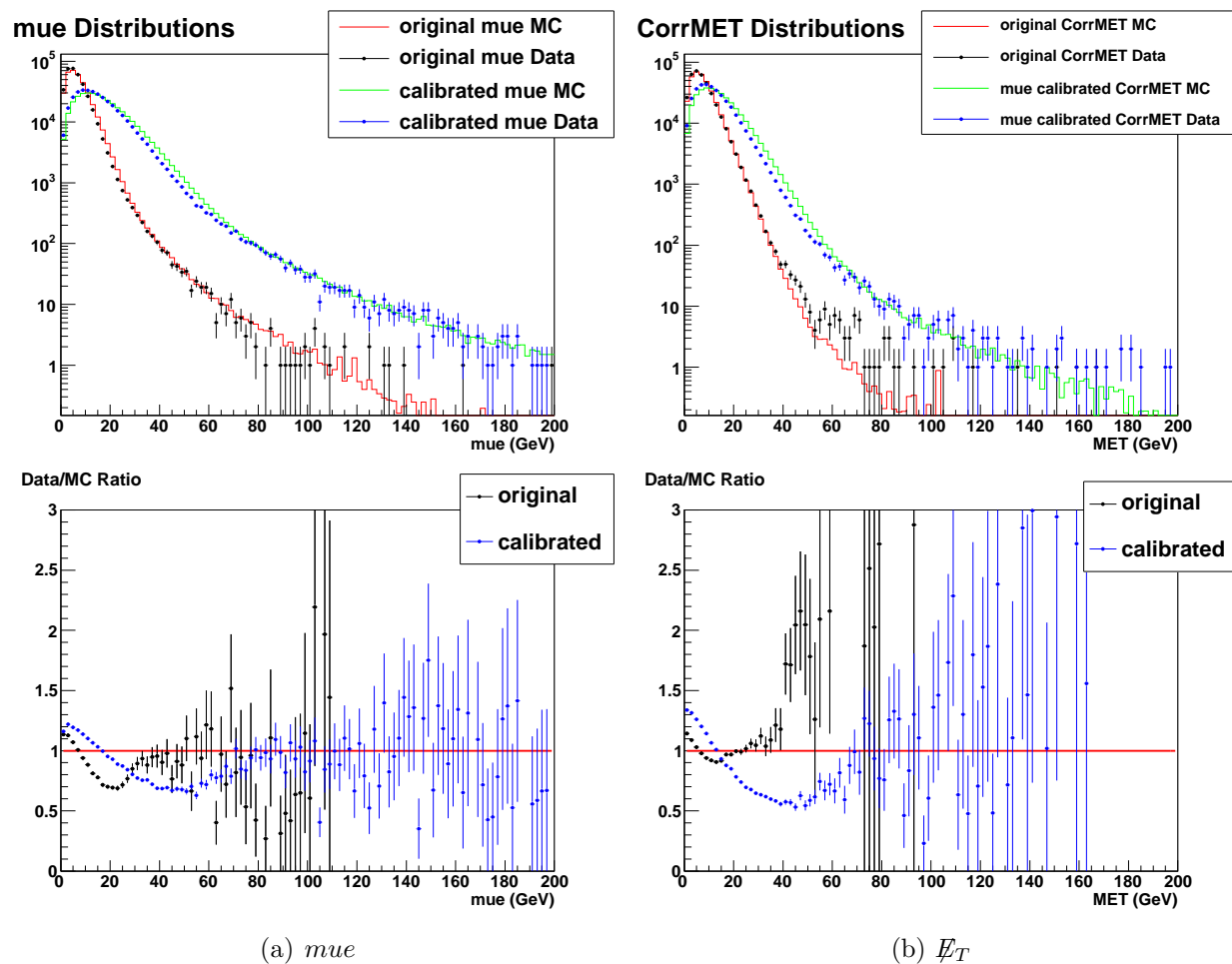


Figure 5.13 : Calibration of  $m_e$  response  $r(\sqrt{SET})$ : unsuccessful since the widths of the  $m_e$  and  $E_T$  distributions are greatly increased.

energy, reduced fake  $\cancel{E}_T$ , and significantly improved modeling of  $\cancel{E}_T$  and SET (Figs. 5.16 - 5.18).

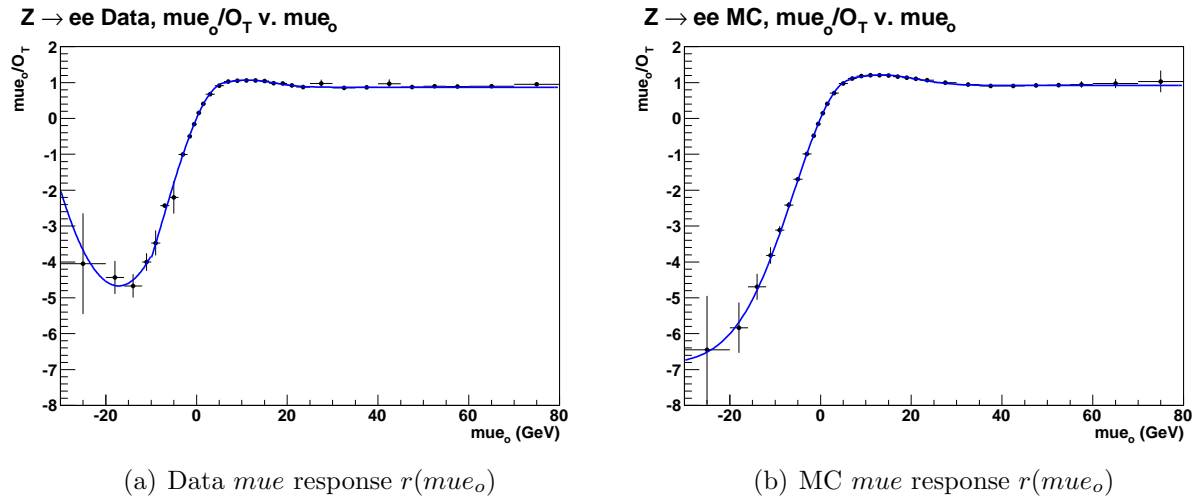
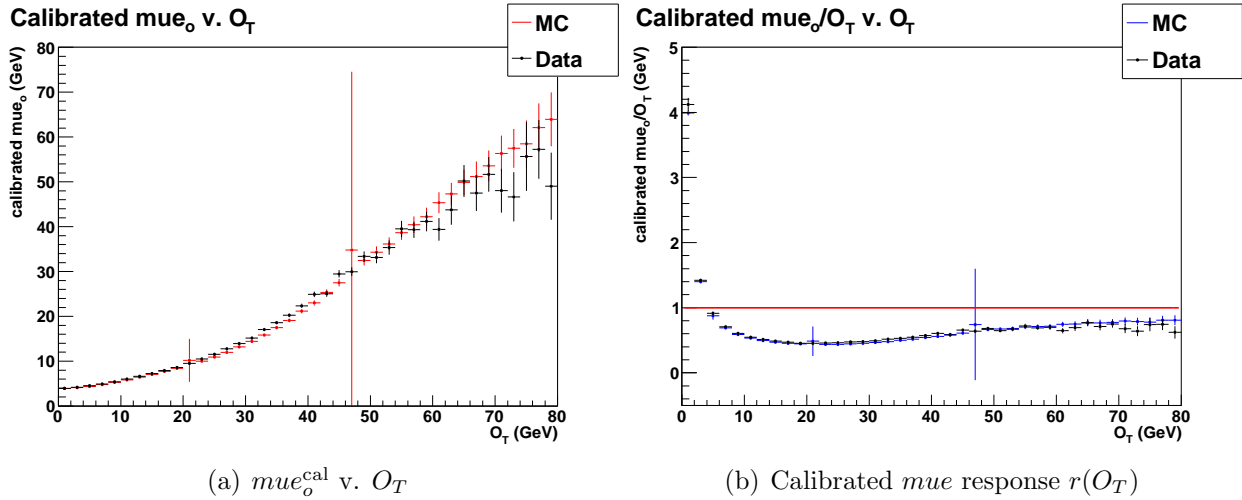


Figure 5.14 : Data and MC fits of  $\mu e$  response  $r(\mu e_o)$ .

Long tails are present in the calibrated distributions because of the response functions crossing zero. The tails can be reduced if the smoothness of the  $r(\mu e_o)$  is broken in the region near zero. Figure 5.19(a) shows that tails should be reduced over the range  $-1.5 \leq \mu e_o \leq 1.5$ . The value of  $r(\mu e_o = -1.5)$  is applied over the range  $(-1.5, 0)$  and the value of  $r(\mu e_o = 1.5)$  is applied over the range  $(0, 1.5)$ . Data/MC agreement in the remaining tail region is poor, but is generally an improvement over the uncalibrated distributions (Fig. 5.20).

	Range (GeV)	$r(x = m\mu e_o)$	$\chi^2/\text{NDF}$
MC	$m\mu e_o < 6.5$	$r = -6.859 + 7.942 \times e^{-0.5(x-6.894)^2/162.078}$	42/11
	$m\mu e_o \geq 6.5$	$r = 0.921 + 2.910 \times e^{-0.5(x-13.522)^2/59.892}$	5.6/14
	$m\mu e_o < -10$	$r = 0.148 + 0.561x + 0.016x^2$	0.6/1
Data	$-10 \leq m\mu e_o < 6.5$	$r = -8.973 + 9.971 \times e^{-0.5(x-6.510)^2/201.044}$	131/7
	$m\mu e_o \geq 6.5$	$r = 0.870 + 0.199 \times e^{-0.5(x-11.227)^2/33.744}$	17/14

Table 5.3 : Fit functions for  $m\mu e$  response  $r(m\mu e_o)$ .Figure 5.15 : Calibration of  $m\mu e$  response  $r(m\mu e_o)$ : calibrated  $m\mu e_o$  versus  $O_T$  (a) shows some distortion due to overcorrection at small  $O_T$ , but in general the response (b) is improved.

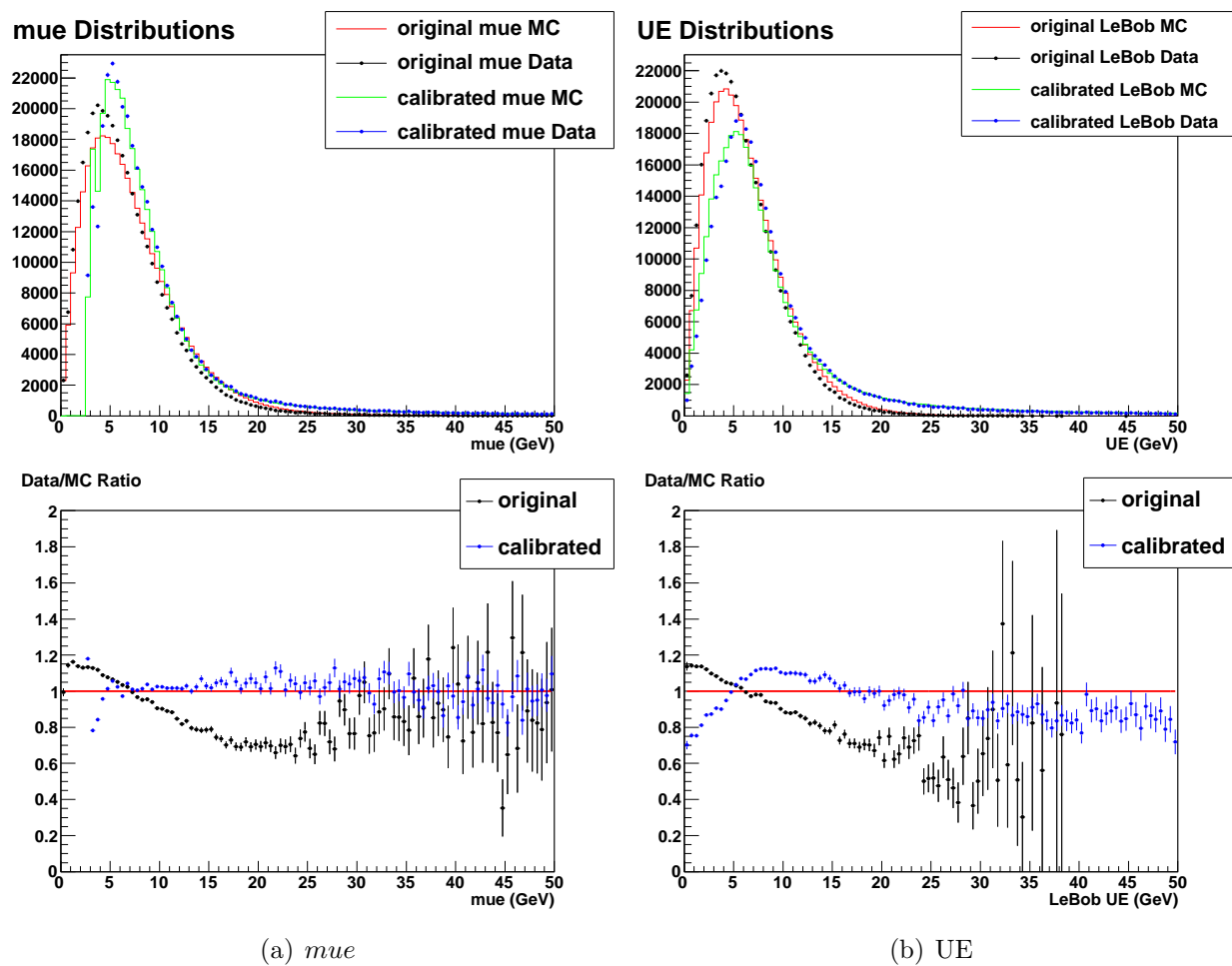


Figure 5.16 : Calibration of  $\mu e$  response  $r(\mu e_o)$ : original and calibrated  $\mu e$  and UE distributions.

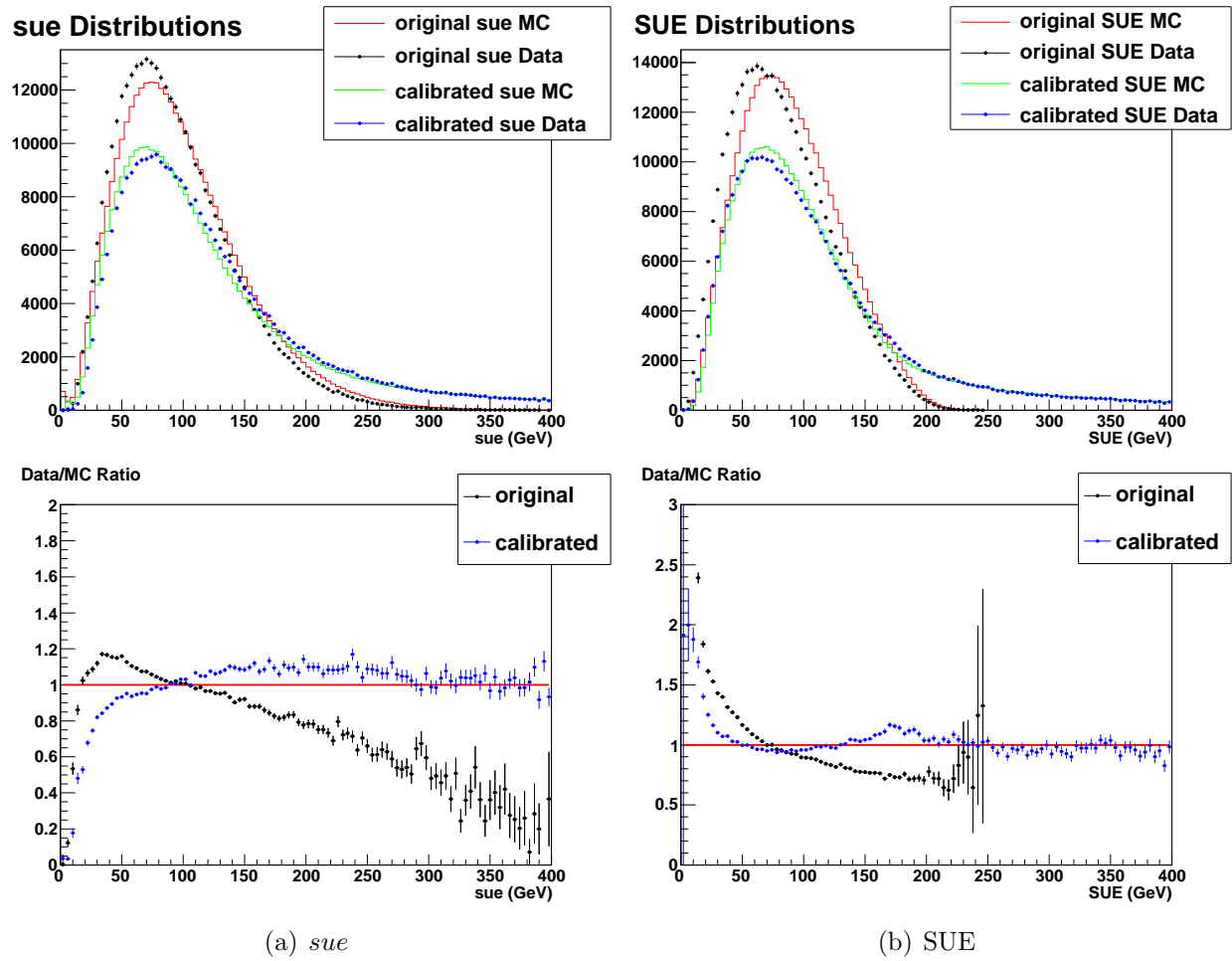


Figure 5.17 : Calibration of  $mue$  response  $r(mue_o)$ : original and calibrated  $sue$  and  $SUE$  distributions.

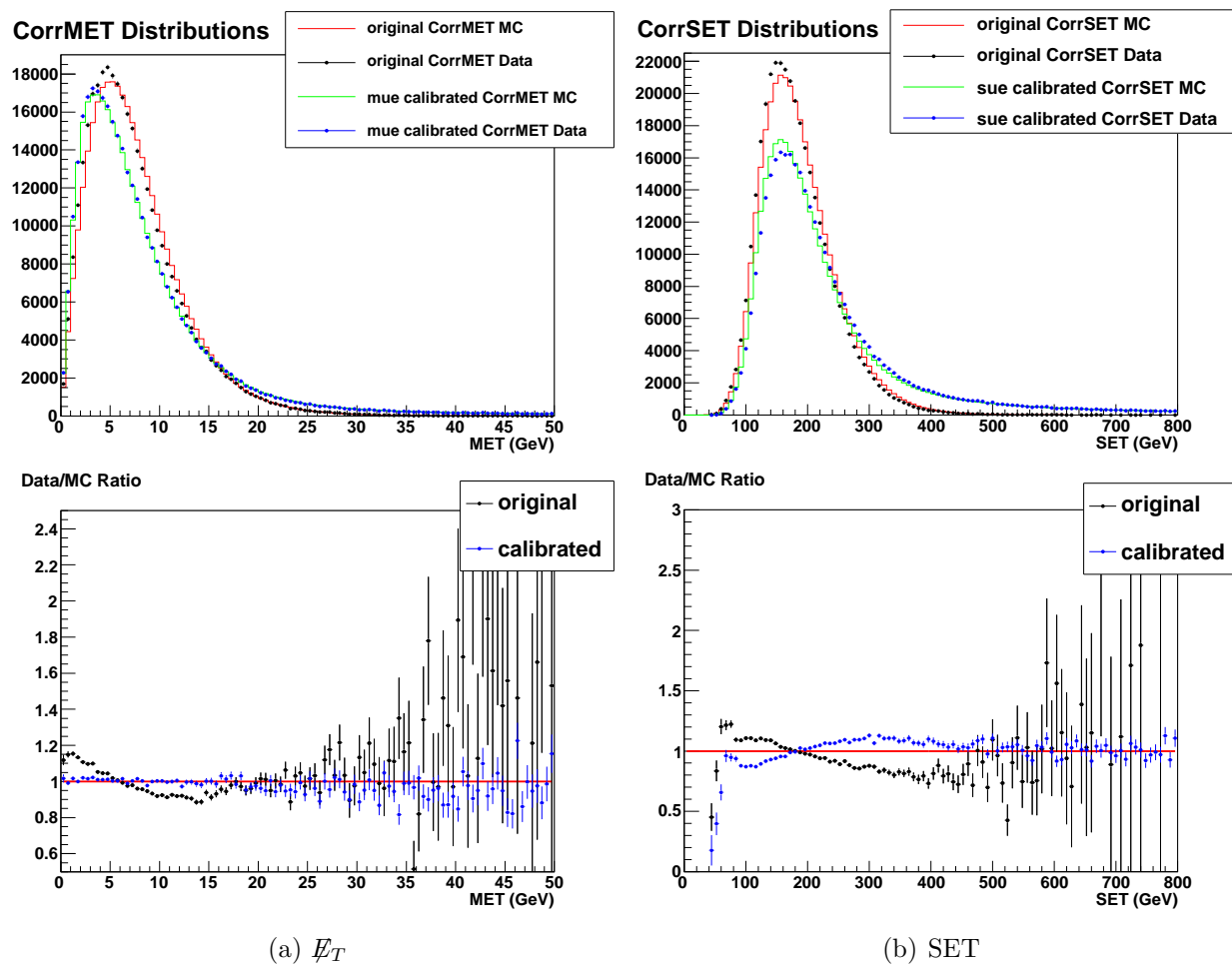


Figure 5.18 : Calibration of  $\mu$ e response  $r(mue_o)$ : original and calibrated  $\cancel{E}_T$  and SET distributions. Unique to this calibration is the clear decrease in the mean value of  $\cancel{E}_T$  and substantial improvement in data/MC agreement (a).



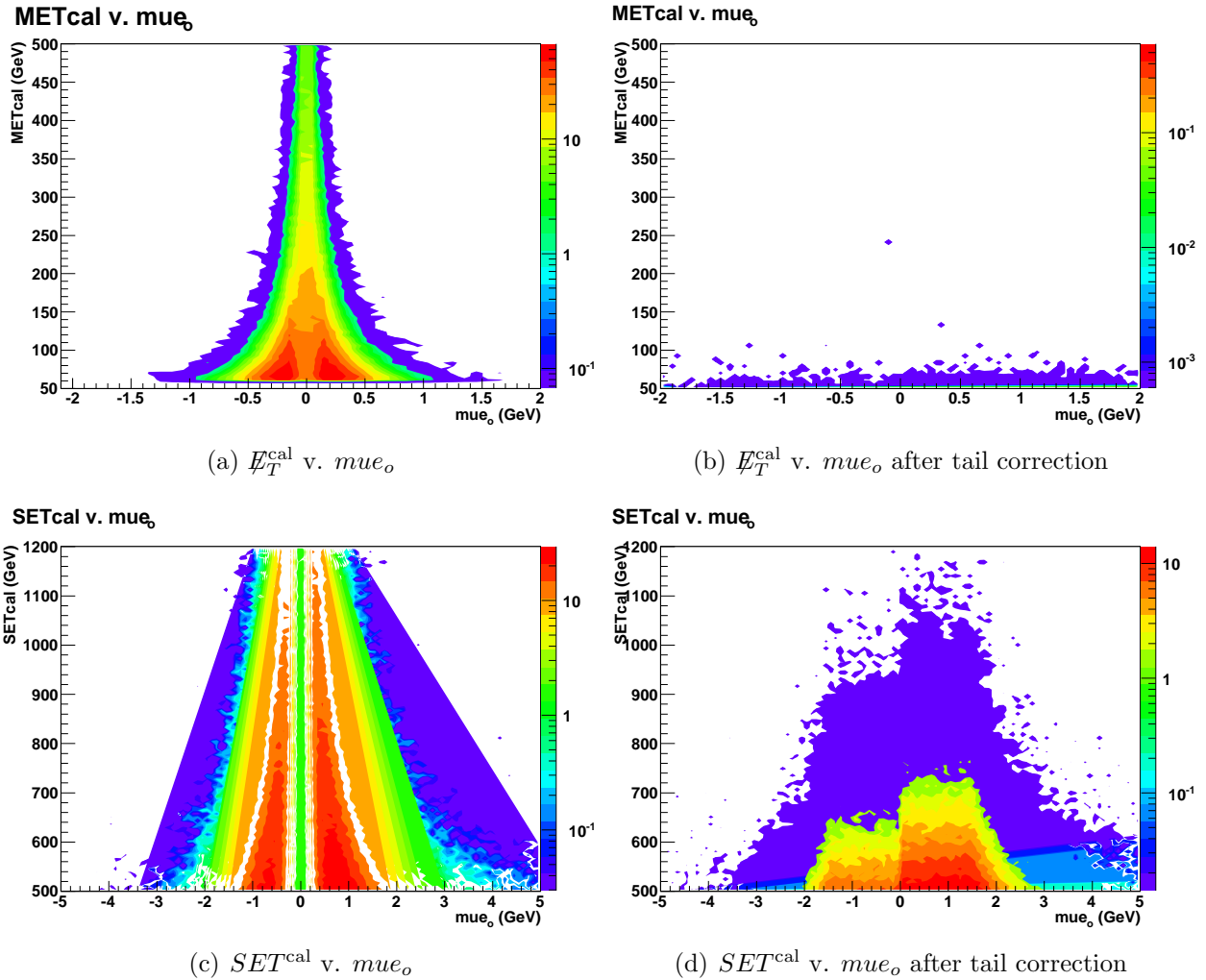


Figure 5.19 : Calibration of  $mue$  response  $r(mue_o)$  leaves tails in calibrated  $\cancel{E}_T$  and SET, which are reduced after the tail correction.

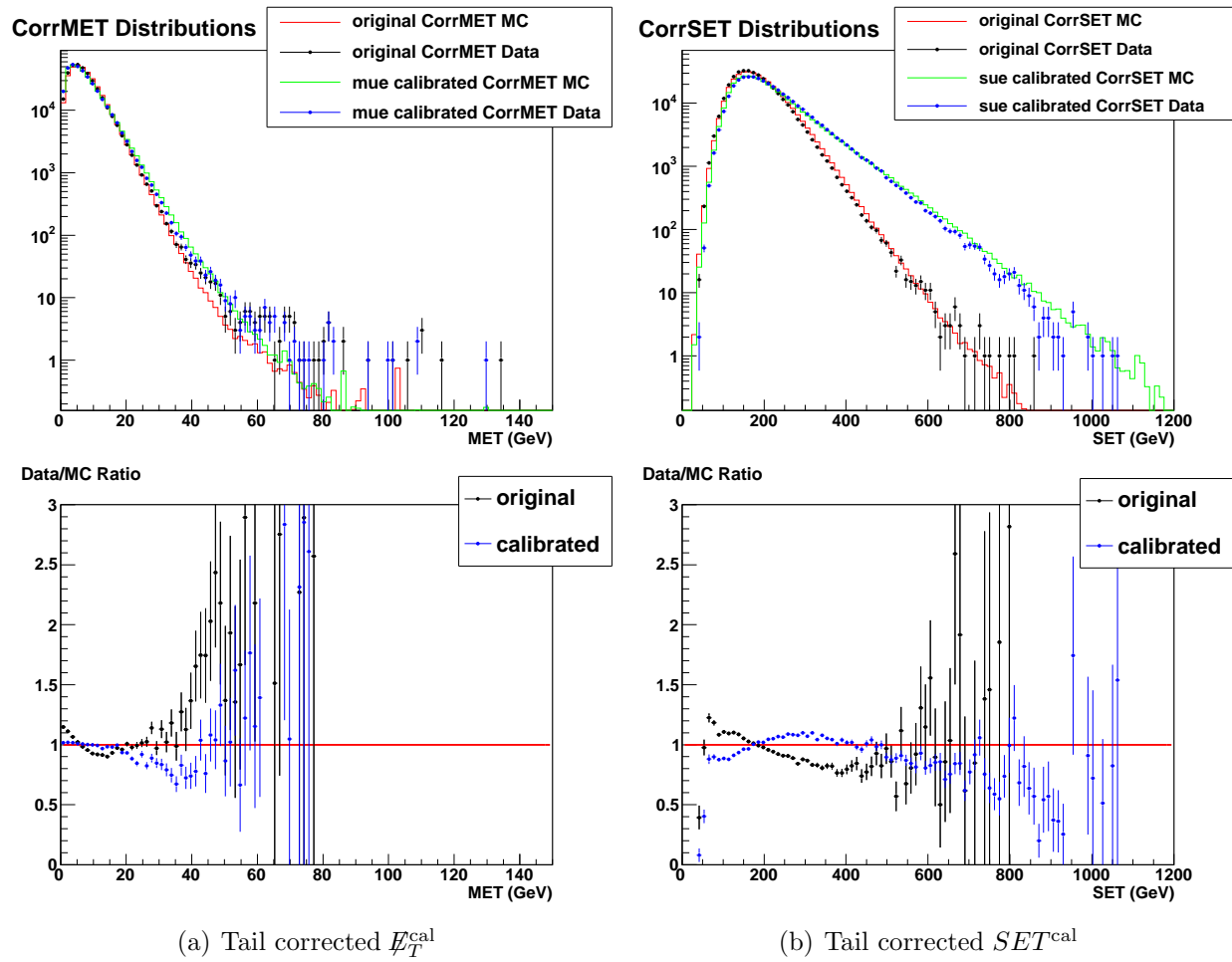


Figure 5.20 : Original and calibrated  $\cancel{E}_T$  and SET distributions showing the effects of tail corrections to the  $r(mue_o)$  calibration.

## 5.4 Summary

Calibration of  $r(mue_o)$  produces narrower energy distributions, reduced fake  $E_T$ , better data/MC agreement, and improvements in the relationship between  $mue$  and  $O_T$ . The sensitivity of  $r(mue_o)$  to events with a negative response appears to be the important difference between  $q = mue_o$  and others such as  $\sqrt{SET}$  (compare Fig. 5.14 to Fig. 5.11). It is clear that an effective calibration variable  $q$  will be a vector component rather than a vector magnitude or scalar quantity. However,  $mue_o$  cannot be calculated universally since it depends on accurate knowledge of  $O_T$ , and the mathematics of this calibration method produce infinite tails which must be removed. If a system of ascertaining  $mue_o$  without knowledge of  $O_T$  can be formulated, or another useful reference frame is found, a calibration of unclustered energy could be a great improvement to  $D\bar{O}$  analyses.

## Chapter 6

### Conclusions

Several improvements and additions have been made to missing transverse energy algorithms in the  $D\bar{O}$  analysis framework.  $\cancel{E}_T$  certification for RunIIb4 identified problems in the primary vertex algorithms which were successfully resolved for the final segments of  $D\bar{O}$  data. Certification of data reprocessed following the end of the Tevatron run showed that the behavior of  $\cancel{E}_T$  did not change significantly during reprocessing (Ch. 2).

The  $\cancel{E}_T$  significance algorithm received substantial upgrades, both to the unclustered energy resolution and the minimum probability used in the final calculation (Ch. 3). RunIIa unclustered energy resolution functions for events with two or more jets were shown to generally overestimate the correct resolutions, and new resolution functions were derived for both RunIIa and RunIIb data and Monte Carlo. Background rejection efficiency which was lost when using the new functions is regained by extending the minimum probability of the METsig calculation. The METsigAlg processor was updated to include reliable unclustered energy resolutions combined with a minimum probability value which provides users with the desired background rejection efficiencies.

A new processor was added to the framework to calculate missing momentum from tracks using a method analogous to the calculation of  $\cancel{E}_T$  from calorimeter cells (Ch. 4). The magnitude of  $\cancel{p}_T$  and the angle it forms with  $\cancel{E}_T$  ( $Dphi$ ) have proved quite powerful against

multijet backgrounds which persist after requirements of high  $\cancel{E}_T$  and high METsig. In a study of purifying a  $W \rightarrow e\nu$  sample with high  $\cancel{E}_T$ , cuts on METsig and  $Dphi$  removed approximately forty percent more multijet background events than a traditional triangle cut.

Finally, the long-standing desire to improve data/Monte Carlo agreement in  $\cancel{E}_T$  and unclustered energy distributions prompted an effort to calibrate the unclustered energy measurement (Ch. 5). No effective calibration mechanism has been found for the analysis framework's TMBLeBob UE, and the significant differences observed between this variable and a calculated version of unclustered energy ( $mue$ ) will be investigated more thoroughly in the future. The only successful calibration method for  $mue$  depends on the sum of the physics objects' transverse momenta, which cannot be calculated correctly for events with real missing energy, so the calibration cannot be applied universally. New developments are necessary before this calibration effort can move forward.

Many  $D\bar{O}$  analyses investigate processes which produce neutrinos, and several searches for physics beyond the Standard Model include potential weakly interacting particles which would also be identified through missing energy. The recent improvements to the missing energy algorithms provide users with up to date and reliable tools for understanding these elusive particles.

## References

- [1] F. Halzen and A.D. Martin. *Quarks and Leptons: An Introductory Course in Modern Particle Physics*. John Wiley & Sons, Inc., 1984.
- [2] S. Abachi et al. Observation of the Top Quark. *Phys. Rev. Lett.*, 74:2632–2637, 1995.
- [3] The ATLAS Collaboration. Observation of a New Particle in the Search for the Standard Model Higgs boson with the ATLAS Detector at the LHC. *Phys. Lett. B*, B716:1–29, 2012.
- [4] Fermilab Accelerator Division. Concepts Rookie Book, 2010. [http://www-bdnew.fnal.gov/operations/rookie\\_books/rbooks.html](http://www-bdnew.fnal.gov/operations/rookie_books/rbooks.html).
- [5] B. Casey et al. The DØ Run IIb Luminosity Measurement. *Nucl. Instrum. Methods A*, 2012. In press, <http://dx.doi.org/10.1016/j.nima.2012.08.095>.
- [6] V.M. Abazov et al. The Upgraded DØ Detector. *Nucl. Instrum. Methods*, A565:463–537, 2006.
- [7] R. Brun et al. GEANT 3 - Detector Description and Simulation Tool. CERN Program Library Long Writeup W5013, 1993.
- [8] M.L. Mangano, M. Moretti, F. Piccinini, R. Pittau, and A.D. Polosa. ALPGEN, a generator for hard multiparton processes in hadronic collisions. *JHEP*, 0307:001, 2003.
- [9] T. Sjöstrand, S. Mrenna, and P. Skands. PYTHIA 6.4 Physics and Manual. *JHEP*, 0605:026, 2006.
- [10] J. Pumplin, D.R. Stump, J. Huston, H.L. Lai, P. Nadolsky, and W.K. Tung. New Generation of Parton Distributions with Uncertainties from Global QCD Analysis. *JHEP*, 0207:012, 2002.
- [11] Fermilab Particle Physics Division Mechanical Department. D-Zero Run II 1.160 Dia. Beryllium Beam Pipe. Drawing Number: 3823.110-MD-399365, 2001.
- [12] A. Scharzman. *Measurement of the  $B^\pm$  Lifetime and Top Quark Identification using Secondary Vertex  $b$ -tagging*. PhD thesis, Universidad de Buenos Aires, 2004. Chapter 6:  $E_T$  Significance.

- [13] I. Antcheva et al. ROOT - A C++ framework for petabyte data storage, statistical analysis and visualization. *Computer Physics Communications*, 180(12):2499–2512, 2009.
- [14] X. Bu, T. Head, K. Petridis, M. Takahashi, and Y. Xie. Electron Identification for Summer 2010. Internal Note 6116, DØ Collaboration, 2010.
- [15] P. Renkel. Missing  $E_T$  Resolution study in  $Z \rightarrow ee$  Channel. Internal DØ Presentation at Double Top meeting, October 12, 2006.
- [16] P. Renkel. Update on Missing Energy Resolution. Internal DØ Presentation at Double Top meeting, January 25, 2007.
- [17] A. Dubey et al. Search for the Standard Model Higgs Boson in the  $ZH \rightarrow \nu\bar{\nu}b\bar{b}$  Channel in Run II Data. Internal Note 6293, DØ Collaboration, 2012.
- [18] X. Lei. MET significance with new unclustered energy resolution functions. Internal DØ Presentation at  $ZH \rightarrow \nu\bar{\nu}b\bar{b}$  meeting, June 26, 2012.
- [19] H. Greenlee. Motion of a Charged Particle in an Electric Field. Internal Note 4180, DØ Collaboration, 2003.
- [20] The CMS Collaboration. Missing transverse energy performance of the CMS detector. *Journal of Instrumentation*, 6(09):P09001, 2011. Appendix A: Optimization of  $\cancel{E}_T$  Corrections.
- [21] U. Gebbert. *Photons, Missing Energy and the Quest for Supersymmetry at the LHC*. PhD thesis, Universität Hamburg, 2012. Chapter 4: Measuring the Missing Transverse Energy.